POLITECNICO DI TORINO

Collegio di Ingegneria Chimica e dei Materiali

Master of Science Course

in Materials Engineering for Industry 4.0

Master of Science Thesis

Assessing the Feasibility of Laser-Based Directed Energy Deposition (LB-DED) for Manufacturing Copper-Based Cooling Structures onto Gyrotron Cavities



Tutors

prof. Christian Leinenbach

prof.ssa Mariangela Lombardi

Candidate

Lorenzo Sandrone

October 2026

Abstract

Gyrotron cavities for high-power millimeter-wave applications – including fusion research, geothermal systems, and advanced particle sources – operate under extreme electromagnetic and thermal loads. Heat is deposited within only tens of microns of the inner radiofrequency (RF) surface, and long-term performance depends on efficient heat extraction without affecting dimensional stability or vacuum compatibility.

Glidcop, a dispersion-strengthened copper alloy containing fine alumina particles, is widely used for such cavities thanks to its excellent electrical and thermal conductivity and high-temperature strength. However, today's monolithic, subtractively manufactured Glidcop cavities leave almost no possibility to integrate efficient cooling structures close to the RF wall.

This project explores whether a Laser Based Directed Energy Deposition system can be used to print copper alloy features directly onto a pure copper substrate.

This study was carried out to understand the interaction between the copper/copper alloys and the Near InfraRed (NIR) laser, investigating how the process parameters and substrate surface pre-treatment correlate with adhesion, thermal distortion, and melt pool stability.

COMSOL Multiphysics simulation work was integrated in the study to better understand the thermal evolution of the process and to identify the system requirements to achieve a stable DED process with NIR laser.

The project aims to deliver better understanding of the LB-DED process for copper and copper alloys, marking a step forward the realization of efficient and advanced cooling structures onto gyrotron cavities and nuclear fusion reactor development.

Keywords: Gyrotron Cavities, Additive Manufacturing, LB-DED, Copper, NIR-Laser Absorptivity, Immersion Deposition of Tin, COMSOL Simulation.

Acknowledgements

This master's thesis was conducted within the framework of the Swiss Plasma Center (SPC) at EPFL, and the research was carried out at the Swiss Federal Laboratories for Materials Science and Technology (Empa), within the Laboratory for Advanced Metallurgy & Manufacturing of Metals (AM^3), from March to August 2026.

First and foremost, I would like to express my sincere gratitude to Prof. Christian Leinenbach for welcoming me into his research group and for offering me the opportunity to carry out this project, as well as for his valuable advice and counselling throughout my journey. I am deeply grateful to Dr. Marc Leparoux for his steady guidance and support, especially during the most demanding and challenging phases of this work. Our discussions never failed to spark my curiosity, constantly providing fresh perspectives and intellectual stimulation. I would also like to thank the entire research group – Folco, Justin, Davi, Abdullah – for their continuous assistance and collaborative spirit, and all the people from Empa who made these six months undoubtedly much more enjoyable and fun.

I would also like to thank my extended family for the last six months, my roommates – Mika, Salomé, Mirjam – who never failed to make me feel home, and my Italian dudes – Vincenzo, Matteo, Giacomo – who didn't fail to export some transalpine healthy ignorance.

Agli amici di sempre – Ade, Albi, Savo, Umbi – perché, anche se per qualche ora e di sfuggita, c'era sempre tempo per una chiacchierata durante i miei ritorni lampo in patria. Ai miei coinquilini – Barbe, Gullo, Fume – per tutte le partite a scacchi e bowling sulla Wii e ai miei compagni di uni per avere reso il Poli un posto un po' più colorato in questi cinque anni. Ad Alfre, Auro e tutto il team del Cus per avere condiviso la passione per l'arrampicata nel modo più divertente e ignorante possibile.

Alla mia famiglia, per farmi sentire il vostro supporto anche a chilometri di distanza. Ai miei genitori, per tutti i sacrifici che avete sempre fatto per non farmi mai mancare nulla e lasciarmi la possibilità di scegliere. Avere la sensazione di poter fare un salto più lungo in avanti per ogni vostro passo indietro, con la sicurezza di trovare un braccio allungato nel caso non dovessi atterrare, è la forma più grande di fiducia che mi avete mostrato e per cui vi sarò sempre grato.

A mio fratello, per essere costantemente la mia fonte più grande di ispirazione. Da piccolo lo nascondevo sotto le mentite spoglie di competizione, ma in realtà ho sempre desiderato di essere come te.

Infine, a Marta, per dimostrarmi come non esista distanza troppo lunga per non sentire la vicinanza, il calore e il sostegno della persona giusta. Mi hai fatto capire che la vita è a colori e può essere artistica anche per un ingegnere. Se ci sono dei disegni in questa tesi, è per le ore passate ad imparare da te.

Table of Contents

Abstract i
Acknowledgements ii
Table of Contents iii
List of Figures v
List of Tables ix
Nomenclature xi
1 Introduction 1
2 LB-DED of Copper and Copper Alloys 5
2.1 NIR LB-DED of copper and copper alloys: challenges and strategies 5
2.1.1 The narrow stable melting window 5
2.1.2 Surface texturing/modification of the substrate 6
2.1.3 Surface modification/coating of powders 6
2.1.4 Overcoming the absorptivity problem: green and blue lasers 7
2.2 Simulation of the DED process 8
3 Materials and Methods 9
3.1 Simulation of the LB-DED Process 9
3.1.1 Thermal Model Setup 10
3.1.1.1 Thermal equilibrium 10
3.1.1.2 Moving Laser Heat Source 10
3.1.1.3 Phase Change Material Modelling 11
3.1.1.4 Temperature-dependent Material Properties 12
3.1.1.5 Boundary Conditions 12
3.1.2 High-Speed Thermal Camera Setup 13
3.2 Substrate Material 14
3.2.1 Surface Sandblasting 15
3.2.2 Titanium Sheet 15
3.2.3 Carbon spray coating 16
3.2.4 Immersion deposition of tin 16
3.3 Powder Feedstock 20
3.3.1 Powder characterization 20
3.4 Directed Energy Deposition System 21
3.4.1 Laser Beam Specifications 22

3.4.2 Nozzle Head 22
3.4.3 Powder Feeding System 23
3.4.4 Powder Jet Convergence Height Characterization 24
3.5 High-speed Visible Imaging – Thermal Distortion Analysis 25
3.6 Sample Preparation 26
3.7 Optical Imaging 27
4 Results and Discussion 28
4.1 Untreated and Sandblasted Copper Substrate 28
4.1.1 Numerical Simulation of Laser-Material Interaction on Copper 28
4.1.2 LB-DED of Single Tracks onto Surface Sandblasted Copper Substrate 30
4.1.3 Numerical Simulation of Sandblasted Copper Substrate Melting Thresholds 33
4.2 Surface-modified Copper Substrate 34
4.2.1 Titanium Starting Foil 34
4.2.2 Carbon Spray Coated Copper Substrate 35
4.2.3 Immersion Deposited Tin Coating 36
4.2.3.1 Numerical Simulation of Laser-Material Interaction on Tin-Coated Copper 37
4.2.3.2 LB-DED Experiments on Tin-Coated Copper Substrate 38
4.2.3.3 Experimental Validation of the Simulated Model 45
4.2.3.4 Numerical Simulation of Tin-Coated Copper Substrate Melting Thresholds 47
5 Conclusions 50
5.1 Summary of Key Findings 50
5.2 Future Work 51
Appendix A 54
Appendix B 56
Bibliography 57

List of Figures

Figure 1.1: Schematic view of a gyrotron, with its main components [5] 1

Figure 1.2: (a) 3D sketch of the resonant cavity and a portion of the launcher, with the profile of a heat load released on the inner wall. The green volume represents the area devoted for cooling: (b) Raschig Rings cooling, (c) azimuthal micro-channels cooling, (d) longitudinal mini-channels cooling (modified from [12]) 2

Figure 1.3: Additively manufactured tungsten gyroid TPMS structure [17] 3

Figure 1.4: Main types of additive manufacturing (AM) processes according to ASTM F2792—12a [18]. 3

Figure 1.5: Schematic views of pulsed Laser-PBF (a) and Laser-DED (b) [23] 4

Figure 2.1: (a) 3D morphology of a laser-etched surface, (b) schematic representation illustrating laser absorption enhancement. Adapted from Zhang et al. [37] 6

Figure 2.2: Absorptivity of pure copper as a function of wavelength for: SLM produced parts (orange), powder sample of D10 = 15 μm and D90 = 45 μm (black). Adapted from Domine et al. [48]. 7

Figure 3.1: Schematic representation of the 3D thermal FE model highlighting the moving Gaussian laser heat source (q_0), conductive heat dissipation to the stainless-steel base plate (q_{cond}), and convective (q_{conv}) and radiative (q_{rad}) heat losses to the ambient 9

Figure 3.2: θ_1 and θ_2 Heaviside step functions evolution over the transition interval as is displayed from COMSOL software 11

Figure 3.3: Schematic sketch of the setup used for the infrared termography of the LB-DED process 14

Figure 3.4: Surface profile analysis after sandblasting (left), and a sandblasted copper plate (right) 15

Figure 3.5: Thin titanium sheet clamped on the roughened pure copper substrate inside the LB-DED chamber 16

Figure 3.6: Schematic illustration of the complexation process. The copper ions are captured by the thiourea, and the reaction is shifted towards the tin deposition by reduction of the dissolved salt 17

Figure 3.7: Detailed experimental steps for the immersion deposition process of tin onto copper substrate: acetone degreasing (a), surface deoxidization (b), deionized water boiling and thiourea dissolution (c), immersion of copper substrate in Solution 1 (d), cooling to reaction temperature (e), deposition process (f-g), tin coated copper substrate (h). 19

Figure 3.8: Cross-section optical imaging of the tin (green/grey layer in picture) coated copper substrate 19

Figure 3.9: Particle volumetric size (left) and aspect ratio distribution (right) for the 85/15CuSn powder 20

Figure 3.10: 85/15CuSn powder morphology from Morphologi 4 optical imaging; the red dotted circles highlight the satellites 20

Figure 3.11: Snapshots of the flowing powder bed taken at different drum rotating speed 21

Figure 3.12: BeAM Mobile 1.0 LB-DED machine working chamber and reference axes 22

Figure 3.13: Sketch of the coaxial BeAM Mobile 1.0 LB-DED nozzle head 23

Figure 3.14: Powder feed rate as a function of plate rotation speed for the 85/15CuSn powder at fixed primary, shaping and carrier gas flow rates 23

Figure 3.15: Powder jet convergence height as a function of plate rotation speed at fixed primary, shaping and carrier gas flow rates (a), schematic illustration of the measurement method (b), processed image at 6 % of plate rotation speed (c) 24

Figure 3.16: Schematic sketch of the setup used for the backlight high-speed visible imaging of the LB-DED process 25

Figure 3.17: Adopted sample preparation routine 26

Figure 3.18: Cross-sectional optical micrographs of etched samples of bronze deposition on copper substrate using different etching solutions: (a) 1:10 solution of ammonium persulfate ($(NH_4)_2S_2O_8$) in deionized water, (b) 1:40 solution of ferric chloride ($FeCl_3$) in a 1:20 hydrochloric acid (HCl, 37%) ethanol solution, and (c) the selected Klemm II solution. 27

Figure 4.1: (a) Mesh quality plot for the simulated model; (b) magnification of the refined sub-mesh for the heat-affected zone (HAZ) modeling..... 29

Figure 4.2: Temperature field at the end of the laser track for: (a) untreated copper substrate, (b) sandblasted copper substrate..... 30

Figure 4.3: Example of a deposited 85/15CuSn single track onto roughened pure copper substrate; imprints of already detached beads can be seen in the back 31

Figure 4.4: Single tracks deposited onto pre-heated roughened pure copper substrate at 300 °C. The dark surface of the substrate is due to the presence of the oxide layer 32

Figure 4.5: (a) Cu-binary phase map at the end of the laser track for the 2,800 W scenario (green highlights the liquid phase volume, while red is the solid volume); (b) cross-sectional view of the melt pool at t = 5.995 s, with related measurements to the known depth of the sub-mesh (highlighted in red, A* = 225 μm)..... 33

Figure 4.6: Thin titanium sheet LB-DED experiments. The letters correspond to the test labels reported in Table 4.3. The different colors highlight the different types of experiment: red for laser scans without powder, pink for single tracks, and blue for walls 35

Figure 4.7: Carbon spray coated copper substrate experiments: laser scan (1, red) and 85/15CuSn single tracks (2-10, pink) 36

Figure 4.8: (a) Mesh quality plot for the tin coated substrate model; (b) magnification of the refined sub-mesh for the heat-affected zone (HAZ) modeling 37

Figure 4.9: Temperature field at the end of the laser track for the tin-coated copper substrate 38

Figure 4.10: Detailed view from inside the machine chamber of 85/15CuSn single tracks deposited onto the tin coated copper substrate 39

Figure 4.11: Optical cross-sectional micrographs of the deposited bronze single tracks onto the tin coated copper substrate (process parameters listed in Table 4.6). The operators between the samples state the relationships between energy density (pink) and LEPF (yellow) respective values 39

Figure 4.12: 100x magnification of an 85/15CuSn single track cross-section, with highlighting of the tin-rich surface valleys. The light-blue dotted curve highlights the metallurgical bond between the tin coating and the deposited bronze layer 40

Figure 4.13: High-speed images of the laser beam interaction with the tin coated substrate at different laser scanning speed: (a) 20 mm/min, (b) 100 mm/min. 41

Figure 4.14: High-speed images of the 85/15CuSn thin wall deposition with backlight setup: (a) beginning of first layer, (b) end of first layer, (c) beginning of second layer, (d) end of second layer. The light blue arrow highlights the detachment area from the substrate 42

Figure 4.15: Thermal distortion evaluation using 2D feature-tracking algorithm: (a) initial and (b) post-cooling raw frames captured via high-speed visible imaging; (c) processed second frame with highlighted tracked regions (colored circles) and displacement vectors. 43

Figure 4.16: Net displacement against longitudinal position (X) along the track plot for the analyzed regions of interest; the orange squares represent the stationary reference points on the baseline, while the blue squares represent the points standing on the cooled layer 44

Figure 4.17: High-speed thermal camera frames acquired during the deposition of thin 85/15CuSn bronze wall onto pre-heated tin coated copper substrate; (c) onset of detachment with highlighted thermal regions 45

Figure 4.18: Example of a frame captured by the MWIR-camera during the laser scanning 45

Figure 4.19: Fictitious temperature plot over time as derived from the MWIR-camera in a point standing along the laser scan; the plateau at around 196 °C is due to sensor saturation at high temperatures 46

Figure 4.20: Comparison between simulated ("COMSOL", dark blue) and experimentally derived ("TC#51", light blue) cooling rates 47

Figure 4.21: Cu-binary phase maps at the end of the laser track for the (a) 650 W and (b) 700 W scenarios. Green highlights the liquid phase volume, while red is the solid volume. 48

Figure 4.22: Cross-sectional view of the melt pools (green regions) as simulated by the software at the end of the laser scan for the (a) 650 W and (b) 700 W output power scenarios, with related measurements to the known depth of the sub-mesh (highlighted in red) 49

List of Tables

Table 2.1: Comparison between recent DED studies on the effectiveness of green and blue lasers for copper parts manufacturing 7

Table 2.2: Latest reported studies on the simulation of the DED process 8

Table 3.1: Input melting temperature, transition interval amplitude, and latent heat of fusion for simulated copper and tin..... 12

Table 3.2: Surface emissivity values for the simulated copper and tin 13

Table 3.3: Chemical composition of the Cu-ETP plate 14

Table 3.4: Calculated values of roughness for untreated and sandblasted copper plates..... 15

Table 3.5: Titanium Grade 1, unalloyed, chemical composition as for ASTM B265-20a [68] 16

Table 3.6: Half-cell reactions with their standard potential (E^0) and the relative equilibrium constant K_{Sn} for the oxidation of copper to copper (II). Adapted from Lindström [27] 17

Table 3.7: Detailed recipe for "C Sn0.8" solution [27] for the immersion deposition process of tin onto copper substrates 18

Table 3.8: Chemical composition of the 85/15CuSn bronze powder 20

Table 3.9: Calculated values of dynamic angle of repose (α_d), cohesive index (CI), and their respective hysteresis at different drum rotating speed 21

Table 4.1: Simulated process parameters for the laser scan experiment carried out on COMSOL Multiphysics software; T_0 is the initial substrate temperature and E is the resulting energy density of the beam 28

Table 4.2: Tested process parameters values for the optimization of the deposition of single tracks for the LB-DED process of 85/15CuSn onto roughened pure copper substrates..... 31

Table 4.3: Overview of the thin titanium sheet experiments carried out. As for the case of the 2-layer wall, the notation "x + y" stands for the different parameters used for the first (x) and the second (y) layer 34

Table 4.4: Overview of the carbon spray coated copper substrate experiments carried out 36

Table 4.5: Overview of the LB-DED experiments carried out onto the tin coated copper substrate. As for the case of the 4-layer walls, the notation "x + y" stands for the different parameters used for the first (x) and the three upper (y) layers 38

Table 4.6: Process parameters and calculated Energy Density/Laser Energy per unit Powder Feed (LEPF) values for the investigated samples from Figure 4.11 40

Table 4.7: Tested process parameters during the high-speed imaging of the LB-DED process of thin wall depositions of bronze onto the tin coated copper substrate; tests 1 and 2 refer to the different illumination modes 41

Nomenclature

Abbreviation and Acronyms

AM	Additive Manufacturing
Cu-ETP	Electrolytic Tough Pitch copper
CE	Circle Equivalent diameter
CFD	Computational Fluid Dynamics
CI	Cohesive Index
CW	Continuous Wave
DoG	Difference of Gaussians
EBM	Electron Beam Melting
EM	Electromagnetic
FEM/FVM	Finite Element Method / Finite Volume Method
IACS	International Annealed Copper Standard
LAP	Simple Linear Assignment Problem algorithm
LB-DED	Laser-Based Directed Energy Deposition
LEPF	Laser Energy per unit Powder Feed
LoF	Lack of Fusion
L-PBF	Laser Powder Bed Fusion
MWIR	Mid-Wave InfraRed
N/D	No Data
NIR	Near-infrared
P×S×C	Primary × Shaping × Carrier gas flow rate
PRS	Plate Rotation Speed
RF	Radiofrequency
RT	Room Temperature
SS	Stainless-Steel
TPMS	Triply Periodic Minimal Surfaces
WD	Working Distance

Other Symbols

α_d	Dynamic Angle of repose
α_m	Phase change step function
A	Absorptivity
C_p	Isotropic Specific Heat Capacity
$C_{\mathrm{p},eff}$	Apparent Heat Capacity
d	Laser beam Diameter
$\lvert\Delta\mathbf{r}\rvert$	Net displacement magnitude
$\Delta T_{1\to2}$	Transition zone temperature interval
ΔX	Longitudinal displacement
ΔY	Vertical deflection
ε	Surface emissivity
E	Effective energy density
E^0	Standard half-cell electrode potential
F	Faraday's constant
F_r	Powder Feed rate
h	Heat transfer coefficient
h_c	Conductance coefficient
θ_i	i-Phase fraction
Θ	Boolean function
k	Thermal conductivity
K_Sn	Equilibrium constant for tin reduction
$L_{1\to2}$	Latent Heat of phase change from 1 to 2
n	Normal coordinate
P	Laser Power
$\mathbf{q}$	Heat Flux
Q	Volumetric heat source
$\mathbf{r}$	Relative reference coordinate
r_spot	Laser spot size
ρ	Density

R	Ideal gas constant
R_a	Arithmetic mean Roughness
R_q	Root mean square Roughness
R_{ku}	Surface Kurtosis
σ	Stefan-Boltzmann constant
S	Heaviside step function
v	Laser scan speed
t	Time
T	Temperature
T_0	Preheating temperature
T_{ext}	Ambient Temperature
$T_{pc,1\rightarrow2}$	Phase change Temperature
wt.%	Weight percentage
(X, Y, Z)	LB-DED Machine Reference Frame
X_c, Y_c	Laser coordinates
X_{end}	Final x-position of the laser
z	Number of electrons

1 Introduction

A gyrotron is a high-power vacuum electronic oscillator that converts energy from a magnetized, gyrating electron beam into coherent millimeter-wave or subterahertz electromagnetic radiation [1] (Figure 1.1). The current continuous wave state-of-the-art gyrotron technology is 1.3 MW at 140 GHz for long-pulse industrial operation [2]. However, to increase plasma confinement efficiency in magnetic fusion reactors (e.g. Tokamaks or Stellarators) the EUROfusion Consortium, which is responsible for the drafting of the European Fusion Roadmap to fusion electricity, explicitly targets 230 – 240 GHz with 1 – 2 MW RF power output [3].

The interaction cavity (resonator) is the short section where the electron beam and the electromagnetic field exchange energy efficiently. A typical cavity is 1 – 5 cm in diameter, and similar in length (although the electron-wave coupling is strongly localized axially in ~ 1 cm [4]).

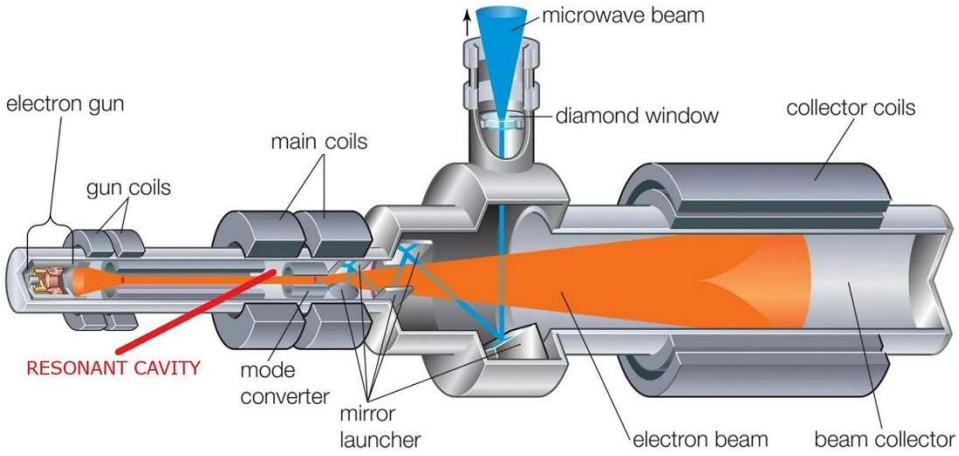


Figure 1.1: Schematic view of a gyrotron, with its main components [5]

Cavity heating is dominated by ohmic losses at the conducting wall: a current is induced by the oscillating field on the cavity surface, flowing in a thin “skin” layer, where resistive dissipation becomes heat that must be removed continuously in CW/long-pulse operation. The density of ohmic losses increases approximately linearly with increasing the wave output power. However, it increases with the power of 5/2 with respect to the operating frequency [1], [6]. This is why moving to > 200 GHz makes cavity thermal management a priority. Moreover, multiphysics studies explicitly state that thermal deformation of the cavity alters the electromagnetic field structure and can affect gyrotron operation, which is why coupled EM–thermal–mechanical modelling is used for design and qualification [4], [7].

Given these premises, the cavity material must have high electrical and thermal conductivity to decrease attenuation and ohmic losses [8] and must withstand high temperature to avoid deformation. Glidcop, an oxide-dispersion strengthened copper

alloy, is widely used for high-heat-flux applications [9] and its Glidcop AL-15® alloy (0.15 wt.% of nanometric alumina particles dispersion) is the current gyrotron cavity material benchmark [10]. The oxide nano particles act as obstacles to dislocation motion and therefore they increase the creep resistance of pure copper, while maintaining ~ 92% IACS.

Common design constraints fix the peak Ohmic wall loading at cavity to ≤ 2 kW/cm^2 and the maximum temperature to avoid damages to < 250 °C [3], [10], [11]. Different strategies have been implemented during the years to effectively cool the cavity to the desired operating temperature (Figure 1.2, [12]). Typical coolant conditions described are subcooled water at room temperature, weakly pressurized (order of a few tenths of MPa [7]).

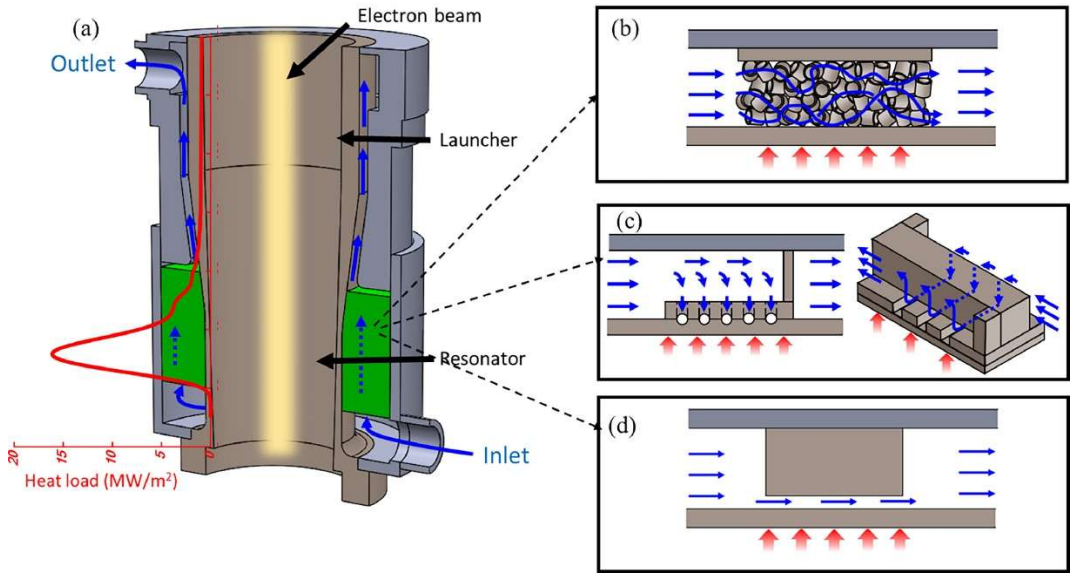


Figure 1.2: (a) 3D sketch of the resonant cavity and a portion of the launcher, with the profile of a heat load released on the inner wall. The green volume represents the area devoted for cooling: (b) Raschig Rings cooling, (c) azimuthal micro-channels cooling, (d) longitudinal mini-channels cooling (modified from [12])

Future requirements oriented towards heat loads from 2.5 to 3 kW/cm^2 [13] pushed the research to develop new cooling designs which could increase heat-removal capability without introducing unacceptable pressure drop, mechanical stress, or manufacturability risk. Triply Periodic Minimal Surfaces (TPMS) geometries are porous cellular structures with high contact-area-to-volume ratio (Figure 1.3) which makes them interesting in the thermal management field [14]. It has already been proved that TPMS structures can remove 11 – 28 % more energy from the heated surface of the divertor than a conventional circular channel [15]. However, these continuous structures are impossible to be conventionally manufactured.

Additive Manufacturing (AM) is well known to enable intricate near-net-shape parts production with much greater design freedom. It consists of layer-by-layer construction of parts from a digital model, allowing minimal material waste [16]. Its fields of application now cover a broad range of materials (polymers, metals, ceramics and even organic tissues) and the main technologies are listed in Figure 1.4. Build volume,

required resolution and surface quality, production rate, materials and type of energy source are key factors while selecting the suitable AM technique.

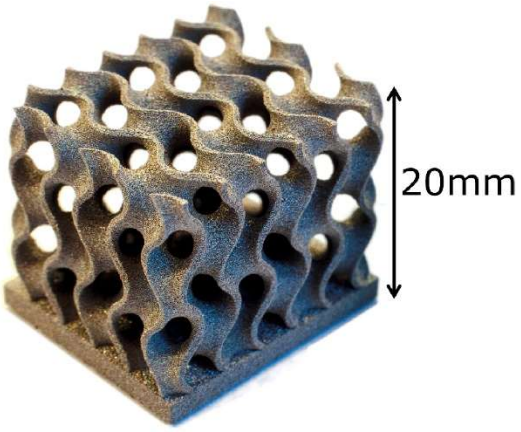


Figure 1.3: Additively manufactured tungsten gyroid TPMS structure [17]

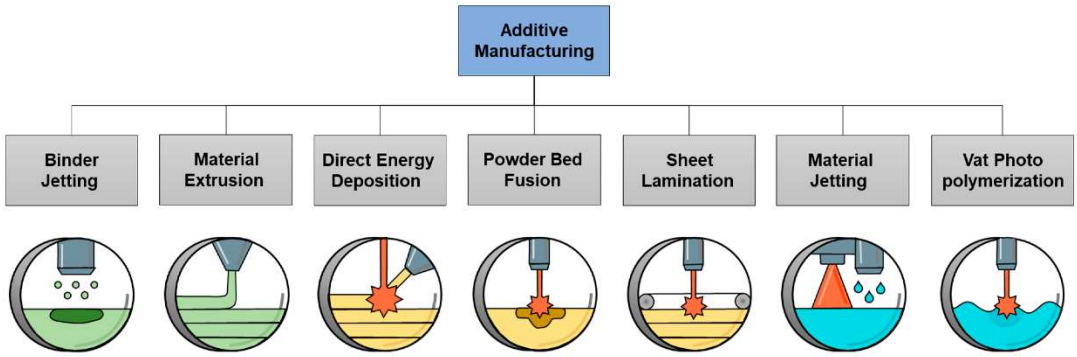


Figure 1.4: Main types of additive manufacturing (AM) processes according to ASTM F2792—12a [18].

Among the different metal AM methods, those employing powder-based feedstocks are the most widely used: Powder Bed Fusion (PBF) and Directed Energy Deposition (DED) [19], [20]. In PBF processes, such as Laser-PBF (L-PBF) and Electron Beam Melting (EBM), respectively a laser and an electron beam are used as a focused energy source to selectively fuse regions in a powder bed: subsequent layers of powder are alternatively deposited and melted to create the programmed part [21]. Conversely, for DED, the powder (or wire) feedstock is delivered directly into the melt pool which is generated by a high energy density heat source (laser, electron beam, or plasma/electric arc) [22]. In both cases, the consolidation of the powder occurs after the almost instant solidification of the melt pool. A visual comparison between the two discussed AM technologies is reported in Figure 1.5. While PBF generally achieves better feature resolution thanks to finer powders and highly focused beams, allowing the printing of internal channels and overhanging structures, its build volume is limited by the machine chamber (usually around 250 × 250 × 500 mm), the production time is relatively long and post-processing is often needed (removal of building supports, thermal treatments and surface finishing) [16]. On the other hand, DED is preferred to fabricate large-scale components up to several meters and

weights of kilograms at higher deposition rates, combining the higher feedstock flexibility as wire/rod can be used too or multiple powder hoppers at the inlet have been used for multi-material printing, functionally graded components, combinatorial materials development, and site-specific composition control [23]. Repairing and/or reinforcing/coating of already existing parts is another field of application for this technique.

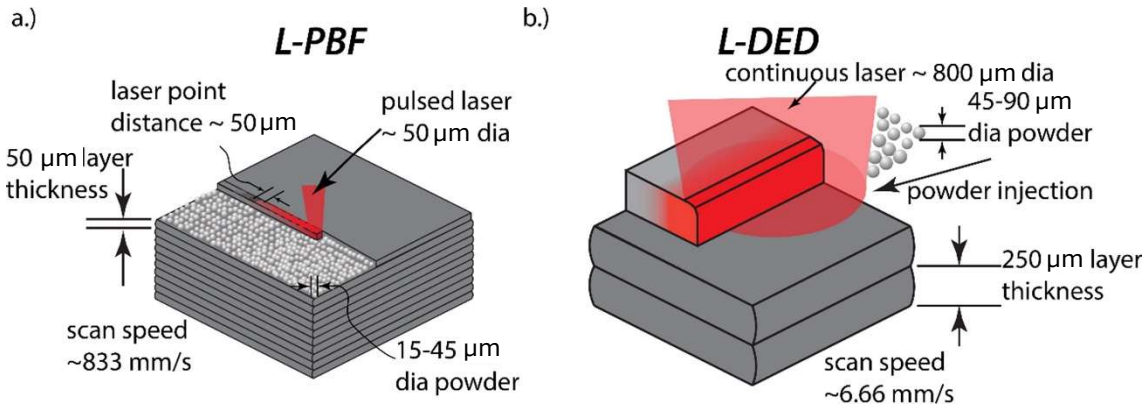


Figure 1.5: Schematic views of pulsed Laser-PBF (a) and Laser-DED (b) [23]

The major drawbacks of DED are lower part resolution given by larger melt pool size, increased layer thickness, and wider hatch spacing, as well as low powder deposition efficiency, leading to high material wastage [24].

The same reasons that make copper and copper-alloys interesting for thermal management systems set the biggest challenges for AM processes. Indeed, the intrinsic high thermal conductivity of copper and low absorptivity in the Near-InfraRed (NIR) spectrum (≤ 5 % at 1064 nm for untreated solid copper surface [25]) of the most common equipped laser systems of AM machines make the complete melting of the powders harder. This is even more complicated in DED if powder shadowing is taken into account [24]. When increasing the input power and reducing the scanning speed of the laser is not sufficient to obtain dense parts, new techniques have been implemented to increase laser absorptivity: for L-PBF, both carburized [26] or Tin/Nickel coated [27] copper powder exhibited enhanced NIR-laser absorptivity, leading to ≥ 99 % part density; for DED, when the deposition is made onto copper substrates, increasing the surface roughness led to better absorptivity, allowing effective melting of the first layer [28]. However, when equipped, green and blue lasers solve the reflectivity problem by shifting the heat source to much higher copper absorptive spectra [29].

The present study investigates the feasibility of L-PBF and LB-DED printing of copper-alloy powders onto pure copper substrates, highlighting how process parameters and surface treatments can affect the production of future parts. This work will be a step forward for the future realization of complex cooling structures for gyrotron cavities for the next generation of high-frequency fusion nuclear reactors.

2 LB-DED of Copper and Copper Alloys

This chapter provides a brief overview of the current state of the art of Laser Based-DED of copper and copper alloys, the main challenges reported in literature, the most common adopted strategies to obtain dense parts, and how software simulation is used to accelerate the development and optimization process.

2.1 NIR LB-DED of copper and copper alloys: challenges and strategies

For Near-InfraRed Directed Energy Deposition (NIR-DED), the main barriers are the intrinsic low absorptivity of pure copper near 1060-1080 nm, the rapid heat extraction due to remarkable thermal conductivity, and the narrow stable melting window. Therefore, the research focuses on two alternative routes which are often coupled to obtain dense parts: surface texturing/modification of the substrate and surface modification/coating of powders. However, the most direct way to increase absorptivity remains moving to the visible spectrum, where copper exhibits lower reflectivity with green and blue laser systems.

2.1.1 The narrow stable melting window

Many studies have been correlating low NIR absorption and rapid heat dissipation to incomplete melting and lack-of-fusion (LoF) porosity in additively built copper parts [29], [30], [31]. Increasing the input energy can also fail, as keyhole porosity and copper vaporization can occur [32], [33]. Effective energy density, E (J/mm^2), is a common parameter utilized as a correlating factor between the processing parameters and continuous deposition and deposit aspect ratio for the DED process[22]:

$$E = \frac{P}{vd} \tag{2.1}$$

where P is the laser power (W), v is the laser scan speed (mm/s), and d is the laser beam diameter (mm). Khandpur et al. [29] explicitly states that "the optimal energy density window is relatively narrow".

Noting that a single universally high-power setting is not sufficient on its own, careful considerations must be taken regarding the scanning strategy. Yadav et al. [34] achieved 99.9 % relative density during pure copper LB-DED using an increasing Laser Energy per unit Powder Feed (LEPF (J/g), as defined in Equation 2.2, where F_r is the powder feed rate (g/s) and P is the laser power) interlayer scheme. This strategy compensates for the different thermal conditions between the steel substrate and the so-deposited copper layers, and it was similarly successfully adopted in other studies [32].

$$LEPF = \frac{P}{F_r} \tag{2.2}$$

2.1.2 Surface texturing/modification of the substrate

As is the case in the current study, the additively deposited structure is built on top of a copper alloy substrate, with the oxide dispersed phase counting only for the 0.15 wt.% in a pure copper matrix. It is widely known that metal surface roughness is directly proportional to laser absorptivity [35], [36], and surface texturing methods, such as deep grinding, etching and sandblasting, have already shown their effectiveness in decreasing laser reflectivity in both pure copper and high copper alloy. Felicioni et al. [28] reported a 27 % absorptivity at 1070 nm wavelength for a "deep grinded" pure copper substrate, while Zhang et al. [37] achieved 80.7 % absorptivity at 1080 nm wavelength for a laser-etched CuCr0.8 substrate (Ra = 15.2 ± 0.6 µm, Figure 2.1).

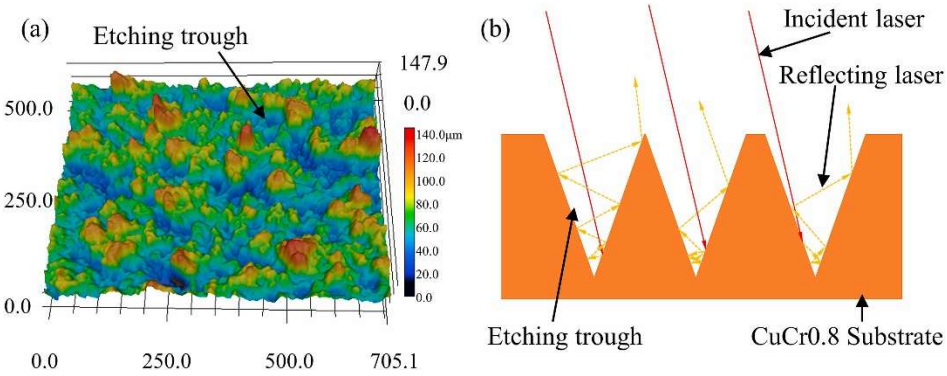


Figure 2.1: (a) 3D morphology of a laser-etched surface, (b) schematic representation illustrating laser absorption enhancement. Adapted from Zhang et al. [37]

The surface can be chemically modified, and higher absorbing materials can be deposited onto the substrate. In the same study mentioned above, Zhang et al. [37] successfully deposited a ~200 µm thick cold sprayed coating of a Ni-based alloy (Inconel 625) on top of a CuCr0.8 substrate to achieve 66.2 % laser absorptivity at 1080 nm wavelength.

2.1.3 Surface modification/coating of powders

While most of the literature focuses on copper powder surface modification for L-PBF, investigating the positive effects of oxidation, nitridation, and carburization, as well as thin coatings of tin, nickel, and yttria, and powder nanotexturing [38], [39], [26], [40], [41], [27], [42], [43] to increase laser absorptivity, the DED-specific literature remains far less mature. In a recent LB-DED study from 2024, Sharma et al. [44] showed how <0.1 wt.% graphene-reinforced copper powders raised the NIR absorptivity to around 60 %, enabling the deposition of defect-free tracks at 750 W laser power onto a rolled copper plate. However, increasing the graphene content above

0.1 % led to keyhole porosity due to excess energy input, confirming once again how narrow the process window is while working with this kind of material.

2.1.4 Overcoming the absorptivity problem: green and blue lasers

Figure 2.2 shows the absorptivity of pure copper as a function of wavelength. As is highlighted by the vertical lines the absorptivity in the blue (~450 nm) and in the green (~515 nm) spectrum is around nine to ten times greater than the conventional NIR spectrum (~1080 nm). While industrial translation toward high-brightness blue laser sources for DED (up to 500W) is still under process [45], high-power green systems are already described as commercially available. Successful deposition of pure copper tracks onto a pure copper substrate was obtained by Prasad et al. [46] with the following process parameters: 1 kW green laser beam power (spot size = 1.7 mm), 0.1 m/min cladding speed, and 1.3 g/min powder feed rate.

The first well-defined geometries built by powder-fed-DED with a blue laser were obtained by Liu et al. [47] in 2023 onto stainless steel substrates, and the process parameters used are listed in Table 2.1, which also gives a comparison between the two mentioned laser systems.

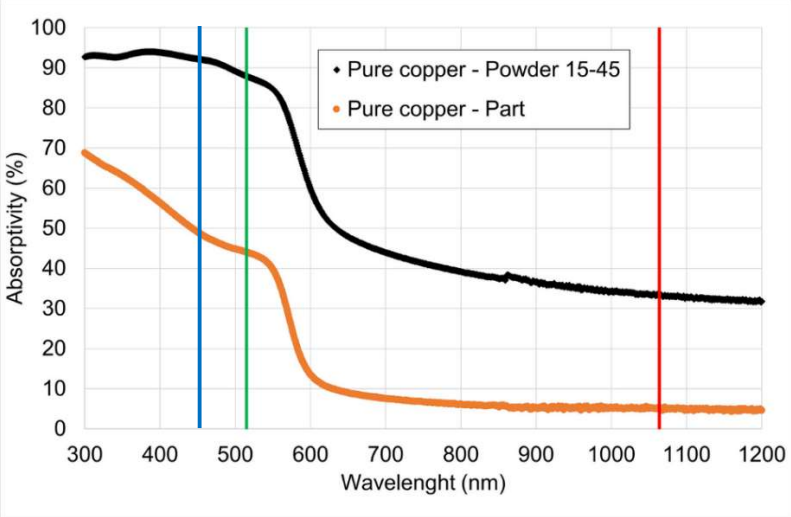


Figure 2.2: Absorptivity of pure copper as a function of wavelength for: SLM produced parts (orange), powder sample of D10 = 15 µm and D90 = 45 µm (black). Adapted from Domine et al. [48].

Table 2.1: Comparison between recent DED studies on the effectiveness of green and blue lasers for copper parts manufacturing

Authors	Part	Substrate	Laser Source (spot size)	Laser Power (W)	Scanning Speed (mm/min)	Powder Feed Rate (g/min)	Relative Density (%)
Prasad et al. [46]	Single track	Pure copper	Green (1.7 mm)	1000	100	1.3	N/D
Liu et al. [47]	Cube	AISI 304	Blue (1 mm)	650	1000	3	99.6

However, neither green nor blue laser sources were available at Empa facilities. Therefore, this approach could not be assessed within this study.

2.2 Simulation of the DED process

Thermal gradients, residual stresses, and melt-pool dynamics are often difficult to predict and observe experimentally. Coupled thermo-mechanical with computational fluid dynamics (CFD) using finite element method (FEM) or finite volume method (FVM) are therefore used by researchers to model these multi-physics phenomena. Software packages to simulate LB-DED are commercially available, and some of the work developed during the last years is reported in Table 2.2 highlighting the key features of each software package used.

Table 2.2: Latest reported studies on the simulation of the DED process

Software	**Numerical Method**	**Modelling Focus**	**Authors**
Abaqus	FEM	Thermo-mechanical analysis, distortion, and residual stresses	Hammouda et al. [49], Çiğir et al. [50]
COMSOL	FEM	Heat transfer modeling	Nain et al. [51]
SIERRA	FEM	Coupled solid-fluid-mechanics for deposition shape and stress	Beghini et al. [52]
Simufact Welding	FEM	Thermo-mechanical behavior and heat treatment mapping	Çallı et al. [53]
SolidWorks Simulation	FEM	Temperature field prediction	Karpovich et al. [54]
Star-CCM+	FVM/FEM	Melt pool evolution and free-surface tracking	Panicker et al. [55]

The developed models are mainly used for predicting the thermo-mechanical behavior of the deposited material, and process parameters optimization can be achieved to mitigate the induced distortion and residual stresses. CFD models can solve melt pool dynamics, including Marangoni convection and recoil pressure. The latter were also effectively implemented to optimize nozzle geometry, improving powder supply efficiency from 50.2 to 66.0 % [56]. Generally, the simulation workflow always includes validating the predictive models against experimental data.

Coupling thermos-mechanical and CFD models together remains difficult as simulating large DED parts requires large amounts of data management. Thermal cycle heat input, multi-layers lumping, and spatial reduction methods from three to two-dimensional problems are just some of the implemented simplification strategies to keep the computational time and data acceptable [57].

It is still important to note that simulation provides a solid framework for DED process parameters optimization, reducing the reliance on costly trial-and-error experiments [58].

3 Materials and Methods

This chapter provides the complete overview of the materials and methods that were used during the study. The LB-DED process consisted of deposition of bronze powder onto surface-modified pure copper substrates. FEM based simulations were performed to investigate the substrate thermal field evolution during the laser process.

3.1 Simulation of the LB-DED Process

COMSOL Multiphysics v6.4 software (COMSOL, Stockholm, Sweden) was used to perform thermal simulations of the LB-DED process and the thermal field evolution of the copper substrate was investigated during the laser scanning. The simulations carried out helped to understand whether a near infrared laser system with a nominal maximum output power of 500 W was suitable to melt the copper substrate and to sustain the melt pool. Three substrate surface cases were investigated: untreated, sandblasted and tin coated. The data collected from the simulation was later compared to experimentally acquired data from an infra-red thermal camera to validate the model. A schematic representation of the 3D FE model showing the substrate geometry, laser scanning direction, and governing thermal boundary conditions is reported in Figure 3.1.

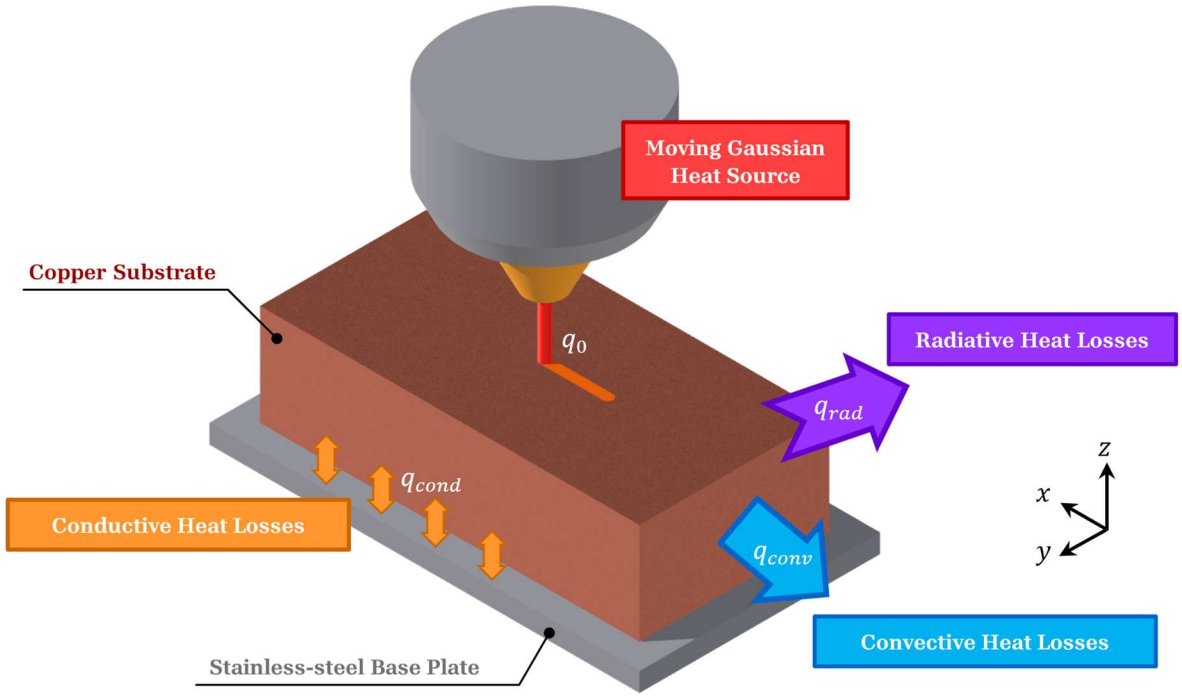


Figure 3.1: Schematic representation of the 3D thermal FE model highlighting the moving Gaussian laser heat source (q_0), conductive heat dissipation to the stainless-steel base plate (q_{cond}), and convective (q_{conv}) and radiative (q_{rad}) heat losses to the ambient

3.1.1 Thermal Model Setup

Described below are the governing equations along with the initial conditions, the heat input model and the thermal boundary conditions required to resolve the temperature field throughout the 3-dimensional DED process, when no powder is deposited and the laser is assumed as a surface heat flux.

3.1.1.1 Thermal equilibrium

For a given body of density, ρ, and isotropic specific heat capacity, C_p, the thermal equilibrium is given by:

$$\rho C_\mathrm{p} \frac{dT}{dt} + \nabla \cdot \mathbf{q}(\mathbf{r}, t) = Q(\mathbf{r}, t) \tag{3.1}$$

where t is time, T is temperature, $\mathbf{q}$ is the heat flux, $\mathbf{r}$ is the relative reference coordinate, and Q is the body heat source. The initial condition is set to $T_{ref} = T_{ext}$, where T_{ext} is the ambient temperature (or preheating temperature if considered in the model). The boundary conditions consist of the applied heat source and the surface heat losses due to conduction with the substrate, thermal radiation and convection.

The distribution of heat through the body is given by Fourier's conduction equation:

$$\mathbf{q} = -k\nabla T \tag{3.2}$$

where k is the isotropic temperature-dependent thermal conductivity.

3.1.1.2 Moving Laser Heat Source

The DED laser has been modeled as a moving 2D Gaussian heat source. The boundary condition has been set as a general inward heat flux ($\mathrm{q_0}$, W/m^2) on the upper surface of the modelled substrate, as reported in Equation 3.3.

$$\mathrm{q_0}(x, y, t, T) = -k\left(\frac{\partial T}{\partial n}\right) = \frac{2P_\mathrm{laser}A(T)}{\pi r_\mathrm{spot}^2} \exp\left(-2\frac{\left(x - X_c(t)\right)^2 + (y - Y_c)^2}{r_{spot}^2}\right) \tag{3.3}$$

where x and y are the in-plane coordinates, n is the coordinate along the outward normal direction from the plane, P_laser is the laser output power (W), $A(T)$ is the absorptivity of the substrate as a function of temperature, and r_spot is the laser spot size at focus (m). As the laser is moving along the x coordinate, its central coordinates (X_c, Y_c) are a function of time and scanning speed, v (m/s):

$$\begin{cases} X_c(t) = X_0 + v \cdot t \\ Y_c = Y_0 \end{cases} \tag{3.4}$$

where X_0 and Y_0 are the laser starting position coordinates.

In order to reach the convergence at the starting point a smoothed (transition zone of 1×10^{-4} s) Heaviside step function (S) has been added to the definition of $\mathrm{q_0}$, and a logical expression, Θ, acts as a Boolean switch, returning 1 for $X_c(t) \leq X_\mathrm{end}$ during the

active scan and 0 upon reaching the end of the track. The final expression of the heat source is then reported in Equation 3.5.

$$q_0(x, y, t, T) = q_0(x, y, t, T) \cdot S(t) \cdot \Theta(X_{\text{end}} - X_c(t)) \tag{3.5}$$

3.1.1.3 Phase Change Material Modelling

To manage the melting of copper substrate or the tin layer and their consequent phase change without having to remodel the mesh each time, COMSOL allows the implementation of the apparent heat capacity method [59]. The latent heat of fusion ($L_{1\to2}$) absorption is integrated by changing the standard specific heat capacity of the material (C_p) to an equivalent one ($C_{p,eff}$) spread over a transition interval ($\Delta T_{1\to2}$):

$$C_{p,eff}(T) = \theta_1 C_{p,1} + \theta_2 C_{p,2} + L_{1\to2}\frac{\partial \alpha_m}{\partial T} \tag{3.6}$$

where θ_i is the fraction of the i-phase at temperature T (given by a smoothed Heaviside function along the transition interval, Figure 3.2), and α_m is a smoothed temperature-dependent step function which formulation is reported in Equation 3.7.

$$\alpha_m(T) = \begin{cases} 0 & T < \left(T_{pc,1\to2} - \dfrac{\Delta T_{1\to2}}{2}\right) \\ \dfrac{1}{2}\dfrac{\theta_2 - \theta_1}{\theta_1 + \theta_2} & \left(T_{pc,1\to2} - \dfrac{\Delta T_{1\to2}}{2}\right) \le T \le \left(T_{pc,1\to2} + \dfrac{\Delta T_{1\to2}}{2}\right) \\ 1 & T > \left(T_{pc,1\to2} - \dfrac{\Delta T_{1\to2}}{2}\right) \end{cases} \tag{3.7}$$

where $T_{pc,1\to2}$ is the phase change temperature (or melting temperature in this case).

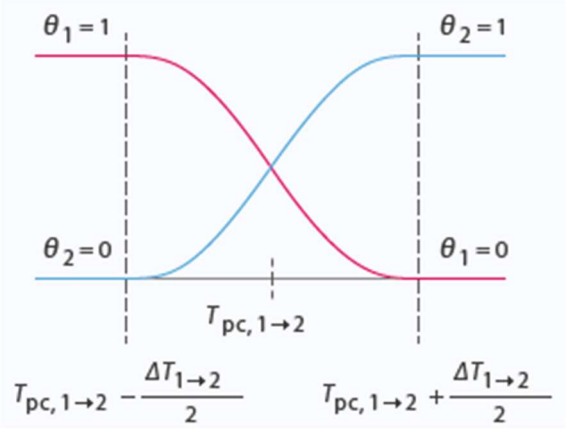


Figure 3.2: θ_1 and θ_2 Heaviside step functions evolution over the transition interval as is displayed from COMSOL software

Moreover, thermal conductivity and density of the material are replaced by equivalent values in the transition zone, and they are calculated as a mix of the properties of both phases (respectively ρ_1, k_1 for the solid phase and ρ_2, k_2 for the liquid phase):

$$\rho_{eff}(T) = \big(1 - \alpha_m(T)\big)\rho_1 + \alpha_m(T)\rho_2 \tag{3.8}$$

$$k_{eff}(T) = \big(1 - \alpha_m(T)\big)k_1 + \alpha_m(T)k_2 \tag{3.9}$$

The input values used to simulate the phase change occurring during melting for both copper and tin are listed in Table 3.1. The transition interval amplitudes for both tin and copper have been kept deliberately relatively wide to allow convergence of the 3D-model in reasonable computational time.

Table 3.1: Input melting temperature, transition interval amplitude, and latent heat of fusion for simulated copper and tin

Material	$T_{pc,1\to2}$ (K)	$\Delta T_{1\to2}$ (K)	$L_{1\to2}$ (kJ/kg)
Copper	1357.77	20	205 [60]
Tin	505.08	15	59.21[61]

Density, thermal conductivity, specific heat capacity, and absorptivity at laser wavelength of the materials investigated were determined as a function of temperature and given as input to the model.

3.1.1.4 Temperature-dependent Material Properties

The material properties required in solving the governing Equations 3.1 and 3.2 were searched in literature or evaluated from Thermo-Calc simulation (Thermo-Calc Software, Solna, Sweden), and their trends as a function of temperature are reported in Appendix A. The absorptivity of both copper (in the case of untreated surface and sandblasted surface) and tin were also evaluated from literature as a function of temperature and their trends are reported in Appendix A.

3.1.1.5 Boundary Conditions

During the studied process heat losses occur due to thermal radiation, free convection, and conduction through the base plate which the substrate is fixed on.

The free convective heat flux (q_{conv}) is modeled with Newton's law of cooling, and it is applied on every surface exposed to the chamber environment:

$$q_{conv} = h(T - T_{ext}) \tag{3.10}$$

where h is the convective heat transfer coefficient, which is assumed to be 10 W/(m^{2}K) for free convection of both copper and tin with air during the DED process [62].

The thermal radiation is described by Stefan-Boltzmann law:

$$q_{rad} = \varepsilon\sigma(T^4 - T_{ext}^4) \tag{3.11}$$

where ε is the surface emissivity and σ is the Stefan-Boltzmann constant (σ = 5.67 × 10^{-8} W/(m^{2}K^4). The input values for surface emissivity of both copper and tin are listed in Table 3.2. As the surfaces of the copper substrate were roughened and preheating was simulated, its emissivity was purposely chosen as in the case of oxidized copper.

Table 3.2: Surface emissivity values for the simulated copper and tin

Material	ε [63]
Copper (oxidized)	0.65
Tin	0.05

The fixture and the thermal conduction between the substrate and the stainless-steel (SS) base plate (which acted as the heating plate too) was approximated as a convection loss (q_{cond}) [64]. Due to the lack of tabulated literature values for the dissimilar Cu-SS pair, an intermediate conductance coefficient, h_c = 3,500 W/(m^{2}K) was adopted, chosen between benchmark values for homogeneous copper/copper and stainless-steel/stainless-steel contacts [65].

$$q_{cond} = h_c(T - T_0) \tag{3.12}$$

where T_0 is the base plate temperature, or preheating temperature.

3.1.2 High-Speed Thermal Camera Setup

To validate the simulation model, infrared thermography has been performed with a high-speed Mid-Wave InfraRed (MWIR) camera (Telops Fast M3K, Telops, Québec, Canada). Thermal sequences were acquired at a resolution of 64×64 pixels and a frame rate of 7,194 Hz. The camera features an InSb detector operating in the 3-5.5 µm spectral range, equipped with a Telops G1X lens (f/3.0, working distance of 260 mm). The system accuracy is given by its thermal sensitivity, which is lower than 25 mK. A lower-temperature filter configuration was selected to maximize thermal resolution during the cooling stage. Although this resulted in data saturation at peak temperatures, this regime was deprioritized due to system's intrinsic reduced accuracy at high temperatures. Optical access to the melt pool was obtained through an uncoated calcium fluoride (CaF_2) window with a diameter of 120 mm and a thickness of 2 mm. The window maintains the chamber environment isolated from the outside, while allowing 95 % total transmittance in the studied infrared region for the selected thickness (manufacturer specifications). The IR-camera was positioned at a fixed angle of 45 ° with respect to the substrate. An illustration of the experimental setup is reported in Figure 3.3. Thermal measurements were conducted during laser scanning without powder to evaluate the induced thermal field in the substrate, as well as during actual deposition runs to investigate process-induced thermal distortion and substrate detachment.

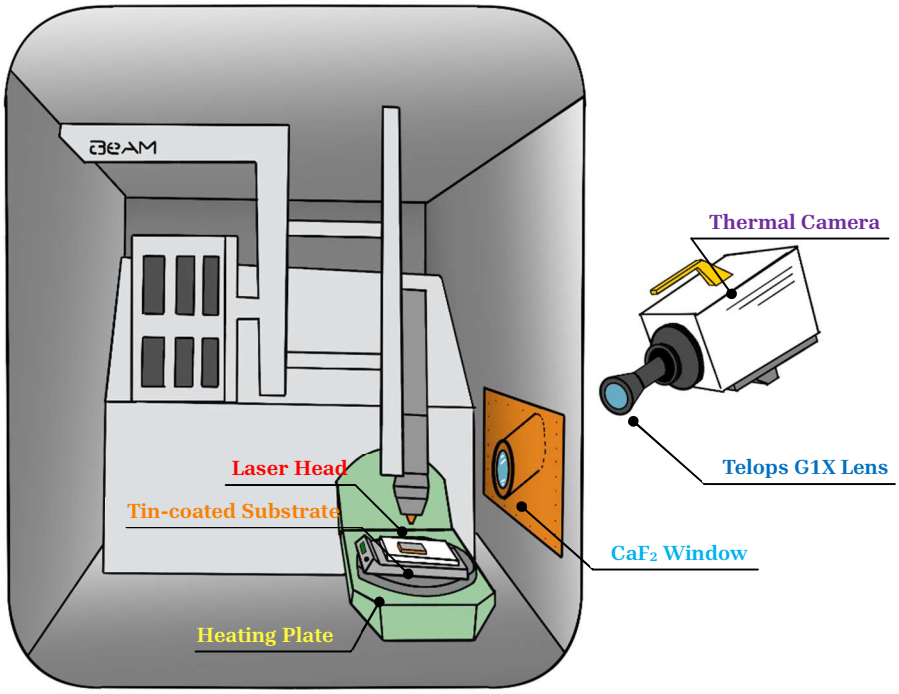


Figure 3.3: Schematic sketch of the setup used for the infrared termography of the LB-DED process

It should be noted that thermal data reflected apparent temperatures assuming an ideal blackbody emissivity ($\varepsilon = 1.0$), since no calibration with material-specific emissivity values was performed. However, because this investigation focused strictly on comparing cooling rates rather than quantifying absolute temperatures, the relative temperature dynamics and derivative cooling trends remain fully consistent.

3.2 Substrate Material

The LB-DED depositions were all obtained onto electrolytic tough pitch copper (Cu-ETP, CW004A) plates with dimensions of 50 × 100 mm^2 and a nominal thickness of 8 mm. The supplier (Thyssenkrupp Schulte GmbH, Essen, Germany) provided the chemical composition listed in Table 3.3.

Table 3.3: Chemical composition of the Cu-ETP plate

Element	Cu	Bi	O	Pb
wt.%	≥99.90	≤0.0005	≤0.040	≤0.005

Various surface treatments were applied to the copper substrate to maximize laser absorptivity and minimize back-reflection. These strategies included sandblasting, the use of a sacrificial titanium starter foil at the scan initiation point, and surface modification using either a carbon spray coating or an immersion-deposited tin layer.

3.2.1 Surface Sandblasting

As already mentioned in Chapter 2.1.2, higher surface roughness of the substrate enhances laser absorptivity. Sandblasting (or abrasive blasting) consists of a propelled stream of abrasive particles which are forcibly shot under high pressure against a smooth surface to roughen it. A sandblasting machine (Nordblast S.r.l., Model 3D7, operating pressure of 4 bar) equipped with corundum particles (grit size FEPA F120) was used and the resulting roughness profile was captured with the S-neox 3D optical profilometer (Sensofar, Barcelona, Spain) (Figure 3.4). Specific roughness values for both the untreated and the sandblasted surfaces are listed in Table 3.4.

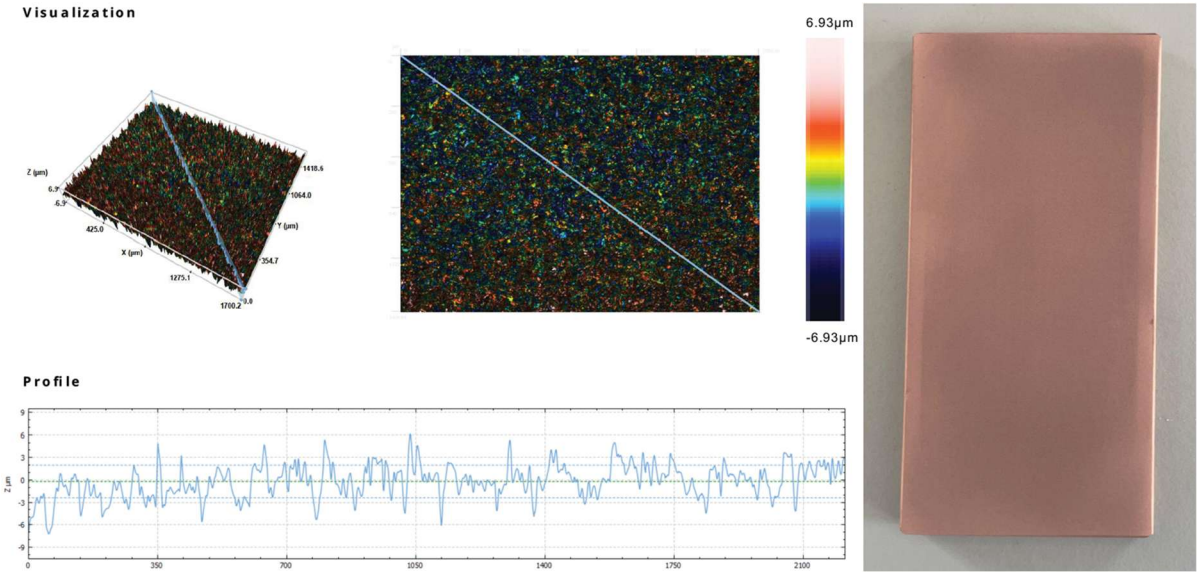


Figure 3.4: Surface profile analysis after sandblasting (left), and a sandblasted copper plate (right)

Table 3.4: Calculated values of roughness for untreated and sandblasted copper plates

Substrate type	R_a (µm)	R_q (µm)	R_{ku}
Untreated	0.7073	0.8608	2.7128
Sandblasted	1.7669	2.3164	8.5880

Sandblasting increased R_a to 1.77 µm and significantly elevated the kurtosis (R_{ku}) up to 8.59. This leptokurtic morphology (R_{ku} > 3) indicates sharp peaks and deep crevices that promote light trapping, effectively enhancing laser coupling into the copper substrate.

3.2.2 Titanium Sheet

Pure titanium (Grade 1, chemical composition given in Table 3.5) shows great absorptivity at 1070 nm (around 40 % as for Linden et al. [66]).

Table 3.5: Titanium Grade 1, unalloyed, chemical composition as for ASTM B265-20a **[67]**

Element	Ti	C	O	N	H	Fe	Others
wt.%	≥99.1	≤0.08	≤0.18	≤0.03	≤0.015	≤0.20	≤0.40

A thin titanium sheet of dimensions 10×20 mm^2 and thickness of 0.5 mm, was clamped onto the roughened pure copper substrate (Figure 3.5). The sheet was positioned at the beginning of the scanning track, and the objective was to start the melt pool in the titanium slab, transferring the heat to the copper substrate to both directly, through the laser, and indirectly, through conduction, melting it. Indeed, molten copper shows slightly better absorptivity at 1070 nm than when it is solid due to intrinsic wavier metal surface [68], allowing, in principle, for a longer continuation of the melt pool.



Figure 3.5: Thin titanium sheet clamped on the roughened pure copper substrate inside the LB-DED chamber

3.2.3 Carbon spray coating

Kontakt Chemie's (CRC Industries Europe, Zele, Belgium) Graphit 33 conductive coating was used to create a uniform carbon sprayed coating on top of the pure copper substrate. The deposition was made by shaking, spraying and air drying for 1-2 minutes.

3.2.4 Immersion deposition of tin

The Cu-ETP substrate was coated with a thin layer of tin with an immersion deposition method. This process works by having a metal salt in aqueous solution reacting with the copper, depositing the metal by reduction and dissolving the copper ions in the solution by oxidation. The salt used is tin (II) chloride ($SnCl_2$, anhydrous, ≥97%, Sigma-Aldrich) and the combined redox reaction is presented in Equation 3.13.

$$Sn^{2+}_{(aq)} + Cu \overset{K_{Sn}}{\rightleftarrows} Cu^{2+}_{(aq)} + Sn \tag{3.13}$$

The standard half-cell electrode potentials (E^0) for the reaction are listed in Table 3.6 [27] together with the equilibrium coefficient (K_{Sn}) calculated from the Nernst equation:

$$\ln K_{Sn} = \frac{zFE^0}{RT} \tag{3.14}$$

where z is the number of electrons transferred during the redox reaction (two between tin and copper), R is the ideal gas constant, T is the temperature and F = 96,485 C mol^{-1} is the Faraday constant.

Table 3.6: Half-cell reactions with their standard potential (E^0) and the relative equilibrium constant K_{Sn} for the oxidation of copper to copper (II). Adapted from Lindström [27]

Reaction	E^0	K_{Sn} for reduction of Cu
$Sn^{2+} + 2\,e^- \rightleftharpoons Sn$	-0.13 V	1.5×10^{-16}
$Cu^{2+} + 2\,e^- \rightleftharpoons Cu$	+0.34 V	

The equilibrium constant is extremely small and in order to shift the equilibrium towards the right a lixiviant is added: thiourea (CH_4N_2S, ≥99%, Sigma-Aldrich), which can form a strong complex with copper ions, increasing the deposition rate following Le Chatelier's principle. The complexation reaction is intricate, consisting of many competing reactions with different kinetics [69], but it is however generally accepted [70], [71] that the reaction takes place through the two steps proposed in Equation 3.15 and Equation 3.16.

$$Cu^{2+} + 2\,CS(NH_2)_2 \rightleftarrows Cu^{+} + (CS(NH_2)_2)^{+}_2 \tag{3.15}$$

$$Cu^{+} + 4\,CS(NH_2)_2 \rightleftarrows Cu[CS(NH_2)_2]^{+}_4 \tag{3.16}$$

Once it is active, the complex is very stable, and the stability constant has been reported to be above $1 \times 10^{15.4}$ [71]. A schematic illustration of the complexation process is reported in Figure 3.6.

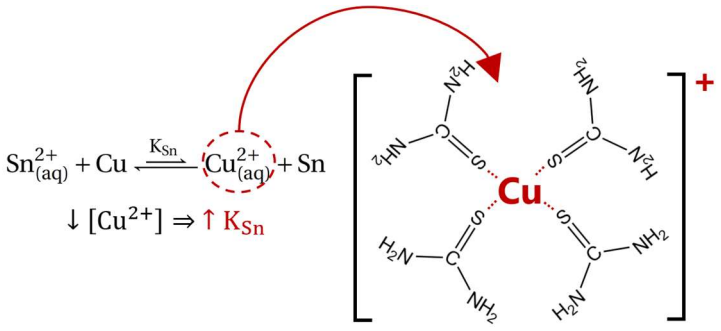


Figure 3.6: Schematic illustration of the complexation process. The copper ions are captured by the thiourea, and the reaction is shifted towards the tin deposition by reduction of the dissolved salt

Two solutions were prepared for the immersion deposition process following "C Sn0.8" Lindström recipe (Table 3.7), which led to uniform deposition of the absorbing tin layer onto pure copper powders for L-PBF [27]:

- Solution 1: deionized water (pre-boiled for 5 minutes to deoxidize) and dissolved thiourea.
- Solution 2: deionized and deoxidize water, tin (II) chloride and hydrochloric acid to avoid oxidation of the salt.

Table 3.7: Detailed recipe for "C Sn0.8" solution [27] for the immersion deposition process of tin onto copper substrates

Reactant	Thiourea	Tin (II) Chloride	Hydrochloric Acid
Molar Concentration	0.41 M	76 mM	0.40 M

The experimental steps taken for the immersion deposition of tin onto copper substrates are illustrated in Figure 3.7 and they consist of:

- 5-minute immersion of the copper substrate in acetone to degrease the surface (Figure 3.7a)
- Immersion of the substrate in a 2 % aqueous solution of hydrochloric acid (HCl) to deoxidize the surface (Figure 3.7b)
- Deoxidation of the deionized water by boiling and dissolution of thiourea (Solution 1) (Figure 3.7c)
- Immersion of copper substrate in Solution 1 and cooling to the desired reaction temperature (43 °C) (Figures 3.7d-e)
- Addition of Solution 2 to Solution 1 and tin deposition for around 1.5 minutes (Figures 3.7f-g)
- Repetitive surface washing with deionized water, ethanol and isopropanol and air drying of the substrate (Figure 3.7h)

The deposition resulted in a uniform 1-2 μm-thick tin layer. As the substrate surface was previously sandblasted to enhance its roughness, a bigger accumulation of tin can be noted in the surface valleys (Figure 3.8).

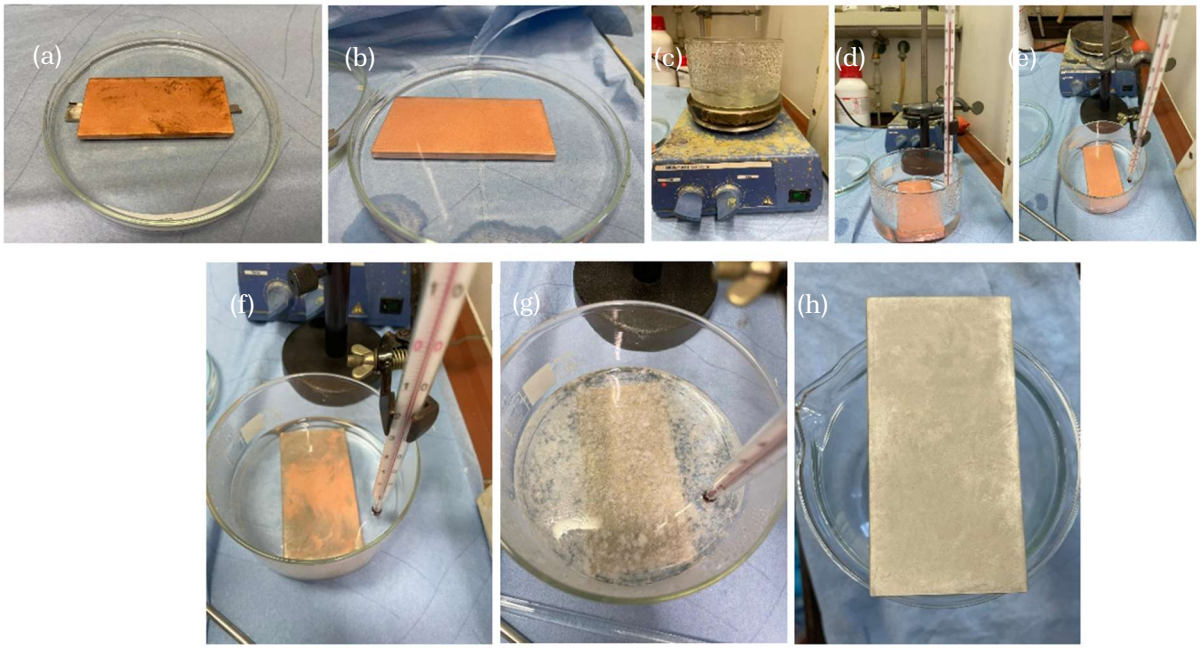


Figure 3.7: Detailed experimental steps for the immersion deposition process of tin onto copper substrate: acetone degreasing (a), surface deoxidization (b), deionized water boiling and thiourea dissolution (c), immersion of copper substrate in Solution 1 (d), cooling to reaction temperature (e), deposition process (f-g), tin coated copper substrate (h)

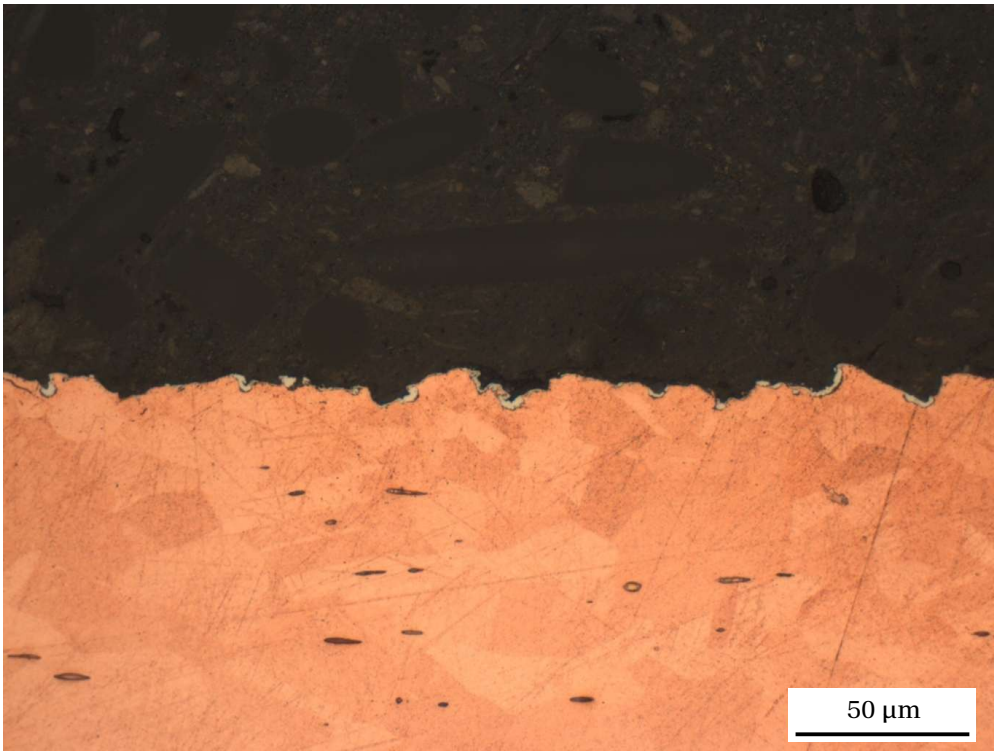


Figure 3.8: Cross-section optical imaging of the tin (green/grey layer in picture) coated copper substrate

3.3 *Powder Feedstock*

The bronze feedstock was 85/15CuSn powder (Sandvik Osprey Ltd., Neath, UK), which composition is reported in Table 3.8.

Table 3.8: Chemical composition of the 85/15CuSn bronze powder

Element	Copper	Phosphorus	Tin
wt.%	84.85	0.10 – 0.35	14 – 16

3.3.1 Powder characterization

The particle size distribution was evaluated with Morphologi 4 static image analysis setup (MOR2800, Malvern Panalytical Ltd., Malvern, UK) and the resulting volumetric and aspect ratio distribution are plotted in Figure 3.9. The calculated cumulative percentile diameters D10, D50 and D90 for the volumetric particle size distribution were: 26, 36 and 49 µm, while the calculated mean aspect ratio was 0.891. Powder morphology is highly spherical, even if some satellites can still be found as is highlighted by the red dotted circles in Figure 3.10.

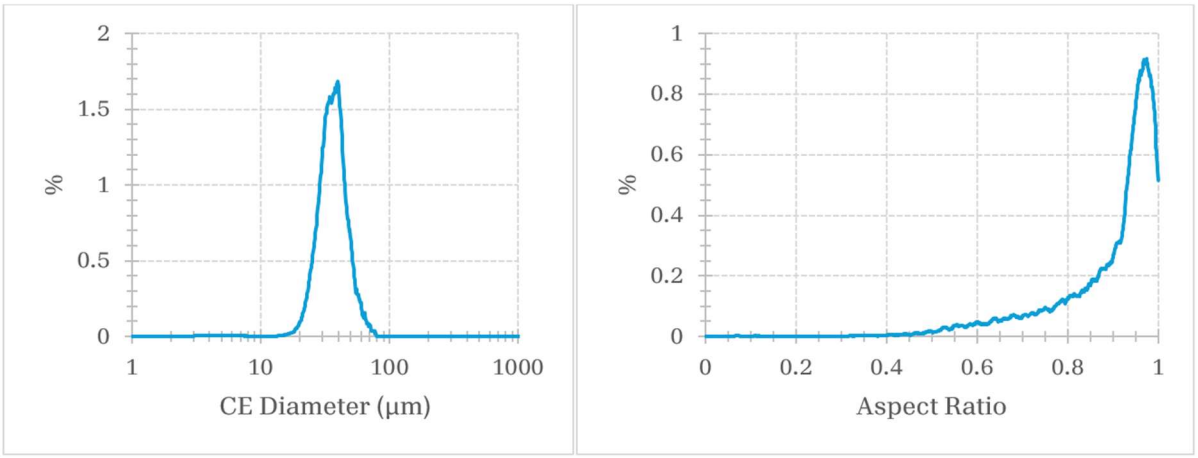


Figure 3.9: Particle volumetric size (left) and aspect ratio distribution (right) for the 85/15CuSn powder

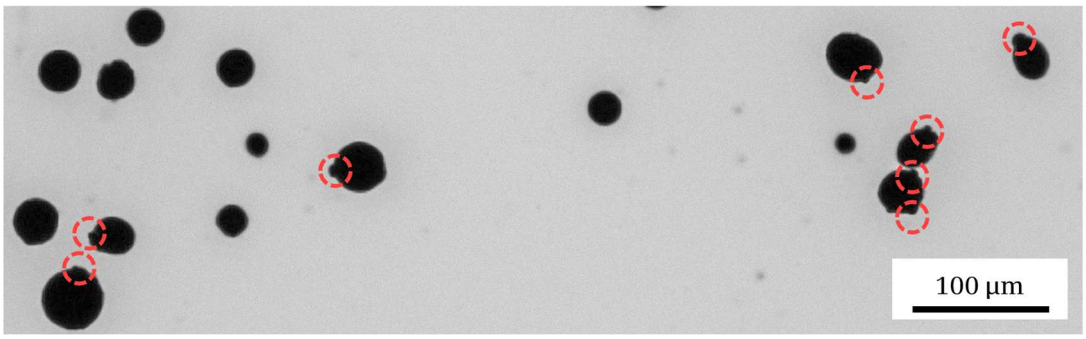


Figure 3.10: 85/15CuSn powder morphology from Morphologi 4 optical imaging; the red dotted circles highlight the satellites

The flowability of the powder was investigated with a GranuDrum setup (Granutools SRL, Awans, Belgium), which consists of a rotating drum equipped with a CCD camera which can calculate the dynamic angle of repose (α_d, the angle formed between the ground plane and the surface of the flowing powder) and the cohesive index (CI, the fluctuation of the interface comparing to the average surface position) of the powder through software image elaboration. The rotating speed of the drum was varied to evaluate potential properties hysteresis, following the scheme: 2, 4, 6, 8, 10, 10, 8, 6, 4, 2 rpm; at each speed, 20 snapshots per seconds of the powder bed were recorded (Figure 3.11) and the two above-mentioned parameters were calculated (acquired data is reported in Table 3.9). It is generally accepted that a small dynamic angle of repose (≤ 35°) and a CI close to zero correspond to good powder flowability [72].

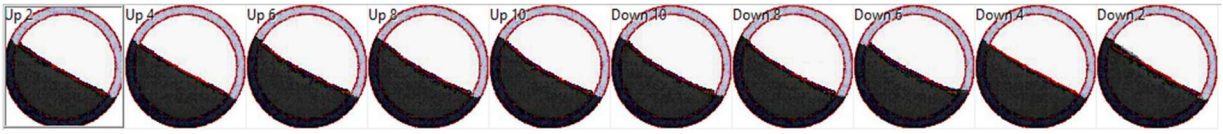


Figure 3.11: Snapshots of the flowing powder bed taken at different drum rotating speed

Table 3.9: Calculated values of dynamic angle of repose (α_d), cohesive index (CI), and their respective hysteresis at different drum rotating speed

	Sequence Velocity		**Reverse Velocity**		**Hysteresis**	
Rotating speed (rpm)	α_d (°)	CI	α_d (°)	CI	α_d (°)	CI
2	31.0	4.1	30.3	3.6	0.7	0.5
4	30.3	3.0	31.6	2.0	1.2	1.0
6	33.4	3.6	31.9	4.3	1.5	0.7
8	32.8	3.4	32.4	3.6	0.3	0.2
10	35.1	3.9	34.4	4.2	0.7	0.2

Although the particle size distribution is within the lower limit of the standard range for DED [73], the flowability was proved to be excellent without any hysteresis behavior which could alter the flowing after some experiments. The collected data verifies the suitability of the chosen powder to the DED process.

3.4 Directed Energy Deposition System

The experiments were performed on a 5-axis BeAM Mobile 1.0 LB-DED machine (BeAM Machines by AddUp, Cébazet, France). Partitioning the degrees of freedom, three are assigned to the nozzle head and two to the substrate platform, as is highlighted by the red arrows indicating the reference axes in Figure 3.12. The maximum nozzle speed is 30,000 mm/min and the build volume is 400×250×250 mm^3, which is

reduced to 200×250×250 mm^3 when all of 5 axes are used. Argon can be used to inert the chamber. In some experimental conditions, the oxygen level in the chamber was decreased down to 500 ppm.



Figure 3.12: BeAM Mobile 1.0 LB-DED machine working chamber and reference axes

3.4.1 Laser Beam Specifications

The nozzle head is equipped with a continuous-wave Yb-fiber laser (YLR-Series, IPG Photonics, Oxford, MA, USA) with an operating wavelength of 1068 nm. Although the system features a nominal power of 500 W, the actual delivered output at 100 % setpoint is 440 W. The laser beam has a Gaussian profile, a spot size at focus of 0.8 mm, and a Rayleigh length of 18 mm.

3.4.2 Nozzle Head

The nozzle head consists of three coaxial copper hollow cones, which create one central and two annular channels. A dedicated water-cooling system is connected to the cones to prevent overheating. The laser beam is delivered through the central channel along with the primary shielding gas. The shaping gas travels through the intermediate channel and the powder is ejected from the outer channel, carried by shielding (or carrier) gas (Figure 3.13). The adjustment between the primary, shaping and carrier powder flow rates modify the shape of the powder jet; a correct and uniform deposition is often obtained when the convergence point of the ejected powder cone is at the laser focus. However, in some cases when high power is needed to melt the substrate, it is convenient to have a slightly off-focused setup (convergence point below the substrate surface) to avoid particle shadowing [24].

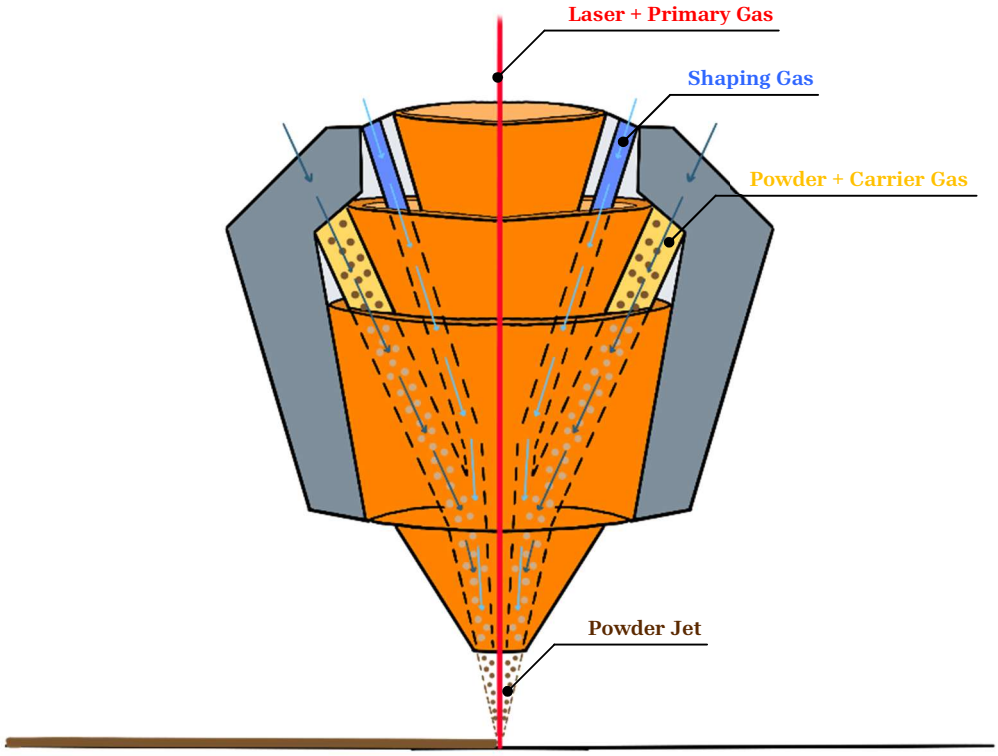


Figure 3.13: Sketch of the coaxial BeAM Mobile 1.0 LB-DED nozzle head

3.4.3 Powder Feeding System

The machine is equipped with two volumetric powder feeders (Medicoat AG, Switzerland), but since no multi-material deposition was performed, only one bowl was used. The powder is first agitated onto a turnplate and then conveyed through the carrier gas stream, after being redirected by a fixed baffle. The powder feed rate of the bronze powder was measured as a function of the plate rotation speed (PRS) at a fixed carrier gas flow of 3 l/min, and it is plotted in Figure 3.14. The primary and the shaping gas flow rates were fixed at 6 l/min, as this value was kept constant in all experiments carried out.

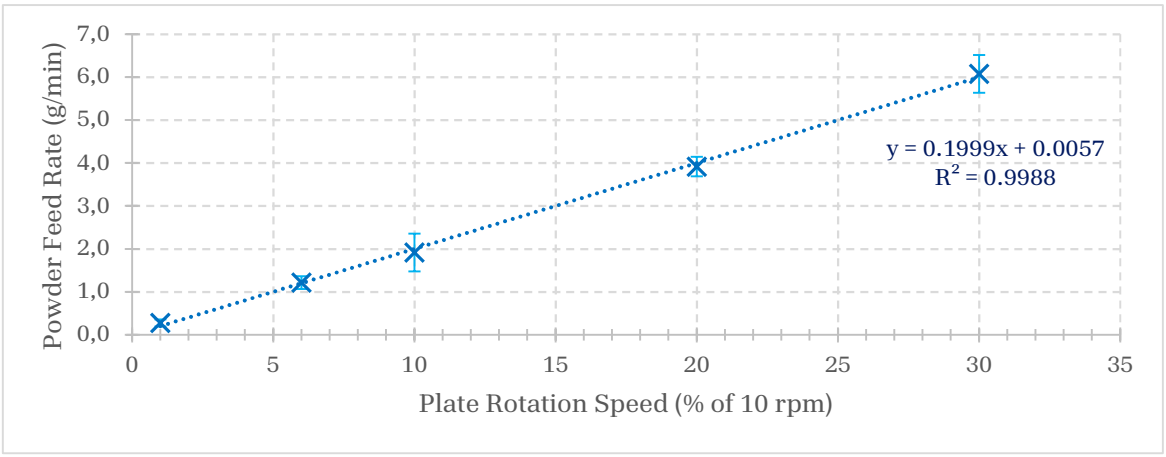


Figure 3.14: Powder feed rate as a function of plate rotation speed for the 85/15CuSn powder at fixed primary, shaping and carrier gas flow rates

3.4.4 Powder Jet Convergence Height Characterization

Adjusting the primary and secondary gas flow rates, as well as the powder feed rate, the powder jet modifies its shape and the convergence height changes. The convergence height has been calculated following these steps: image acquisition of the powder jet (live acquisition from a digital camera connected to a laptop with ThorCam (Thorlabs, Inc., Newton, NJ, USA) software), image processing and measurements with Fiji (ImageJ) software. The effective value was evaluated as the distance from the nozzle where the powder stream has a width of the laser spot size at focus (0.8 mm). This parameter is key to understanding how much of the laser power is lost to either melt the particles in-flight or to heat/melt the substrate or the previous deposited layer. Once the correlation between the convergence height of the powder jet and the powder feed rate is known, different strategies can be implemented in actual depositions:

- Working distance (WD) shorter than the convergence height concentrates the heat on the substrate/last deposited layer;
- Working distance bigger than the convergence height leads to in-flight melting of the particles (similarly to cladding) and shadowing of the substrate.

The powder jet convergence height for the 85/15CuSn bronze powder was evaluated at different powder feed rates (function of the turnplate rotation speed, as described in Chapter 3.4.3) at a fixed gas flow rate of 6 l/min for both the primary and the shaping gas and 3 l/min for the carrier gas (Figure 3.15a). A schematic representation of the measurement method and an example processed image are reported in Figure 3.15b and Figure 3.15c.

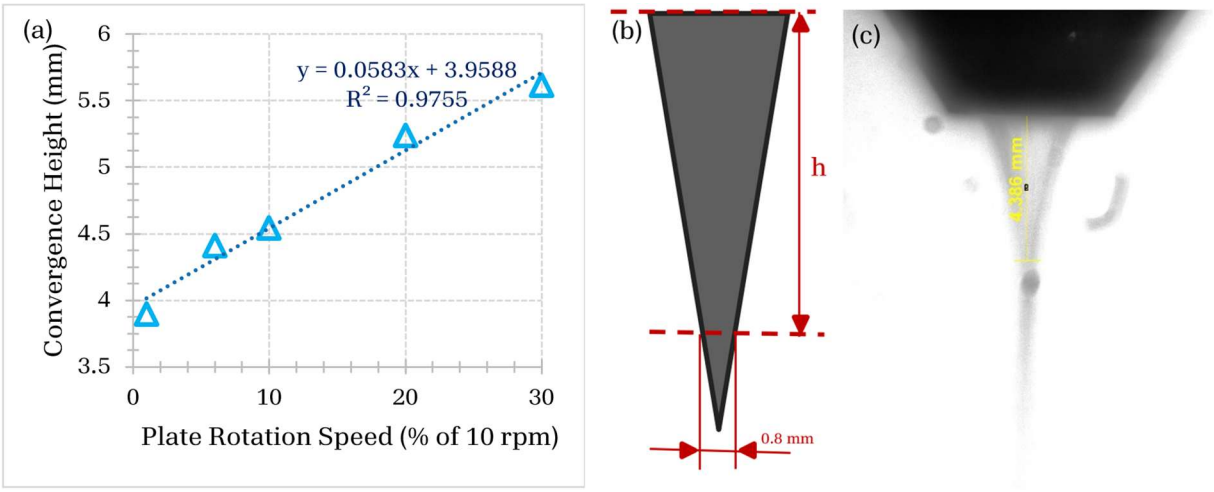


Figure 3.15: Powder jet convergence height as a function of plate rotation speed at fixed primary, shaping and carrier gas flow rates (a), schematic illustration of the measurement method (b), processed image at 6 % of plate rotation speed (c)

The convergence height of the powder jet increased linearly with the powder feed rates/ feeder plate rotation speed ($y = 0.0583x + 3.9588$, $R^2 = 0.9755$), extending the powder focal plane downwards at higher feed rates.

3.5 *High-speed Visible Imaging – Thermal Distortion Analysis*

High-speed imaging was performed focusing on the substrate while the laser scanning/deposition of the 85/15CuSn powder was carried out on the tin coated plate. The imaging setup consisted of a high-speed camera (Videal Motion Pro Y4, Videal AG, Niederönz, Switzerland) equipped with a telecentric lens and a shortpass filter FESH0950 (Thorlabs, Inc., Newton, NJ, USA), which has 950 nm cutoff wavelength to protect the optical lenses when the laser beam is on. The setup included an LED matrix illuminator, which was positioned opposite the camera with respect to the substrate to capture in backlight mode or between the camera and the substrate to capture in front-light mode. 270 frames per second were captured at a pixel depth of 8-bit, and the total resolution was set to 1024×1024 pixels. The relatively low frame rate employed allowed the acquisition of the complete process without large data management. During laser scanning at 95 % of maximum output power of the beam at different speeds, high-speed imaging was utilized to observe whether any signs of melt pool were visible, while the videos acquired during the powder deposition process helped to understand how thermal distortion happens. A schematic sketch of the high-speed imaging setup in backlight mode is reported in Figure 3.16.

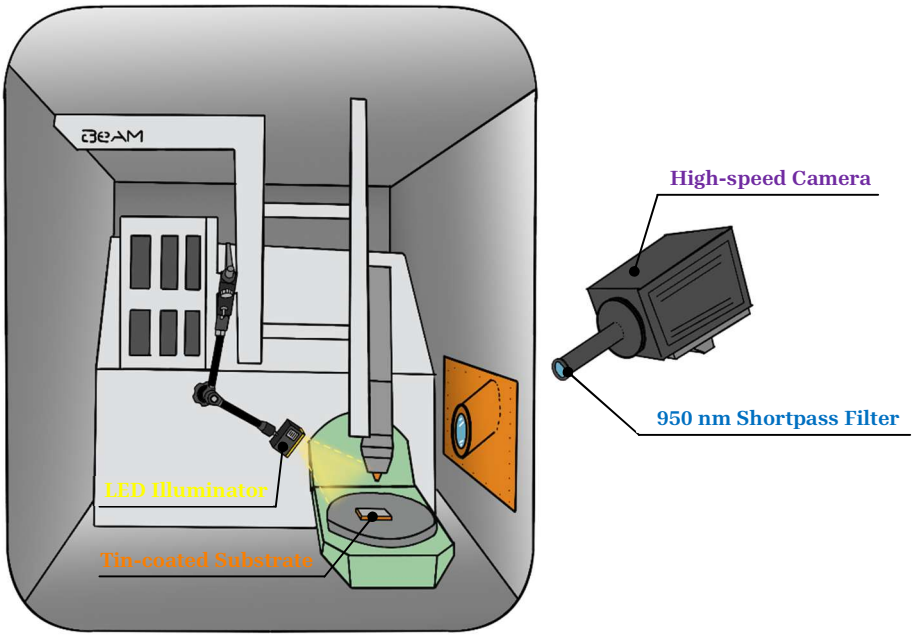


Figure 3.16: Schematic sketch of the setup used for the backlight high-speed visible imaging of the LB-DED process

To quantify the localized displacement and thermal distortion of the deposited track, an optical tracking procedure was implemented in Fiji (ImageJ) using the TrackMate plugin (v8.1.6) [74], [75]. Two representative 1024 × 1024-pixel frames acquired via front-light high-speed visible imaging during the LB-DED process were spatially calibrated against the scale bar, yielding an effective resolution of 8,30 µm/pixel. Following threshold-based segmentation was applied to convert the frames into binary masks, isolating the track profile and the substrate from the background.

The two-frame sequence was processed as a temporal stack; features were detected using a Difference of Gaussian (DoG) detector with an estimated feature nominal diameter of 0.50 mm, an intensity threshold of 1.0, and sub-pixel localization enabled without median filtering. The detected spots were linked using the Simple Linear Assignment Problem (LAP) tracker with maximum linking and gap-closing distances fixed to 1.0 mm (maximum frame gap of 2), generating 12 paired tracks. The net displacement magnitude ($|\Delta\mathbf{r}|$) was calculated as:

$$|\Delta\mathbf{r}| = \sqrt{\Delta X^2 + \Delta Y^2} \tag{3.17}$$

where ΔX is the longitudinal displacement and ΔY is the vertical deflection calculated from the initial and final coordinates of each feature (geometrically corrected based on the camera's tilt angle, i.e. 45 °)

3.6 Sample Preparation

For the metallographic characterization, the samples were prepared according to the following routine: cutting, hot mounting, grinding, polishing, and metallographic etching (Figure 3.17).



Figure 3.17: Adopted sample preparation routine

The cutting was performed along the transversal direction (with respect to the deposition direction) with a 30A13 Al_2O_3 cut-off wheel using the Accutom-10 (Struers, Ballerup, Denmark) machine. Subsequently, the cut samples were hot-mounted with a conductive carbon-filled bakelite resin (PolyFast, Struers) utilizing the Hydropress A (Jean Wirtz, Düsseldorf, Germany). The grinding included different steps at different grit sizes, in order: 320, 600, 1200, 2500, 4000 SiC papers were used on a PlanoPol (Struers) machine for around 1-2 minutes each. The ground samples were later polished using 6, 3, and 1 µm diamond suspensions (DP-Suspension M, Struers) at 150 rpm and 90 lbs of normal force for 4 minutes for each step on a Phoenix 4000 system (Buehler Ltd., Lake Bluff, IL, USA). The final step to achieve mirror-like surface finishing included polishing with OP-U 0.04 µm colloidal silica suspension for 15 minutes at 100 rpm and 80 lbs of normal force. The samples were then rinsed with deionized water and ethanol and air-dried with compressed air followed by a hot air stream.

When microstructure characterization was needed, metallographic etching was performed. Different strategies were tried (Figure 3.18), but the best highlighting of grain boundaries was obtained after submerging the samples for 10 seconds in Klemm II solution, consisting of 1:20 dissolution of potassium disulfite ($K_2S_2O_5$, ≥98 %, SAFC) in a saturated sodium thiosulfate pentahydrate solution ("Klemm stock

solution", $Na_2S_2O_3 * 5H_2O$, Sigma-Aldrich). The adopted method was suitable for both the pure copper substrate and the 85/15CuSn powder deposition.

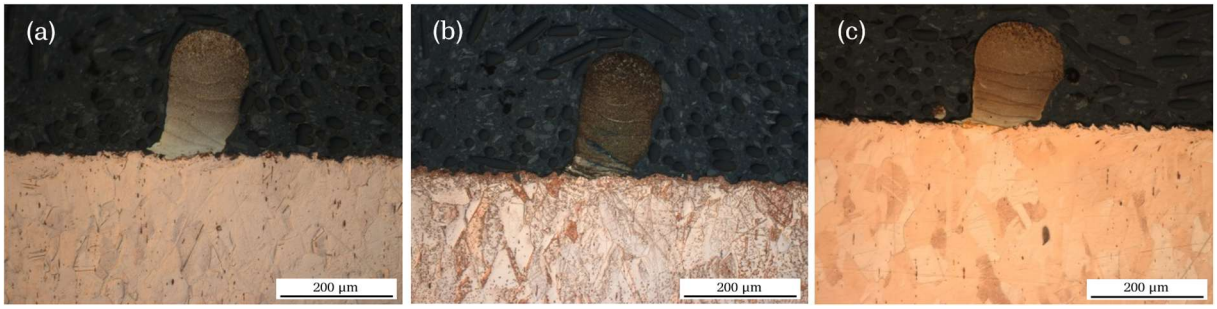


Figure 3.18: Cross-sectional optical micrographs of etched samples of bronze deposition on copper substrate using different etching solutions: (a) 1:10 solution of ammonium persulfate ($(NH_4)_2S_2O_8$) in deionized water, (b) 1:40 solution of ferric chloride ($FeCl_3$) in a 1:20 hydrochloric acid (HCl, 37%) ethanol solution, and (c) the selected Klemm II solution.

3.7 Optical Imaging

Optical micrographs were obtained with a ZEISS Axioplan upright optical microscope (ZEISS, Munich, Germany). The maximum available magnification is 100x, and it can be performed only via oil immersion. Employing polarized light enables the visualization and highlighting of the grains of the material etched with Klemm II solution.

4 Results and Discussion

In this chapter the results of the attempted LB-DED depositions of the 85/15CuSn bronze powder onto the surface-modified pure copper substrates are reported, including optical micrographs, high-speed visible imaging, and simulation work. The results from the latter are also compared with experimentally acquired thermal data.

4.1 Untreated and Sandblasted Copper Substrate

The current chapter includes the numerical simulations of the LB-DED process onto both untreated and sandblasted pure copper substrate. For the latter, attempted laboratory experiments and an investigation on minimal requirements to initiate surface melting employing a near-infrared laser source are also reported.

4.1.1 Numerical Simulation of Laser-Material Interaction on Copper

Preliminary tests were performed to investigate the interaction between the laser beam and the untreated/sandblasted copper substrate. The simulation was performed to investigate the thermal field evolution in the substrate during the laser passage when no powder is injected to evaluate whether the installed laser heat source is sufficient to sustain a melt pool in the substrate, employing maximum power output and reasonable scanning speed for the LB-DED process.

The simulated model consisted of a 15×30×8 mm^3 body associated to the pure copper substrate. Thanks to the intrinsic symmetry of the process, the total 3D model was cut along the laser direction and only half of the geometry was simulated. The test consisted of a 5-second simulation of a 10-millimeter laser scan in the central region of the top surface. The simulated process parameters are listed in Table 4.1. Given its speed, the laser scanned the substrate for around 1 second, while the last 4 seconds simulated the cooling stage. The resulting energy density value was 55 J/mm^2.

Table 4.1: Simulated process parameters for the laser scan experiment carried out on COMSOL Multiphysics software; T_0 is the initial substrate temperature and E is the resulting energy density of the beam

Type	P_{laser} (W)	v (mm/min)	T_0 (K)	E (J/mm^2)
Laser Scan	440	600	300	55

In order to achieve an efficient trade-off between computational data and numerical accuracy, a multi-scale mapped mesh was implemented in the finite element (FE) model (Figure 4.1). The 3D domain was discretized into different sub-domains and

locally refined in correspondence of the heat-affected zone (HAZ). Indeed, this region is involved by the laser passage, and, consequently, steep transient thermal gradients, localized phase transformations, and extreme cooling rates typical of the DED process must be resolved accurately. Therefore, the refinement in the HAZ was obtained by imposing a maximum element size of 5×10^{-5} m to the already 2D "Free-Quad" meshed top surface. The surface mesh was then "swept" in the Z-negative direction using a distribution node to refine the elements close to the upper face. A detailed view of the resulting 3D mesh and the HAZ refined region are reported respectively in Figure 4.1a and Figure 4.1b.

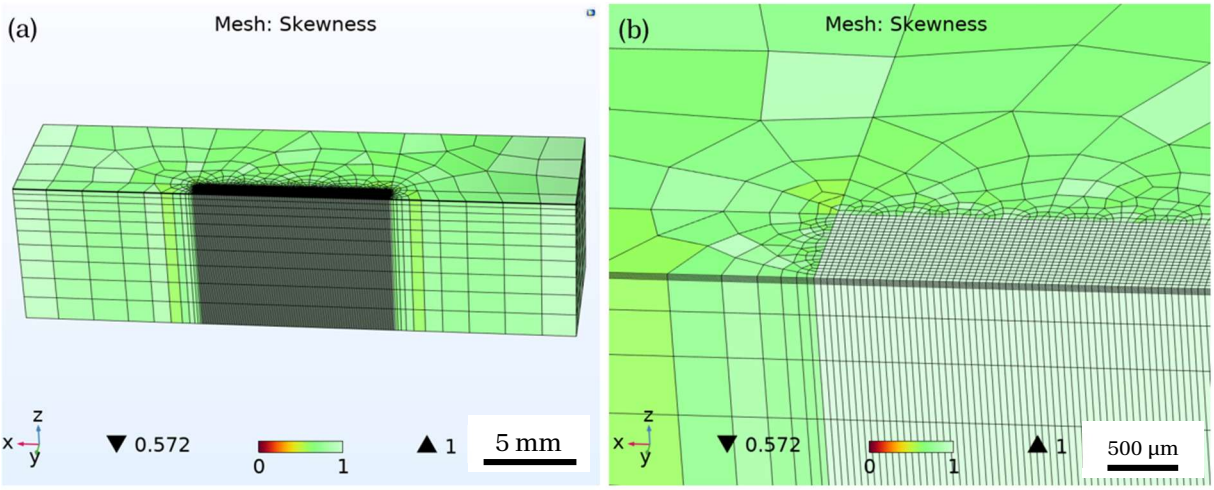


Figure 4.1: (a) Mesh quality plot for the simulated model; (b) magnification of the refined submesh for the heat-affected zone (HAZ) modeling

The resulting mesh consisted of 76,425 elements, of which 75,285 hexahedral and 1,140 prismatic, with an average element quality of 0.9551.

A parametric study was performed using the numerical model to evaluate the evolution of the substrate temperature field during laser scanning under the two different surface conditions. The surface absorptivity at laser wavelength of the pure copper substrate was changed in the two studied cases (reference values can be found in Appendix A). A representative snapshot of the process acquired at the end of the laser track, right before its extinguishing (at t = 0.9992 s) is reported in Figure 4.2, both for the untreated (Figure 4.2a) and the sandblasted surface scenario (Figure 4.2b). Regarding the untreated scenario, the substrate reached a maximum temperature of 380 K under a laser irradiation with an energy density of 55 J/mm^2. As for the sandblasted scenario, the peak temperature was 479 K. Despite the surface roughening increased the coupling with the beam, these temperature values were only 80 – 179 K higher than the substrate initial temperature (i.e. 300 K), meaning that the interaction with the laser beam was nearly null.

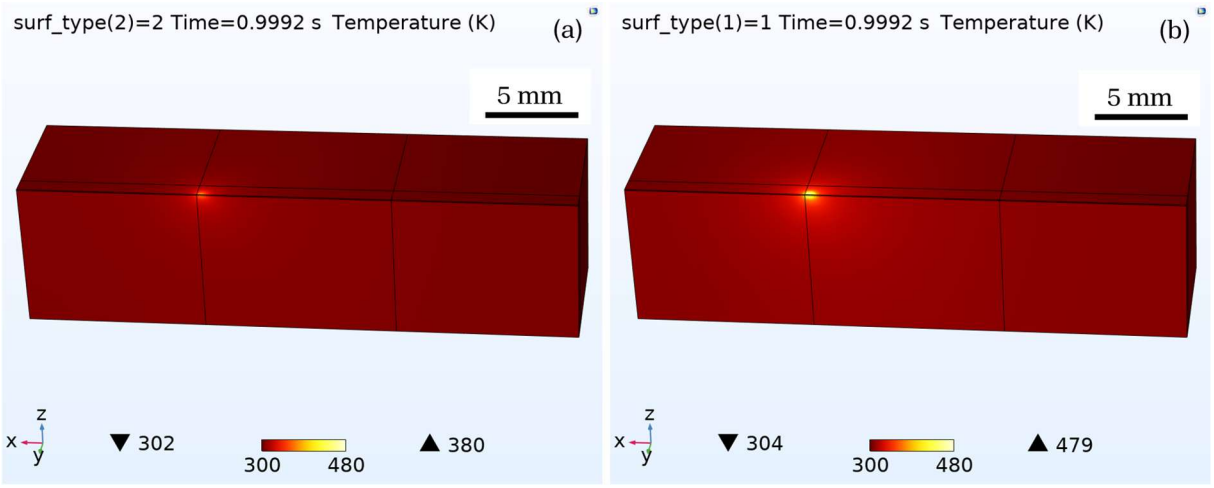


Figure 4.2: Temperature field at the end of the laser track for: (a) untreated copper substrate, (b) sandblasted copper substrate

From the preliminary tests carried out on COMSOL Multiphysics software it was possible to state that an energy density of 55 J/mm^2 was not sufficient to melt a pure copper substrate employing a near-infrared laser source. The surface sandblasting enhanced laser absorptivity by around +26 %; however, the maximum recorded temperature along the track was still around 880 K lower than copper melting temperature. The simulation verified the need for surface modification of the substrate and/or higher energy densities to enhance the interaction with the laser source.

4.1.2 LB-DED of Single Tracks onto Surface Sandblasted Copper Substrate

Single tracks of 85/15CuSn bronze of a length of 10 mm were deposited onto a sandblasted pure copper substrate. Preliminary tests were performed to investigate the process parameters to obtain homogeneous and well-adhered 2D structures.

For the deposition of single tracks, the process parameters were varied between the intervals listed in Table 4.2. The output power (P_{laser}) was kept close to the system limit (90-95 % of the nominal power), the scanning speed varied from low to very high, the turnplate rotation speed (PRS) provided different powder feed rates (from around 1.0 to above 6.0 g/min, cf. Chapter 3.4.3) at a fixed primary, shaping, and carrier (P×S×C) gas flow rates, the different working distances reflected the different deposition strategies (laser focused on the substrate at WD lower than the powder jet convergence height, in-flight particle melting and substrate shadowing at bigger WD, and transitional behavior at intermediate WD), and the substrate was kept at either room temperature (RT) or pre-heated by a heating plate. Indeed, substrate preheating is a widely accepted DED thermal-management technique to enhance bonding conditions and clad dimensional accuracy [76], [77].

Table 4.2: Tested process parameters values for the optimization of the deposition of single tracks for the LB-DED process of 85/15CuSn onto roughened pure copper substrates

Process Parameter	P_{laser}	v	**PRS**	**WD**	**P×S×C Gas Flow Rates**	**Temperature**
Unit of measurement	W	mm/min	% of 10 rpm	mm	l/min	°C
Tested Values	450, 475	100, 200, 300, 450, 600, 750, 900, 1050	6, 10, 15, 20, 30	3.5, 5, 7	6×6×3	RT, 300

A limitation of the LB-DED machine utilized was the effective laser power output registered during the process. Setting 95 % of nominal power in the process code (i.e. 475 W out of the maximum 500 W capacity) would result only in an average of 440 W output power, 8 % lower than expected. Therefore, the resulting Laser Energy per unit Powder Feed (LEPF) index varied between 4,140 and 26,400 J/g and the energy densities tested were in the range 30 – 330 J/mm^2. However, in all the tried combinations of the parameters reported in Table 4.2 no effective adhesion of the tracks was observed and, even if the powder was effectively melted by the laser, the deposited beads detached easily from the substrate (Figure 4.3).



Figure 4.3: Example of a deposited 85/15CuSn single track onto roughened pure copper substrate; imprints of already detached beads can be seen in the back

When preheating the substrate in air was performed, the copper surface oxidized quickly and turned black/dark (Figure 4.4). The oxide layer further compromised the

deposition of the bronze powder, and, again, no real adhesion of the beads was obtained (the beads were easily detached after cooling/weak pulling with fingers).

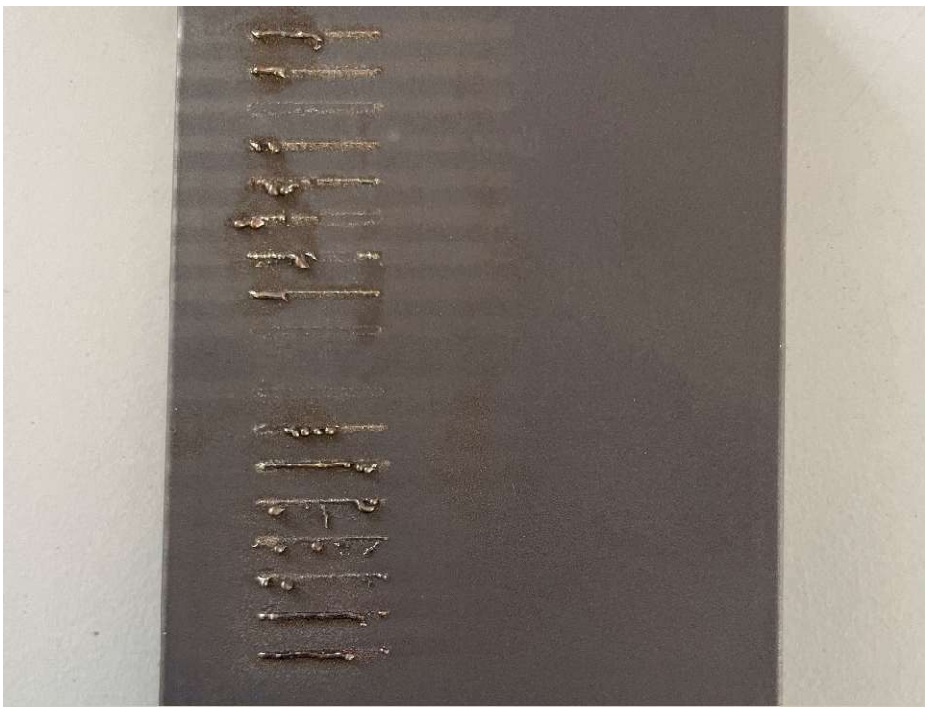


Figure 4.4: Single tracks deposited onto pre-heated roughened pure copper substrate at 300 °C. The dark surface of the substrate is due to the presence of the oxide layer

A closer look to the imprints left from the detached beads showed that the copper surface was not modified at all even when the highest laser output power was applied at the lowest scanning speed and at a close working distance to avoid particle shadowing. Indeed, this combination of parameters leads to the highest possible energy density on the substrate but, still, no traces of copper melting were observed. Since no melt pool could be created on the first layer, no metallurgical bond between the bronze and the copper was generated and, therefore, the detachment occurred. Moreover, increasing the energy density of the beam led to increased thermal distortion of the bronze beads, and the accumulation of molten powder resulted in the creation of big bronze balls that were eventually splashed away by the nozzle gases.

Although a higher energy density was required to melt the copper substrate (as predicted by numerical simulations), operating at low scanning speeds resulted in deposition failures due to hardware limits of the powder feeder. To prevent powder accumulation, the powder feed rate had to be reduced proportionally; however, when the turnplate rotation speed was set to lower than 6 % (of 10 rpm) the continuous powder stream was replaced by a pulsating flow, inevitably leading to defective and irregular tracks.

The combination of high scanning speed and large working distance was tested to deposit bronze powder via in-flight melting. However, despite the effective powder melting at lower energy density, substrate adhesion was completely absent, leading to unsuccessful track formation.

4.1.3 Numerical Simulation of Sandblasted Copper Substrate Melting Thresholds

An investigation about the minimum near-infrared laser output power requirements has been carried out. A parametric study was carried out simulating a 10 mm laser scan on a sandblasted copper substrate at increasing laser output power. After the first screening, no large substrate heating was observed below 2 kW of laser output power. Therefore, 2,500 and 2,800 W were chosen as parametric inputs. The geometry of the model was the same as reported in Chapter 4.1.1, but the laser scanning speed was lowered to 100 mm/min. The resulting energy density values for each case were: 1,875 and 2,100 J/mm^2. Given its speed, the laser scanned the substrate for around 6 seconds, and 4 additional seconds were added to simulate the cooling stage.

For the 2,500 W scenario, the highest recorded temperature on the substrate top surface was 1,090 K, around 270 K lower than copper melting temperature. Conversely, a melt pool was effectively formed in the 2,800 W output power scenario beginning around the middle of the laser trajectory. To better visualize where the eventual melting was taking place, a binary phase map was plotted over time: given the condition "$T \geq$ copper melting temperature" (i.e. 1,357.77 K), the green zones highlight the volumes where the condition is met while red highlights the solid domain (Figure 4.5a). The biggest dimensions of the melt pool were recorded at the end of the laser scan, meaning that sufficient heat accumulation is needed to sustain the melt pool even at higher energy densities. The dimensions of the liquid region were investigated right before the laser extinguishing (at t = 5.995 s) by cutting the 3D domain athwart the laser direction (Figure 4.5b).

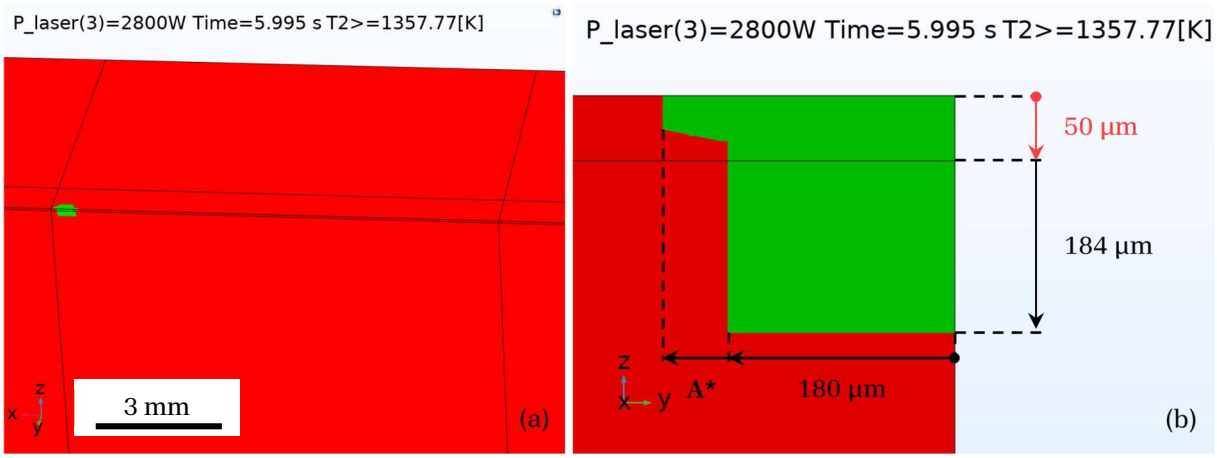


Figure 4.5: (a) Cu-binary phase map at the end of the laser track for the 2,800 W scenario (green highlights the liquid phase volume, while red is the solid volume); (b) cross-sectional view of the melt pool at t = 5.995 s, with related measurements to the known depth of the submesh (highlighted in red, A* = 225 µm)

Regarding the 2,800 W case, the melt pool reached a maximum depth of 184 µm with a width of 360 µm with respect to the laser axis. The maximum width on surface was 450 µm. Considering that the melt pool width was still approximately half of the laser spot diameter, process stability at 2,100 J/mm^2 remains uncertain. However, it

is the minimum numerically assessed threshold to initiate surface melting on a sandblasted pure copper substrate with a near-infrared laser source.

4.2 Surface-modified Copper Substrate

This chapter provides the results of the simulations and attempted LB-DED experiments of 85/15CuSn powder onto surface-modified pure copper substrates. Specifically, three surface engineering strategies are investigated: the application of a titanium starting foil, carbon spray coating, and tin coating by immersion deposition.

4.2.1 Titanium Starting Foil

A thin titanium sheet (thickness = 0.5 mm) was clamped onto a sandblasted pure copper substrate. The initial laser position was above the titanium slab and 10 mm-long laser scans/single tracks/walls (superposition of tracks along the same direction at increasing Z coordinate) were performed along the X-direction of the machine. For this case, no preliminary numerical simulations were performed as the localized starter is used exclusively to facilitate melt pool ignition at the track onset, while the predominant part of the process progresses over the sandblasted copper surface, which was already previously modeled.

The experiments were carried out at room temperature and at a constant P×S×C gas flow of 6×6×3 l/min. The parameters being tested have been listed in Table 4.3. For multi-layer wall depositions, processing parameters were dynamically adjusted between the first and subsequent layers to account for the evolving substrate conditions. As the first layer of bronze was deposited, the following layer parameters were adapted to compensate for the increase of laser absorptivity and the decrease of thermal conductivity, resulting in a decreasing energy density strategy.

Table 4.3: Overview of the thin titanium sheet experiments carried out. As for the case of the 2-layer wall, the notation "x + y" stands for the different parameters used for the first (x) and the second (y) layer

Test	Type	P_{laser} (W)	v (mm/min)	PRS (% of 10 rpm)	WD (mm)
a	Laser Scan	440	5	-no powder-	7
b	Laser Scan	440	50	-no powder-	7
c	Laser Scan	440	300	-no powder-	7
d	Single Track	440	5	1	5
e	Single Track	440	10	1	5
f	2-layer Wall	440	10 + 300	1 + 10	5

An image captured at the end of the experiments carried out is reported in Figure 4.6. For every test, the titanium slab clearly and evidently melted, as big holes can be

seen at the beginning of the tracks. Regarding the laser scans (Figure 4.6a-c), slightly brighter imprints can be seen after the laser passage, but no real difference with respect to previous experiments is observed, and no melting of the copper substrate has been reached either at very slow scanning speed (e.g. test "a" at 5 mm/min). However, the surface is completely unaltered at higher scanning speed (test "c"). As for the single tracks (Figure 4.6d-e), the deposition at very low scanning speed was interrupted as big accumulation of molten powder occurred at the beginning of the track. As it might seem that some deposition effectively occurred for test "e", no adhesion with the substrate was obtained as the only metallurgical bond created was the one with the titanium sheet. The 2-layer wall (Figure 4.6f) completely detached after the deposition of the second layer, as it was probable that the thermal stress exceeded the little interfacial strength with the substrate.

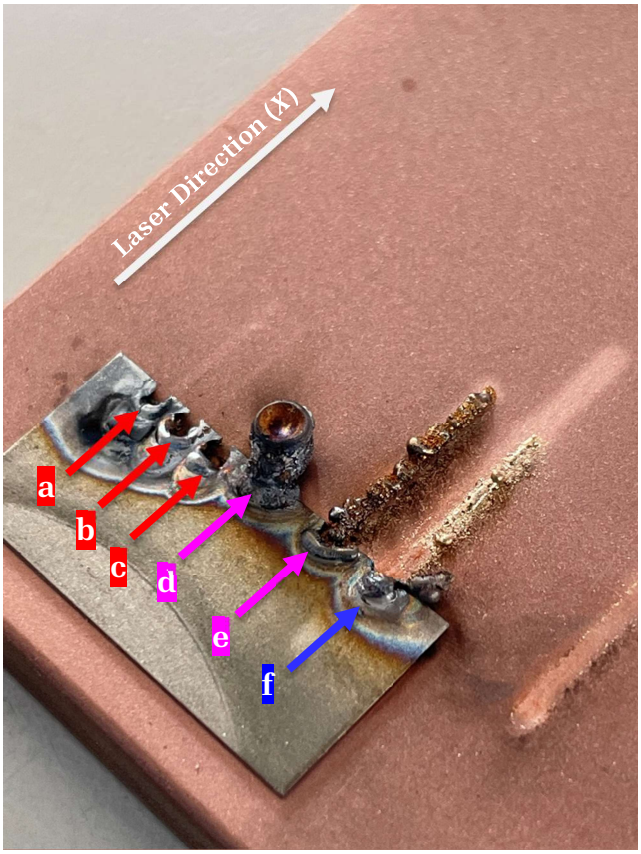


Figure 4.6: Thin titanium sheet LB-DED experiments. The letters correspond to the test labels reported in Table 4.3. The different colors highlight the different types of experiment: red for laser scans without powder, pink for single tracks, and blue for walls

4.2.2 Carbon Spray Coated Copper Substrate

A laser scan and several 85/15CuSn single-track experiments were carried out onto a carbon spray coated pure copper substrate. The substrate temperature and the primary, shaping, and carrier gas flow rates were set constant to room temperature and 6 × 6 × 3 l/min respectively. The parameters being tested are reported in Table 4.4.

Table 4.4: Overview of the carbon spray coated copper substrate experiments carried out

# Test	Type	P_{laser} (W)	v (mm/min)	PRS (% of 10 rpm)	WD (mm)
1	Laser Scan	440	100	-no powder-	3.5
2-9	Single Track	440	100, 300	6, 10	3.5, 5
10	Single Track	440	20	1	3.5

As soon as the laser interacted with the carbon spray coated substrate, the residual organic binder pyrolyzed and evaporated bringing some carbon particles away from the laser focus zone (the large carbon powder shadow shown for test 1 in Figure 4.7). When the powder is injected during the actual LB-DED process this phenomenon is attenuated and the reason could be the sticking of the carbon particles to the deposited molten bronze powder. However, no adhesion was again observed and all the deposited beads detached right after the process.

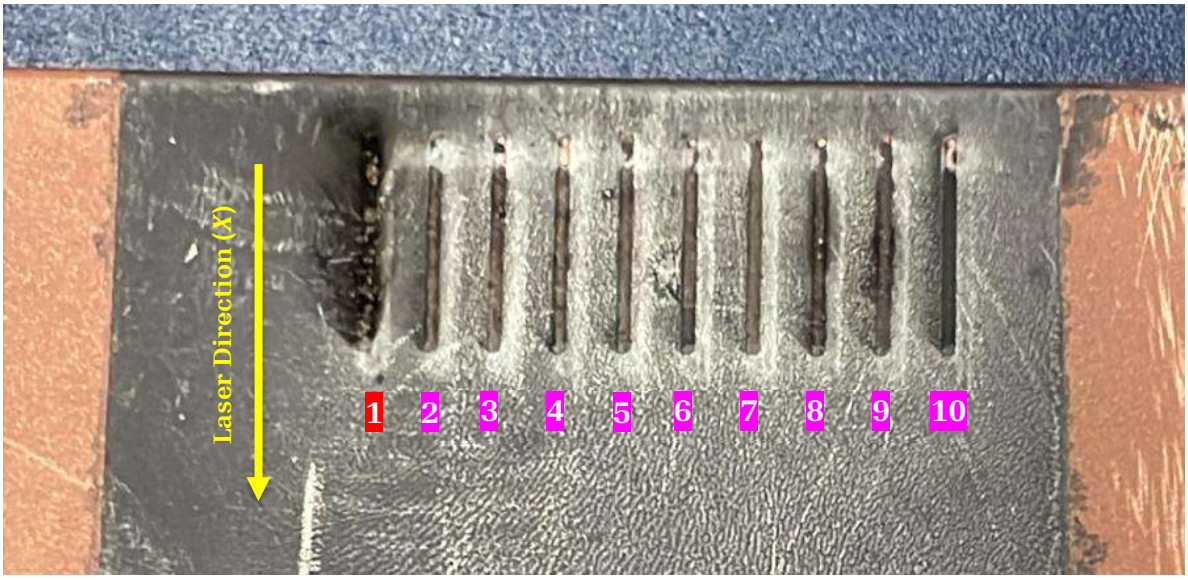


Figure 4.7: Carbon spray coated copper substrate experiments: laser scan (1, red) and 85/15CuSn single tracks (2-10, pink)

4.2.3 Immersion Deposited Tin Coating

A thin metallic tin layer was deposited onto the pure copper substrate by immersion deposition. Given the higher absorptivity of tin at the operating wavelength, better interaction with the laser was expected. A comparison between simulation results of the laser-material interaction carried out with COMSOL Multiphysics software and actual LB-DED experiments is reported in the current chapter. After validation of the simulation model with high-speed thermography, a minimal laser requirements investigation is performed to find out the minimum value of energy density needed to theoretically melt the tin coated pure copper substrate employing a near infrared laser source.

4.2.3.1 Numerical Simulation of Laser-Material Interaction on Tin-Coated Copper

Preliminary tests were performed using COMSOL Multiphysics software to investigate the interaction between the laser beam and the tin-coated copper substrate. The simulation was performed to investigate the thermal field evolution in the substrate during the laser passage when no powder is injected. The purpose of the experiment was to evaluate whether the installed laser heat source is sufficient to sustain a melt pool in the surface-modified substrate, employing maximum output power and reasonable scanning speed for the LB-DED process.

The simulated model consisted of a 15×30×8 mm^3 body associated to the pure copper substrate and a 15×30 mm^2 and 1 µm-thick body (positioned above the former domain) associated to the tin coating. The test consisted of a 5-second simulation of a 10-millimeter laser scan in the central region of the top surface. The process parameters were 440 W laser power, 600 mm/min scanning speed, and 300 K initial substrate temperature. Thus, the investigated energy density was 55 J/mm^2.

A multiscale mapped mesh was employed to achieve numerical accuracy at manageable computational cost (Figure 4.8a). The 3D sub-mesh of the HAZ was created as the intersection between a 2D "Free Quad" mesh (scale factor of 50 in both *X* and *Y* directions) swept from the upper surface of the substrate to the base surface, and a 2D "Mapped" mesh of a 50 µm-deep region underneath the tin layer swept from the symmetry plane to a cut-plane located 0.5 mm away from the laser path (Figure 4.8b). A distribution node was added to the lateral 2D mapped mesh to concentrate the finest mesh resolution directly at the top of the irradiated surface. The resulting mesh consisted of 194,142 elements, of which 191,178 hexahedral and 2,964 prismatic, with an average element quality of 0.9431.

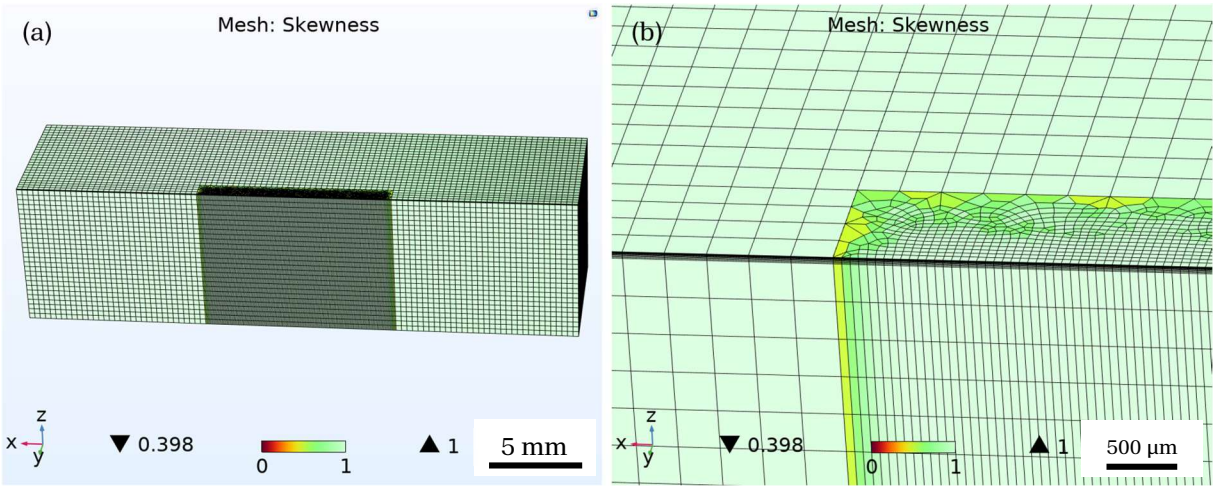


Figure 4.8: (a) Mesh quality plot for the tin coated substrate model; (b) magnification of the refined sub-mesh for the heat-affected zone (HAZ) modeling

The temperature field evolution of the substrate during the laser scanning was evaluated by the software and a representative snapshot of the process acquired at the end of the laser track, right before its extinguishing (at t = 0.9992 s) is reported in Figure 4.9.

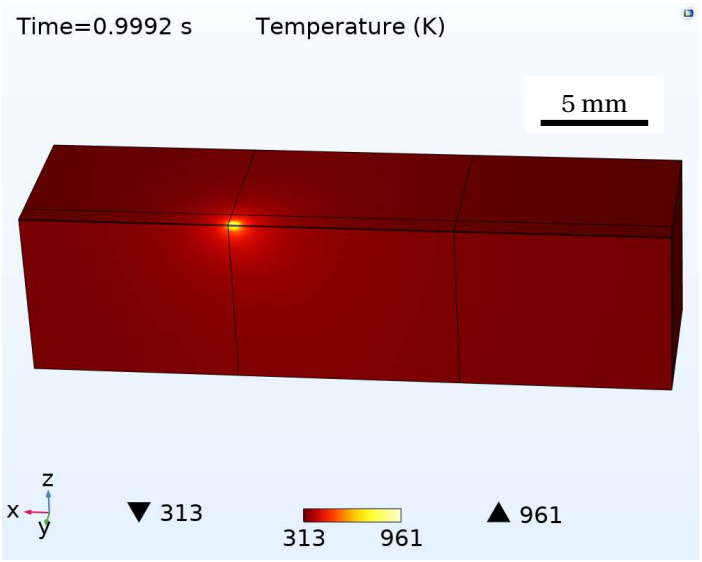


Figure 4.9: Temperature field at the end of the laser track for the tin-coated copper substrate

For a better comparison between the tin-coated surface scenario and the previous sandblasted and untreated scenarios please refer to Appendix B, where the snapshots are reported on the same scale. The substrate reached a maximum temperature of 961 K under laser irradiation with an energy density of 55 J/mm^2. This value was more than 480 K higher than the peak temperature of the sandblasted case, but still around 400 K lower than copper melting temperature. Therefore, even if the interaction with the substrate was notably stronger, no melt pool should form, meaning that an energy density of 55 J/mm^2 is not sufficient to initiate surface melting on a tin-coated pure copper substrate.

4.2.3.2 LB-DED Experiments on Tin-Coated Copper Substrate

Laser scans, single tracks and 4-layer walls were performed onto a tin coated pure copper substrate, obtained by immersion deposition in a solution containing tin (II) chloride. The experiments were carried out at room temperature and at a fixed P×S×C gas flow of 6×6×3 l/min. A detailed overview of the process parameter tested is reported in Table 4.5. Unlike the former experiments carried out, single tracks were effectively obtained with homogeneous beads (Figure 4.10). Nevertheless, as soon as multiple layers were tried to be printed, as in the case of the 4-layer walls, the detachment from the substrate still occurred, even if different strategies were implemented (decreasing LEPF and energy density as the deposition of the upper layers is made onto bronze, which better interacts with the laser).

Table 4.5: Overview of the LB-DED experiments carried out onto the tin coated copper substrate. As for the case of the 4-layer walls, the notation "x + y" stands for the different parameters used for the first (x) and the three upper (y) layers

# Test	Type	P_{laser} (W)	v (mm/min)	PRS (% of 10 rpm)	WD (mm)
1-2	Laser Scan	440	20, 100	-no powder-	3.5

3-8	Single Track	440	100, 300	6, 8, 10	3.5
9-12	4-layer Wall	440	100 + (100, 300, 600, 1000)	8	3.5
13	4-layer Wall	440 + 415	100 + 1000	8	3.5

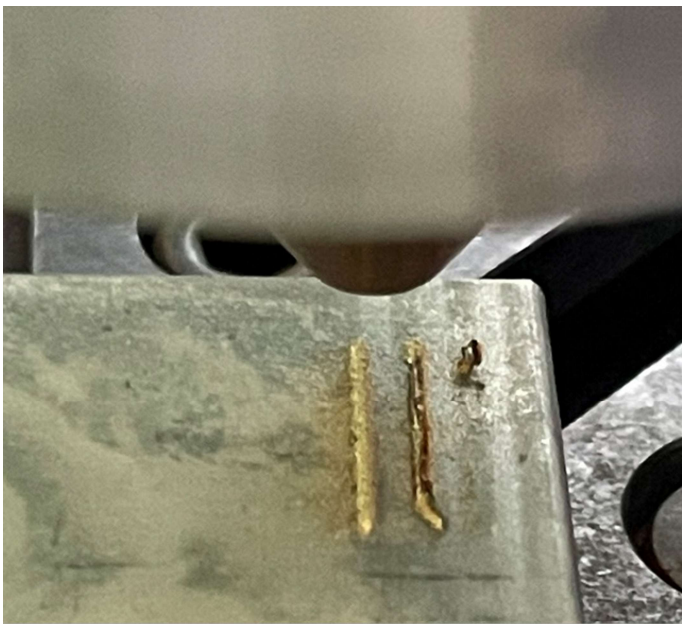


Figure 4.10: Detailed view from inside the machine chamber of 85/15CuSn single tracks deposited onto the tin coated copper substrate

Optical cross-sectional micrographs of the deposited bronze single tracks onto the tin coated copper substrate were taken to further investigate the interface between the beads and the substrate. Few examples are reported in Figure 4.11, and their respective process parameters are listed in Table 4.6.

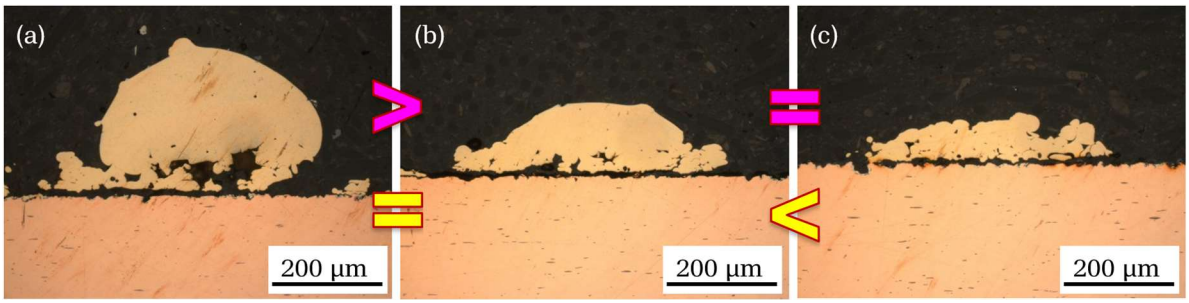


Figure 4.11: Optical cross-sectional micrographs of the deposited bronze single tracks onto the tin coated copper substrate (process parameters listed in Table 4.6). The operators between the samples state the relationships between energy density (pink) and LEPF (yellow) respective values

Table 4.6: Process parameters and calculated Energy Density/Laser Energy per unit Powder Feed (LEPF) values for the investigated samples from Figure 4.11

Label from Figure 4.11	P_{laser} (W)	v (mm/min)	Feed Rate (g/min)	Energy Density (J/mm^2)	LEPF (J/g)
(a)	440	100	1.9	330	13,895
(b)	440	300	1.9	110	13,895
(c)	440	300	1.2	110	22,000

After optical analysis of the interface, it could be noted that no real penetration of the bronze bead had occurred and all the single tracks resulted floating above the tin coated surface. However, as the tracks couldn't be easily detached by weak pulling of fingers, some points of adhesion were supposed to be present, but they were not captured by any cross-sectional micrographs taken. Moreover, the substrate surface looked completely untouched and higher magnifications show that the tin layer didn't evaporate from the surface after the interaction with the laser beam, and, eventually, good bonding with the tin-bronze powder was obtained (Figure 4.12).

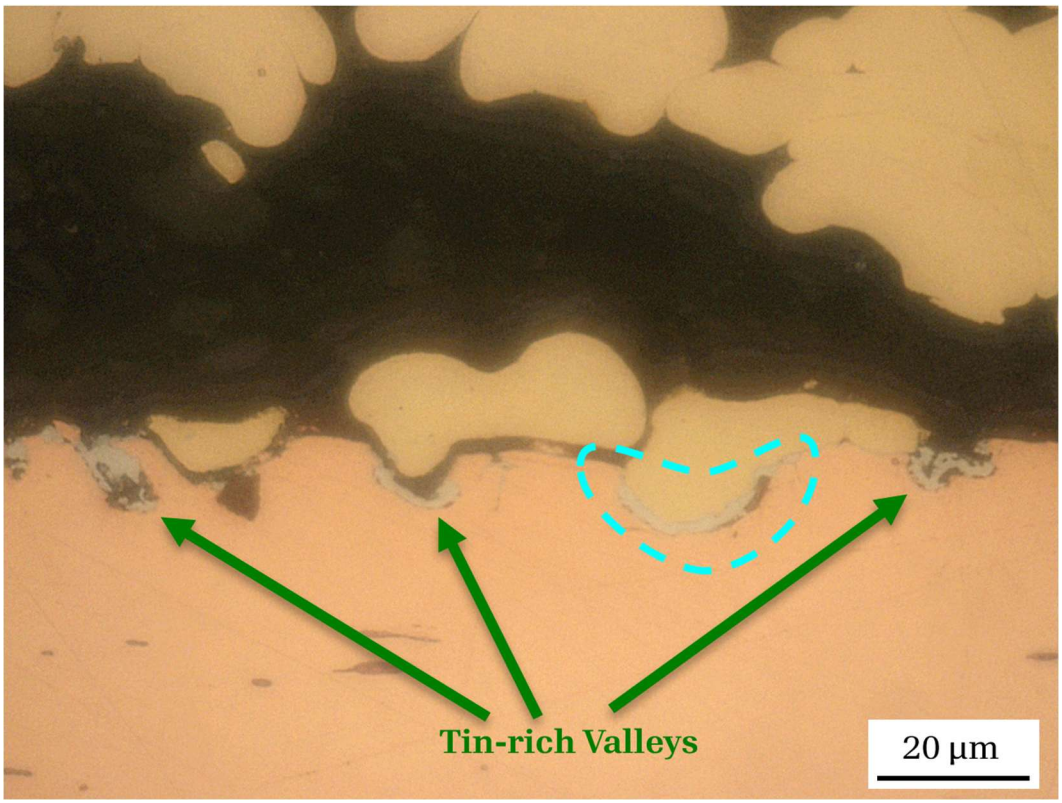


Figure 4.12: 100x magnification of an 85/15CuSn single track cross-section, with highlighting of the tin-rich surface valleys. The light-blue dotted curve highlights the metallurgical bond between the tin coating and the deposited bronze layer

High-speed observation of both laser scans at different scanning speeds and thin walls of 85/15CuSn bronze powder onto tin coated copper substrate were taken. The

purpose of the experiments was to visually observe the LB-DED process and to understand when the detachment from the substrate occurs and, possibly, its origin.

Two acquisitions were taken of the interaction between the laser and the substrate when no powder was injected. The laser power was set constant for both scans (95 % of the nominal output power, i.e. 440 W after system attenuation), and the laser scanning speed varied from 20 mm/min (single indicative frame of the scan reported in Figure 4.13a) to 100 mm/min (Figure 4.13b). Brighter areas (highlighted by yellow arrows) could be recognized where the laser was focused meaning that the substrate was heated up, but no real melting imprints were left on the substrate for both cases.

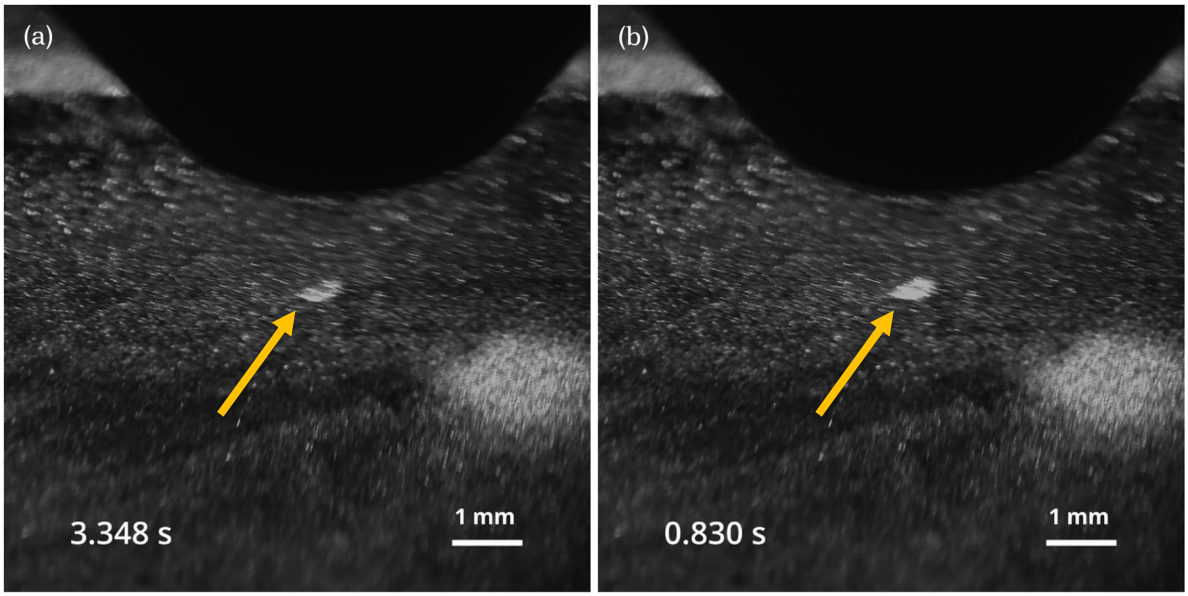


Figure 4.13: High-speed images of the laser beam interaction with the tin coated substrate at different laser scanning speed: (a) 20 mm/min, (b) 100 mm/min.

Two thin walls were printed at room temperature according to the parameters listed in Table 4.7 with two different illumination modes for the video acquisition (respectively back and front-light).

Table 4.7: Tested process parameters during the high-speed imaging of the LB-DED process of thin wall depositions of bronze onto the tin coated copper substrate; tests 1 and 2 refer to the different illumination modes

# Test	Type	P_{laser} (W)	v (mm/min)	PRS (% of 10 rpm)	WD (mm)
1, 2	3-layer Wall	440 + 300	100 + 450	8	3.5

While the first layer maintained continuous adhesion with the substrate throughout its entire deposition (Figures 4.14a-b), the detachment from the substrate at the end of the deposition of the second layer of bronze could be clearly observed with the backlight illumination mode (Figure 4.14d), as the LED light is reflected below the floating bead. This in-situ evidence confirmed that delamination initiated before the

deposition of the third layer. Moreover, the conductive heat dissipation was affected by the loss of physical contact with the substrate, and the consequent heat accumulation in the upper part of the wall exacerbated thermal distortion and bending observed in subsequent passes.

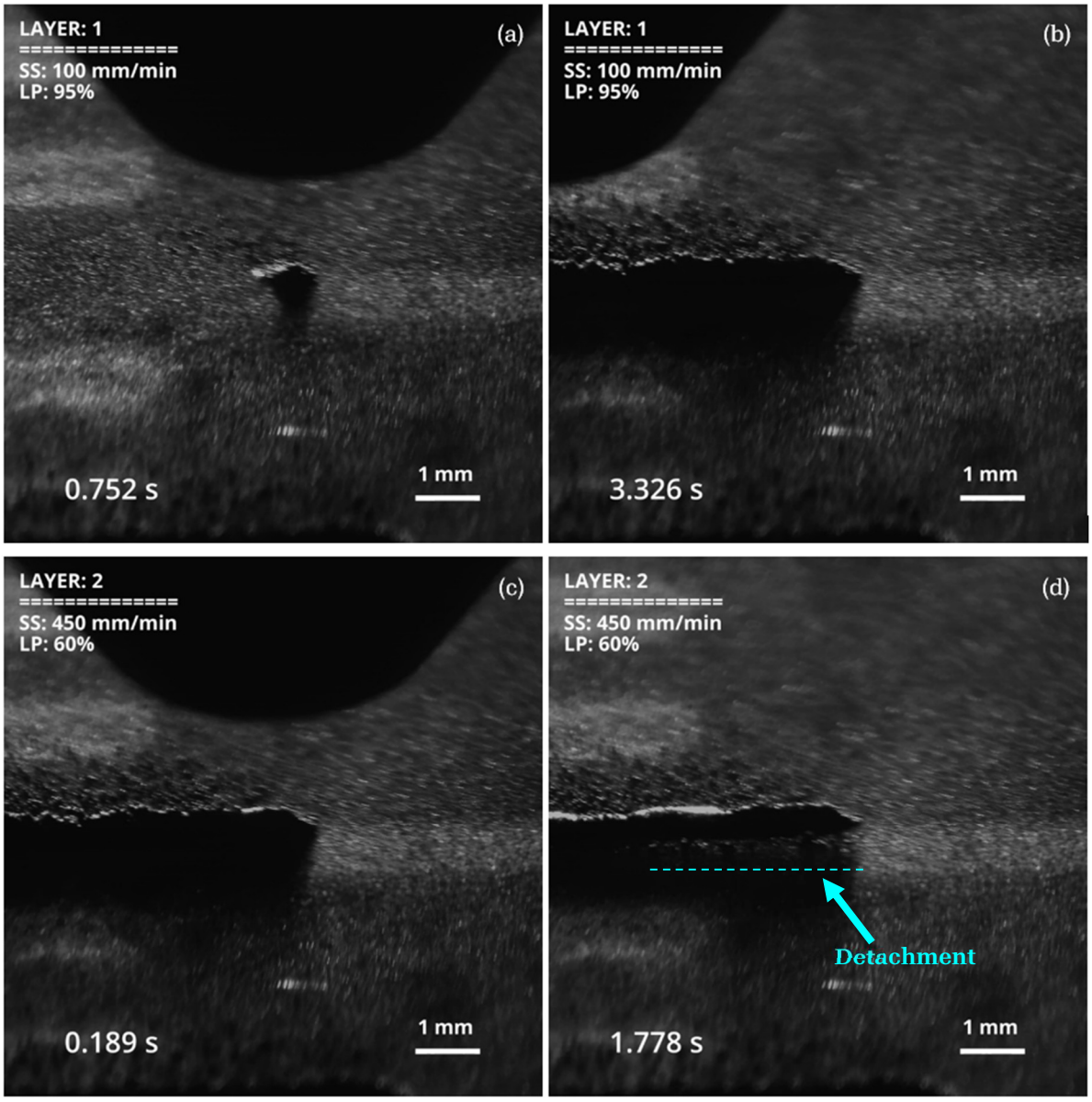


Figure 4.14: High-speed images of the 85/15CuSn thin wall deposition with backlight setup: (a) beginning of first layer, (b) end of first layer, (c) beginning of second layer, (d) end of second layer. The light blue arrow highlights the detachment area from the substrate

The front-light high-speed imaging was performed to capture the process dynamics. Two distinct frames – the first acquired during the deposition of the third layer (Figure 4.15a) and the second upon complete cooling (Figure 4.15b) – were analyzed with a 2D feature-tracking algorithm (LAP tracker) to quantify the thermal displacement of the bead. A processed magnification of the frame acquired at the end of the cooling stage is reported in Figure 4.15c. The colored circles represent the areas

tracked by the algorithm and the little tracks inside represent the calculated vectors of displacement.

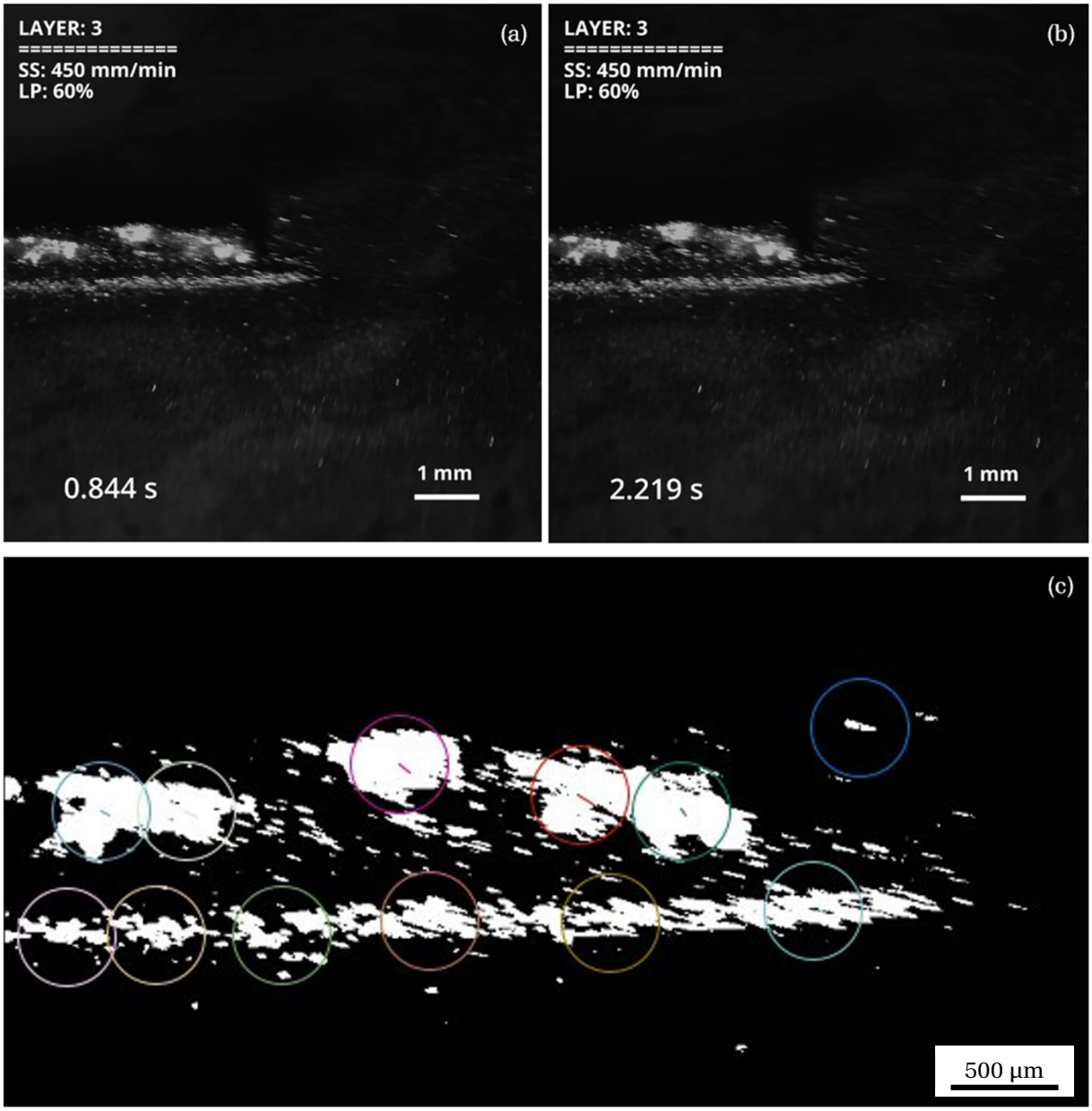


Figure 4.15: Thermal distortion evaluation using 2D feature-tracking algorithm: (a) initial and (b) post-cooling raw frames captured via high-speed visible imaging; (c) processed second frame with highlighted tracked regions (colored circles) and displacement vectors.

To quantitatively evaluate the localized deformation along the build, the net displacement values extracted by the 2D LAP tracking algorithm were plotted against the longitudinal position (X) along the track (Figure 4.16). This analysis enables a clear distinction between the stationary reference points on the lower baseline and the thermal affected regions of the deposited bead.

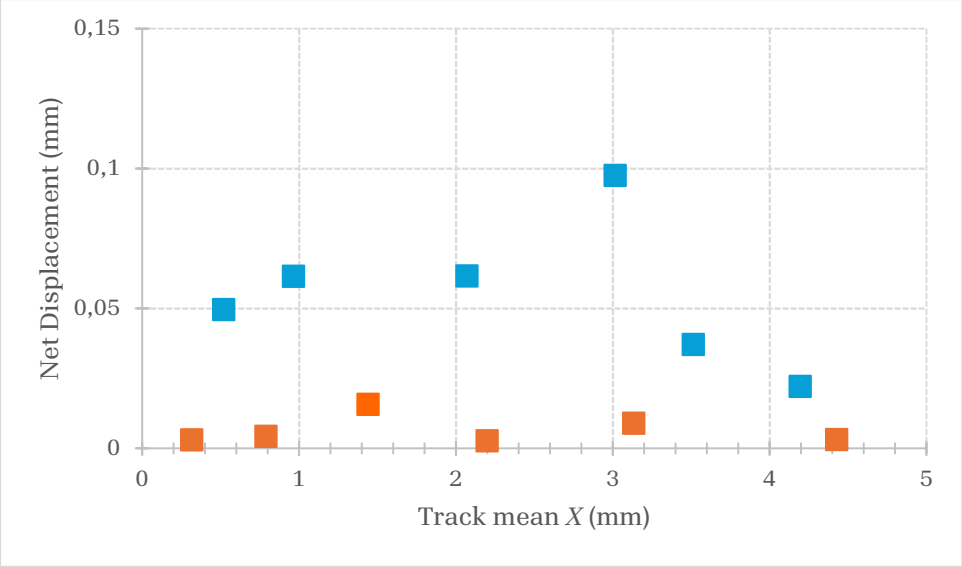


Figure 4.16: Net displacement against longitudinal position (*X*) along the track plot for the analyzed regions of interest; the orange squares represent the stationary reference points on the baseline, while the blue squares represent the points standing on the cooled layer

The blue squares of Figure 4.16 associated with the substrate baseline exhibited negligible displacement (lower than 0.01 mm), confirming camera stability during acquisition. Conversely, the tracked features within the cooled layer revealed a clear displacement gradient, reaching a maximum value of approximately 0.10 mm near *X* = 3.0 mm. With the wall height being roughly 0.5 mm at that stage, the calculated net displacement represented a relative distortion of around 20 %. The pronounced localized bending was driven by severe thermal gradients as the deposited bronze layers hampered heat dissipation. Indeed, bronze has a lower thermal conductivity of 63 W m^{-1} K^{-1} [78] with respect to pure copper (390 W m^{-1} K^{-1} [79]), leading to heat accumulation, differential thermal contraction, and noticeable upward bending of the bead upon cooling.

To better understand the origin of thermal distortion and detachment of the printed walls from the substrate a high-speed thermal camera was used to evaluate thermal trends during the LB-DED process. The thermal camera recorded the thermal field evolution during the deposition of thin 85/15CuSn bronze walls onto a preheated (150 °C) tin coated pure copper substrate in an inert atmosphere. Argon was introduced into the LB-DED chamber to reach an oxygen content lower than 500 ppm. As is shown by the sequence reported in Figure 4.17, the detachment of the bead occurred when its core was at high temperature/near melting point, but its surface had already started to rapidly cool. In these conditions, the thermal gradients were so large that the induced thermal stresses were expected to exceed both the interfacial strength with the substrate and the intrinsic material strength at high temperature. Therefore, large distortion of the bead occurred, and detachment was very likely to happen (Figure 4.17c). Although the reported scale in Figure 4.17 displays apparent temperatures rather than absolute values, the thermal maps reliably captured the localized thermal gradients – specifically the contrast between the hot core and the rapidly solidifying outer surface that drove the wall detachment.

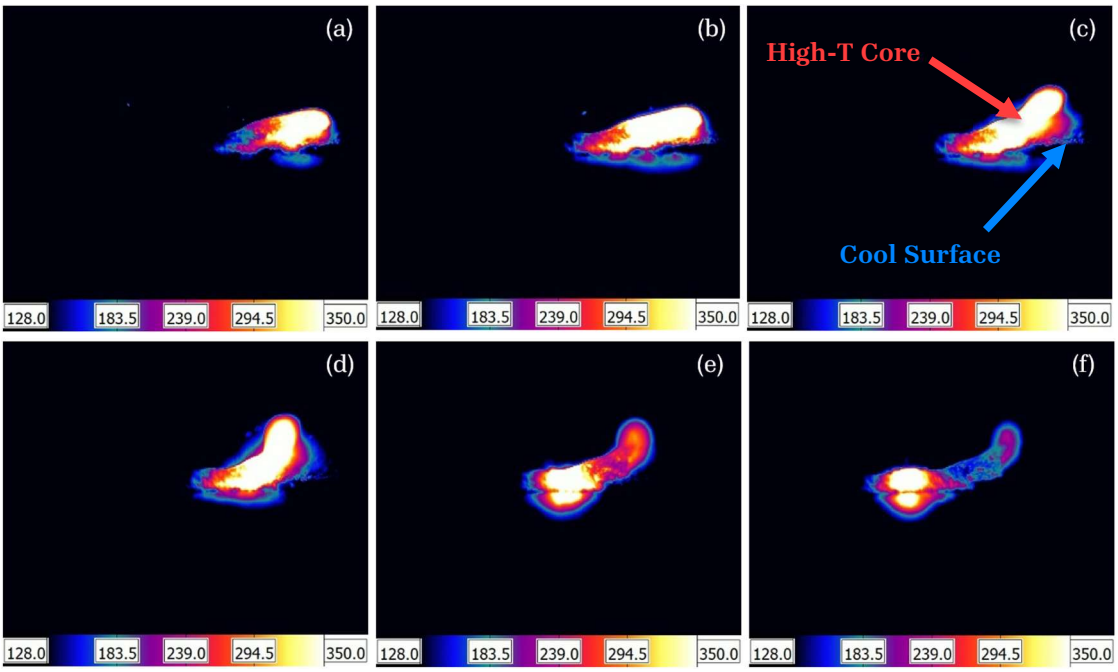


Figure 4.17: High-speed thermal camera frames acquired during the deposition of thin 85/15CuSn bronze wall onto pre-heated tin coated copper substrate; (c) onset of detachment with highlighted thermal regions

4.2.3.3 Experimental Validation of the Simulated Model

Prior to investigating the melting threshold of the tin-coated copper substrate, the numerical model developed in Chapter 4.2.3.1 was experimentally validated. Specifically, the cooling rates predicted by model were compared against in-situ data acquired with a high-speed mid-wave infrared (MWIR) thermal camera under identical process conditions. The experiment consisted of a laser scan at 440 W and 100 mm/min on the tin coated pure copper substrate under inert atmosphere (oxygen content ≤ 500 ppm). The substrate was pre-heated by a stainless-steel plate up to 150 °C. An example frame of the acquired images is reported in Figure 4.18.

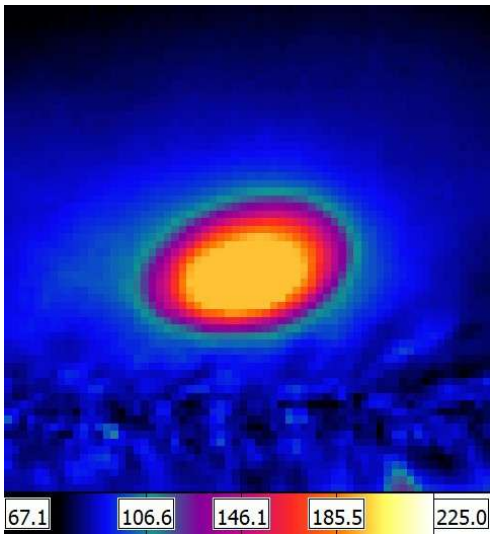


Figure 4.18: Example of a frame captured by the MWIR-camera during the laser scanning

The apparent temperature evolution over time was derived at a single point standing along the laser scan direction and the resulting plot is reported in Figure 4.19.

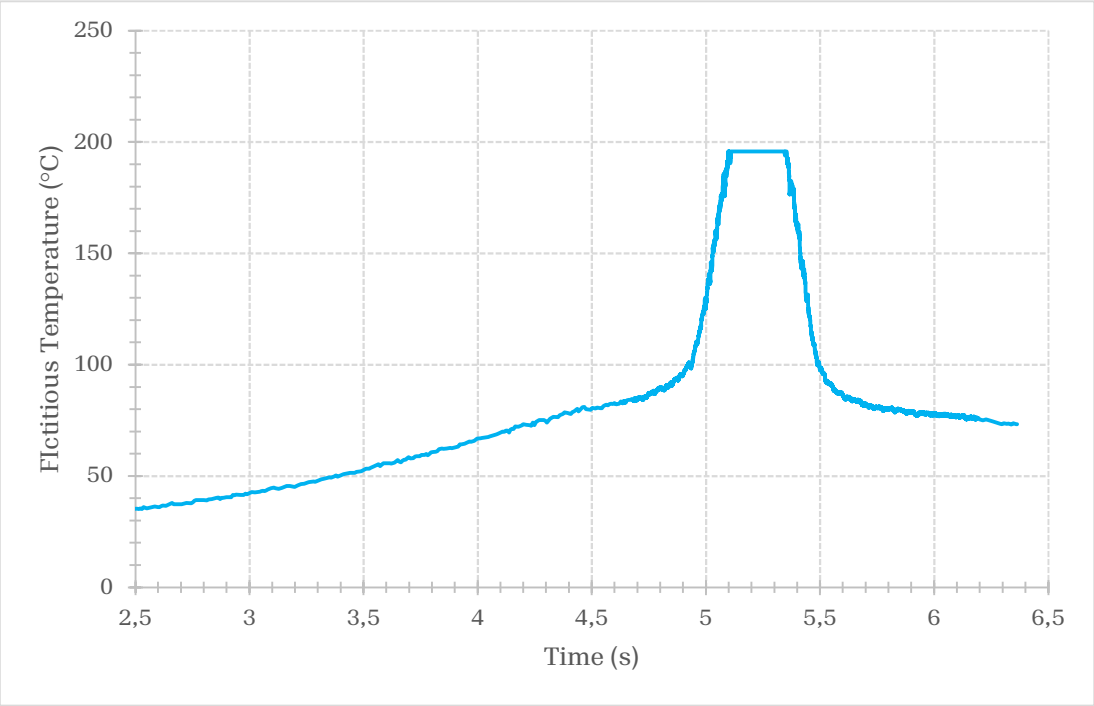


Figure 4.19: Fictitious temperature plot over time as derived from the MWIR-camera in a point standing along the laser scan; the plateau at around 196 °C is due to sensor saturation at high temperatures

The temporal profile shows a gradual preheating ramp ($t < 5.0$ s) as the laser approaches the monitored location, followed by a sharp temperature spike upon direct beam interaction that plateaus at upper sensor limit ($5.1 < t < 5.4$ s), and a fast decay reflecting the heat dissipation through the substrate ($t > 5.5$ s).

Although the recorded temperatures are apparent, the extracted cooling rates remain fully reliable as they depend on the relative rate of temperature decay rather than absolute values. To attenuate the high-frequency noise of the data acquired by the thermal camera, the experimental cooling rate function has been calculated as the slope of the linear regression performed over a 51-point centered moving window ("TC#51" curve in Figure 4.20). Specifically, at each time step, the local time derivative was derived using an ordinary least-squares fit covering a time interval of approximately 10 ms. This specific time-width ensured consistency with the time interval chosen for computing the cooling rate derived from simulation. By juxtaposing the two curves on the same graph, the cooling stage can be compared (Figure 4.20).

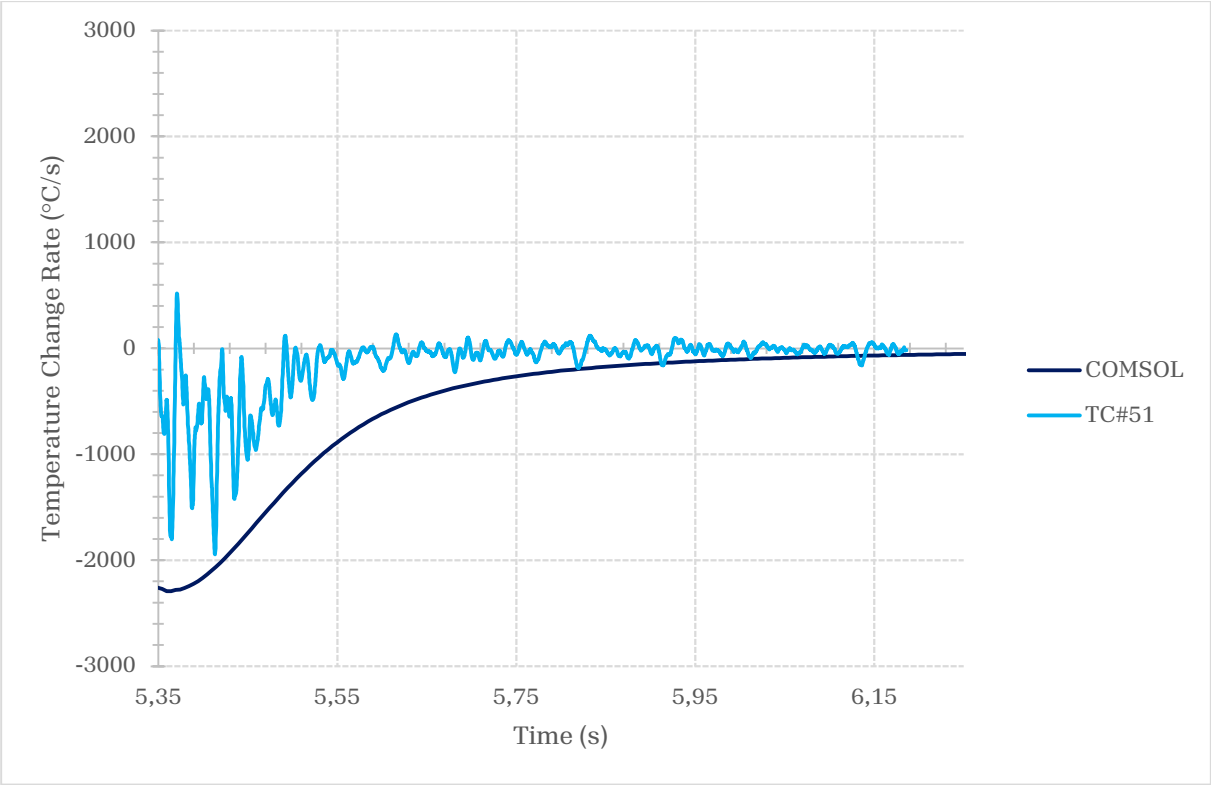


Figure 4.20: Comparison between simulated ("COMSOL", dark blue) and experimentally derived ("TC#51", light blue) cooling rates

The peak cooling rate derived from the experimental data was around -2,000 °C/s, which was close to the simulation derived one (i.e. -2,200 °C/s). Comparing the slope of the two curves, the simulation cooling process seemed to last longer without a sharper difference in cooling rates over time as is the case of the experimentally derived data. This might be because the volume of the real copper substrate was around 11 times bigger than the simulated one (50×100×8 mm^3 against the simulated 15×30×8 mm^3), resulting in a faster heat loss through conduction with the substrate.

In conclusion, the good consistency between the experimental and numerical peak cooling rates demonstrates that the model accurately reproduced the dominant heat dissipation mechanisms. Despite the geometric simplifications in the substrate volume, the numerical framework exhibited sufficient predictive accuracy to evaluate and compare the localized thermal fields and substrate melting thresholds.

4.2.3.4 Numerical Simulation of Tin-Coated Copper Substrate Melting Thresholds

After the model was validated by experimental data, an investigation about the minimum near-infrared laser output power requirements has been performed. A parametric study was carried out simulating a laser scan on a tin-coated copper substrate at increasing laser output power (600, 650, and 700 W). The geometry of the model was the same as reported in Chapter 4.2.3.1, but the laser scanning speed was lowered to 100 mm/min. The resulting energy density values for each case were: 450, 487.5, and 525 J/mm^2. The 10-second simulation included the cooling stage.

For the 600 W laser power case, the melting region was almost negligeable, and the energy density was not sufficient to effectively melt the copper. Starting from the 650 W scenario, a shallow melt pool was observed (Figure 4.21a-b). The biggest dimensions of the melt pools were recorded at the end of the laser scan, meaning that sufficient heat accumulation is needed to sustain the melt pool even at higher energy densities.

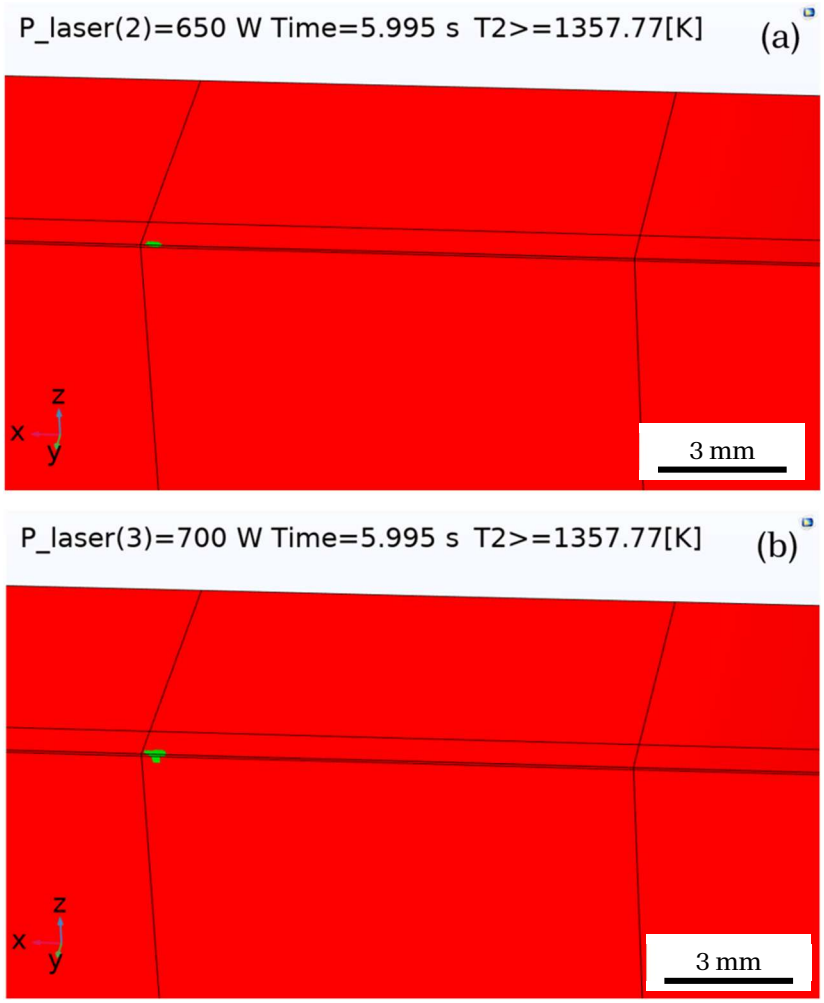


Figure 4.21: Cu-binary phase maps at the end of the laser track for the (a) 650 W and (b) 700 W scenarios. Green highlights the liquid phase volume, while red is the solid volume.

By cutting the 3D domain athwart the laser direction at t = 5.995 s, it was possible to compare the depth of the liquid regions in the 650 and 700 W laser power scenarios (measurements respectively reported in Figure 4.22a and Figure 4.22b). Regarding the 650 W case, the liquid region reached a maximum depth of 38 µm and a maximum width of around 380 µm. For the 700 W scenario, the total depth of 195 µm was reached in a region around 120 µm large with respect to the laser head axis. The cross-sectional view revealed a typical conical shape of the liquid region, and the molten area on the surface reached a width of around 400 µm.

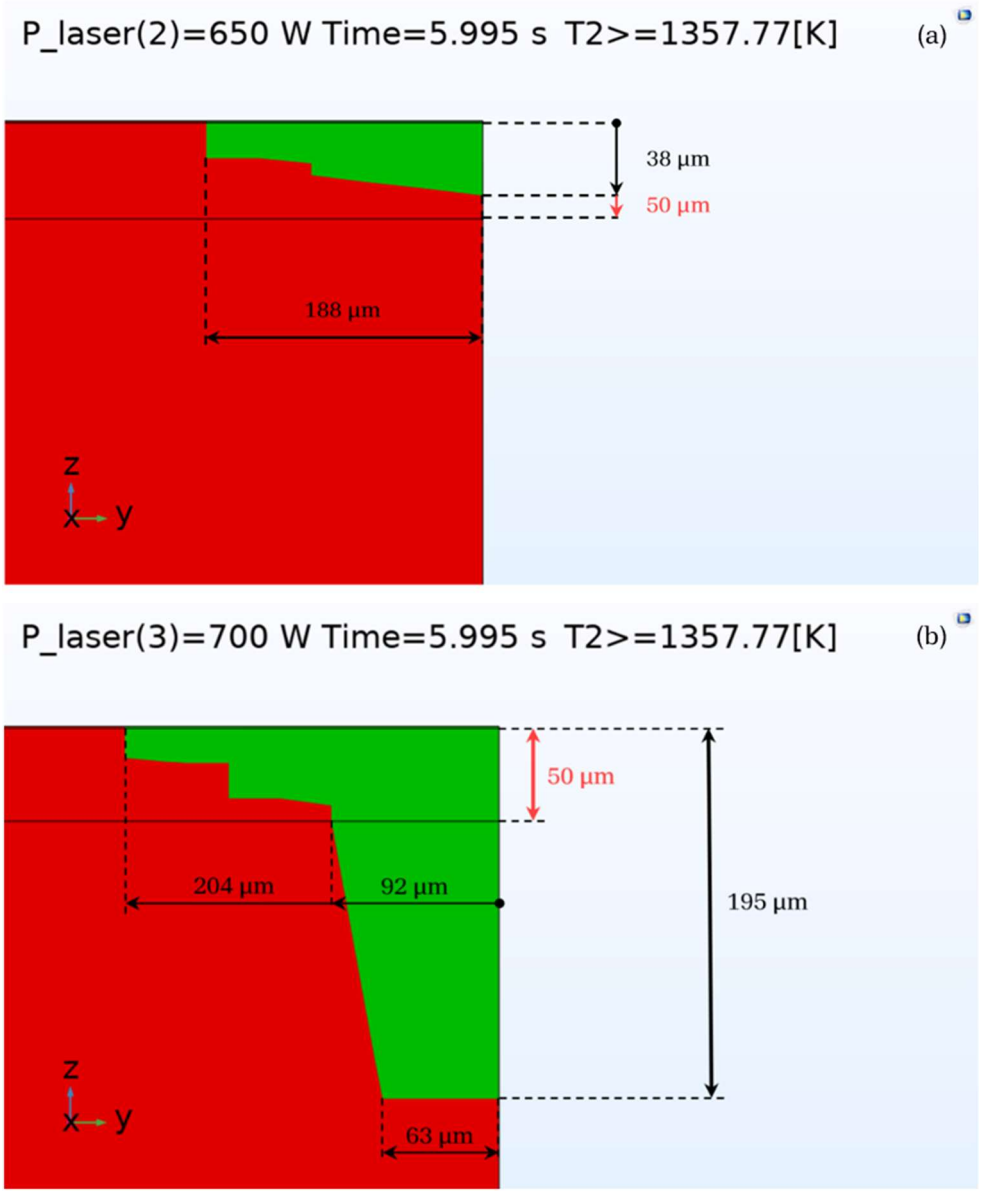


Figure 4.22: Cross-sectional view of the melt pools (green regions) as simulated by the software at the end of the laser scan for the (a) 650 W and (b) 700 W output power scenarios, with related measurements to the known depth of the sub-mesh (highlighted in red)

Considering that the maximum width of the molten region was still approximately one half of the laser spot size at focus and that the melt pool depth was reasonable only at the very last timesteps of the laser scan, it is not assured that a near-infrared laser system with an actual energy density of 525 J/mm^2 would effectively melt a tin coated copper substrate in a manner that ensures a consistent LB-DED process.

However, it is important to note how surface modification led to a marked decrease in the energy density threshold needed to initiate surface melting in the copper substrate. Around a quarter of energy density is needed to form a melt pool with similar dimensions of the sandblasted surface scenario, when a near-infrared laser with a spot size at focus of 0.8 mm is employed. This highlights once again how substrate pre-treatment is key when working with copper.

5 Conclusions

5.1 Summary of Key Findings

The present work investigated the feasibility of near-infrared Laser Based Directed Energy Deposition of copper alloy powders onto pure copper substrates as a step forward the development of advanced cooling structures for gyrotron cavities. The main conclusions are as follows:

1. **Additive Manufacturing of copper:** The high thermal conductivity of copper (390 W m^{-1} K^{-1}) and its intrinsic high optical reflectivity make it unsuitable to work with low energy density near-infrared LB-DED systems. Therefore, the presented system in its current configuration is not sufficient to work with pure copper. Conversely, because the 85/15CuSn bronze powder exhibits favorable laser-material coupling and readily melts, the process bottleneck is strictly confined to the initial interface. Consequently, this work focused on identifying surface modification strategies and the investigation of minimal laser requirements to initiate surface melting in the substrate.
2. **Untreated and Sandblasted Copper Substrates**: Numerical simulations showed that standard operating conditions – 440 W output power and 600 mm/min scanning speed, resulting in 55 J/mm^2 energy density – resulted in the absence of substrate melting (maximum recorded temperature on the irradiated substrate surface of 479 K for the sandblasted scenario). Nonetheless, sandblasting yielded an increase of ~ 26 % in peak surface temperature, owing to the enhanced optical absorptivity provided by the higher surface roughness. The attempted depositions of single tracks with energy densities in the range of 30 – 300 J/mm^2 failed due to lack of adhesion as no melt pool effectively formed on the substrate surface. Neither substrate preheating in air nor in-flight melting strategies yielded metallurgical bonding. A 2,100 J/mm^2 energy density threshold has been calculated via numerical simulation as the minimal requirement to initiate surface melting in the sandblasted substrate.
3. **Surface Modification Strategies:** The titanium sacrificial foil acted as a localized ignition point without effectively enhancing track continuity, and the carbon spray coating evaporated with laser irradiation before promoting melt pool formation. The immersion deposited tin layer significantly increased optical coupling due to the higher absorptivity at operating wavelength, but high-speed camera acquisitions showed that interfacial delamination initiates during the deposition of the second layer when thin walls are printed. 2D feature tracking quantified a localized bending distortion up to 20 % of total wall height after the third layer was deposited. High-speed thermography confirmed that this failure is driven by large thermal gradients between the molten core and rapidly cooling skin of the deposited

bead, amplified by the thermal conductivity mismatch between the bronze deposit (63 W m^{-1} K^{-1}) and the copper substrate. Furthermore, the FE model was validated against in-situ MWIR thermal measurements, and a parametric study on the minimal NIR-laser requirements stated that 525 J/mm^2 are needed to sustain a melt pool in the tin-coated copper substrate. This value is 75 % smaller than the sandblasted pure copper scenario, highlighting how substrate surface modification is key when processing copper via LB-DED.

Overall, these findings confirm the difficulties in additively manufacturing parts with copper and copper alloys with conventional near-infrared laser setups, confirming the need for high-energy density systems or alternative green/blue laser sources. However, as the research is pushing more into this direction, the challenge to print advanced cooling structures for gyrotron cavities will be eventually solved, making a great step forward the availability of high-efficiency nuclear fusion reactors.

5.2 Future Work

Future developments resulting from this research should be addressed across two distinct timeframes: short-term investigations constrained by the available configuration, and long-term perspectives relying on external facilities or alternative manufacturing paradigms.

Regarding the current in-house setup, hardware modifications – such as adapting a higher-power laser source (which would require chiller unit and delivery optics redesign) or installing alternative optical heads with smaller spot diameters – are not viable. Therefore, future on-site efforts must focus primarily on advanced surface modification. While immersion depositions showed promising initial coupling, more uniform and scalable surface engineering methods, such as Chemical Vapor Deposition (CVD), should be investigated to deposit thin, highly absorptive metallic layers directly onto the outer walls of pre-manufactured gyrotron cavities. In addition, although substrate preheating could prove essential to lower the thermal dissipation barrier, further numerical modeling is required prior to testing to assess whether preheating is genuinely effective given the high thermal conductivity of pure copper. The established numerical workflow – which showed relative error of ~ 9 % against experimental cooling rates – can serve as a key tool to model these interfacial layers and preheating regimes, minimizing experimental trial-and-error.

From an industrial and manufacturing perspective, LB-DED remains the most suitable AM technology for this application. Because existing gyrotron cavities are already qualified and demonstrate high RF performance, adding external features onto existing components via DED avoids the prolonged validation and strict surface roughness challenges associated with printing entire monolithic cavities via Laser Powder Bed Fusion (LPBF). Finally, to validate the numerical melting thresholds identified in this work, collaborative efforts on external facilities will be necessary. Such facilities could also provide access to short-wavelength laser systems (green or blue) which inherently bypass copper's high near-infrared reflectivity.

Once the fundamental bottleneck of first-layer interfacial bonding is resolved, the process monitoring methodologies developed in the present study – namely in-situ high-speed MWIR thermography and offline 2D feature tracking – can be deployed to optimize scanning strategies, mitigate thermomechanical distortion in multi-layer builds, and ultimately produce functional 3D cooling channels for hydrodynamic and thermal performance testing.

Appendix A

This appendix provides the material properties and their temperature dependence. The absorptivity of pure copper at 1,064 nm as a function of temperature was derived from Mattern et al. [25] work both for the untreated (Figure A.1a) and the roughened (Figure A.1b) case. The absorptivity of tin at 1,060 nm wavelength was given as input to the software as a function of temperature following Greenstein et al. [80] work and the resulting plot is reported in Figure A.2.

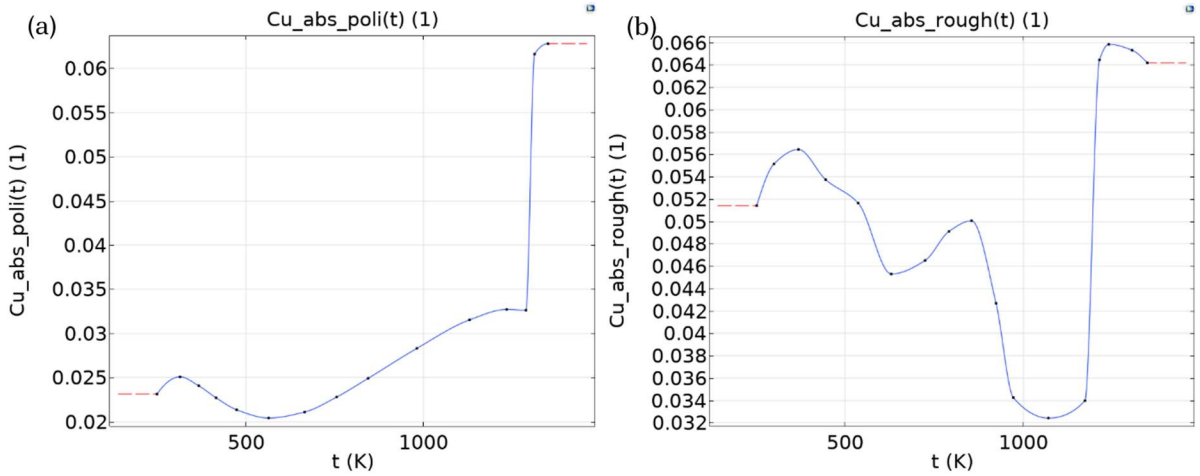


Figure A. 1: Temperature-dependent absorptivity of copper with different surface conditions: (a) untreated, (b) roughened. Adapted from Mattern et al. [25]

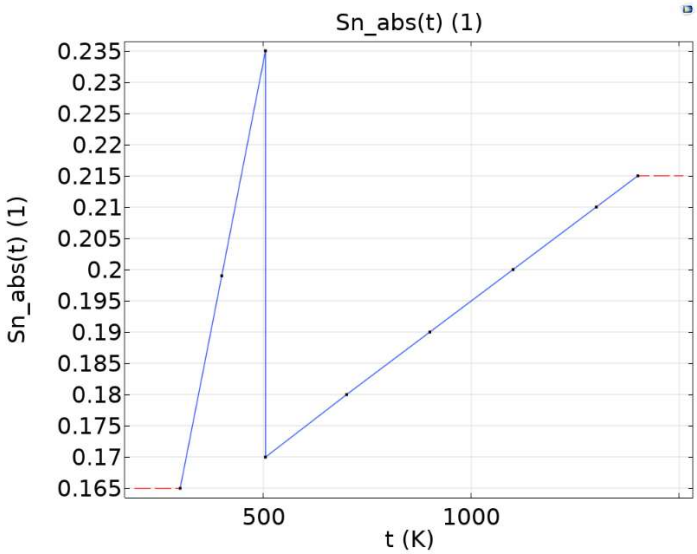


Figure A. 2: Tin absorptivity at 1,060 nm wavelength as a function of temperature as is given as input to the COMSOL model. Adapted from Greenstein et al. [80]

The density ('rho'), the specific heat capacity ('Cp') and the isotropic thermal conductivity ('k') of both electrolytic tough pitch copper and tin are reported as functions of temperature in Figure A.3. Regarding the ETP-copper, the values of the properties come from literature for temperatures below 523 K [79] and from Thermo-Calc simulation (Copper Demo Database v2.0, 100 % Cu, selected phases: 'FCC_A1', 'BCC_A2', 'HCP_A3, 'LIQUID') for the range 600 – 1,800 K. As regards the tin, the values were found in literature [81], [82], [83].

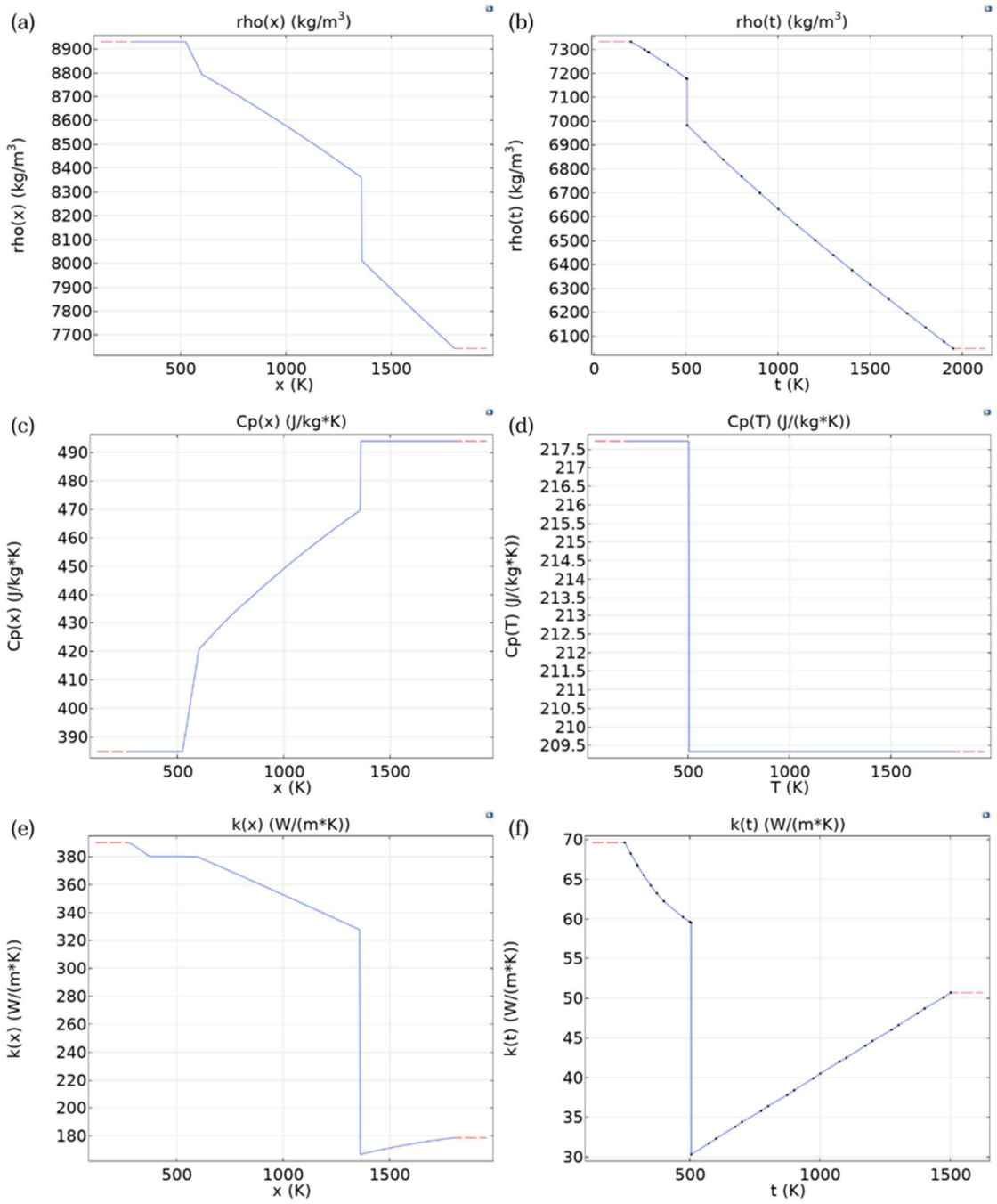


Figure A. 3: Temperature-dependent material properties (density 'rho', specific heat capacity 'Cp', and thermal conductivity 'k') for the simulated electrolytic tough pitch copper (a, c, e) and tin (b, d, f).

Appendix B

This appendix provides a direct comparison of the numerical thermal fields obtained under different substrate surface conditions, displayed on a unified temperature scale (300 – 1,000 K) at the end of the laser pass (t = 0.9992 s).

Figures B.1a-c highlight how progressive modification of the copper surface significantly affects the localized heat input: the untreated and sandblasted copper substrates reach peak surface temperatures of 380 K and 479 K, respectively, due to the high bulk reflectivity and rapid thermal dissipation of copper. The tin-coated configuration (Figure B.1c) exhibits the highest thermal absorption, resulting in a localized hotspot reaching a maximum temperature of approximately 961 K.

To verify that the higher heat absorption in the tin-coated substrate does not induce substrate melting, a binary Boolean phase evaluation was applied based on the pure copper melting point (i.e. 1,357.77 K). As illustrated by the binary phase map in Figure B.1d, the entire computational domain evaluates to false (uniformly red, corresponding to the non-fulfillment of the condition $T \geq 1{,}357.77$ K). This confirms that, while the tin coating substantially improves laser interaction, the peak substrate temperature remains largely below the melting threshold of copper.

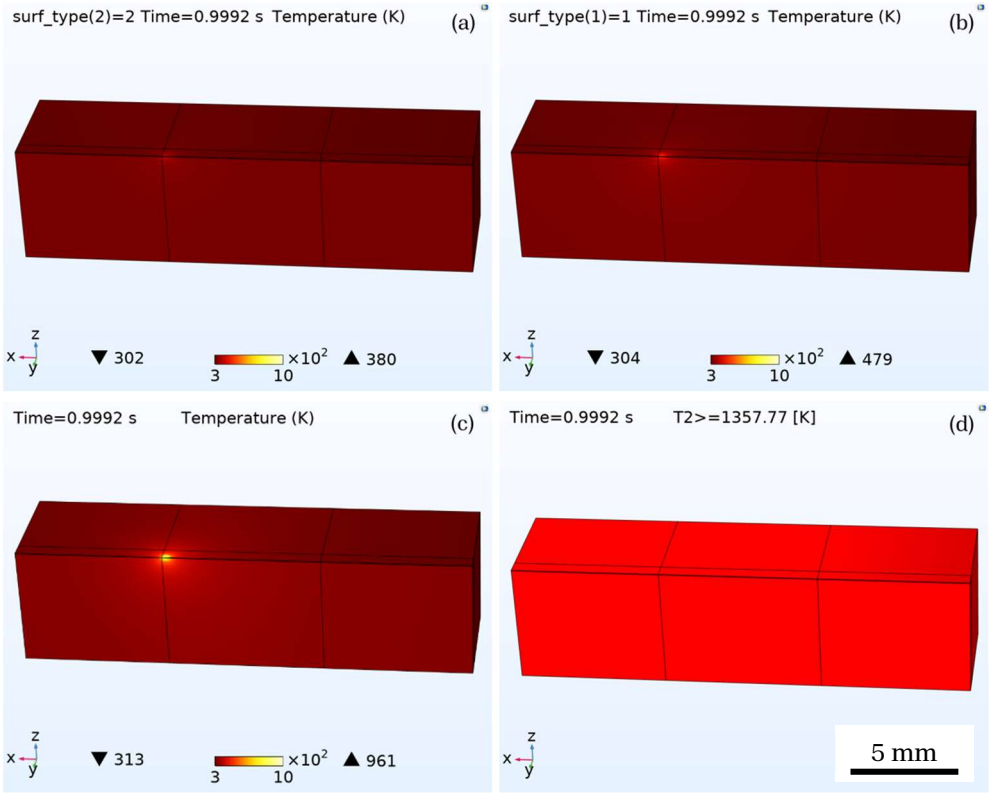


Figure B. 1: Scaled (300 – 1,000 K) numerical simulation of substrate thermal response at the end of the laser pass of: (a) untreated copper, (b) sandblasted copper, and (c) tin-coated copper substrate. (d) Binary phase map for the tin-coated case evaluating the copper melting condition, where uniform red denotes $T \leq 1{,}357.77$ K across the entire domain

Bibliography

[1] G. Nusinovich, *Introduction to the Physics of Gyrotrons*. Johns Hopkins University Press, 2004. doi: 10.1353/book.62236.

[2] A. Leggieri *et al.*, "Breaking the Megawatt Barrier in the Millimeter Wave Band for Continuous Wave Devices: Test Results of the THALES TH1507U 140 GHz 1.5 MW CW Industrial Gyrotron," in *2025 26th International Vacuum Electronics Conference (IVEC)*, Rotterdam, Netherlands: IEEE, Apr. 2025, pp. 1–2. doi: 10.1109/IVEC63678.2025.11115460.

[3] J. Jelonnek *et al.*, "Design considerations for future DEMO gyrotrons: A review on related gyrotron activities within EUROfusion," *Fusion Eng. Des.*, vol. 123, pp. 241–246, Nov. 2017, doi: 10.1016/j.fusengdes.2017.01.047.

[4] A. Bertinetti *et al.*, "Multi-physics analysis of a 1 MW gyrotron cavity cooled by mini-channels," *Fusion Eng. Des.*, vol. 123, pp. 313–316, Nov. 2017, doi: 10.1016/j.fusengdes.2017.05.016.

[5] L. Savoldi, A. Allio, and A. Leggieri, "Optimization of the flow distribution in a gyrotron cavity using evolutionary CFD simulations driven by a genetic algorithm," *Int. J. Heat Fluid Flow*, vol. 96, p. 108987, Aug. 2022, doi: 10.1016/j.ijheatfluidflow.2022.108987.

[6] M. Thumm, "Towards a 0.24-THz, 1-to-2-MW-class gyrotron for DEMO," *Terahertz Sci. Technol.*, vol. 8, no. 3, p. 85, 2015, doi: 10.11906/TST.085-100.2015.09.09.

[7] L. Savoldi, K. A. Avramidis, F. Albajar, S. Alberti, A. Leggieri, and F. Sanchez, "A Validation Roadmap of Multi-Physics Simulators of the Resonator of MW-Class CW Gyrotrons for Fusion Applications," *Energies*, vol. 14, no. 23, p. 8027, Dec. 2021, doi: 10.3390/en14238027.

[8] R. K. Singh, "Cold Analysis for Dispersion, Attenuation and RF Efficiency Characteristics of a Gyrotron Cavity," *Int. J. Electron. Commun. Eng.*, vol. 6, no. 10, pp. 1233–1238, 2012.

[9] K. Morshed-Behbahani, A. Aliyu, D. P. Bishop, and A. Nasiri, "Additive manufacturing of copper-based alloys for high-temperature aerospace applications: A review," *Mater. Today Commun.*, vol. 38, p. 108395, Mar. 2024, doi: 10.1016/j.mtcomm.2024.108395.

[10] S. Stanculovic *et al.*, "Calibration of the KIT test setup for the cooling tests of a gyrotron cavity full-size mock-up equipped with mini-channels," *Fusion Eng. Des.*, vol. 172, p. 112744, Nov. 2021, doi: 10.1016/j.fusengdes.2021.112744.

[11] A. Bertinetti *et al.*, "Analysis of an actively-cooled coaxial cavity in a 170 GHz 2 MW gyrotron using the multi-physics computational tool MUCCA," *Fusion Eng. Des.*, vol. 146, pp. 74–77, Sep. 2019, doi: 10.1016/j.fusengdes.2018.11.033.

[12] R. Difonzo, A. Cammi, C. Introini, and L. Savoldi, "Stability assessment of an optimized cooling configuration of a fusion gyrotron resonant cavity through an analytical model," *Fusion Eng. Des.*, vol. 203, p. 114455, Jun. 2024, doi: 10.1016/j.fusengdes.2024.114455.

[13] L. Savoldi, A. Allio, and A. Leggieri, "Optimization of the flow distribution in a gyrotron cavity using evolutionary CFD simulations driven by a genetic algorithm," *Int. J. Heat Fluid Flow*, vol. 96, p. 108987, Aug. 2022, doi: 10.1016/j.ijheatfluidflow.2022.108987.

[14] C. Piatti, L. Savoldi, and N. Fathi, "Numerical Assessment of Hydraulic Properties of Triply Periodic Minimal Surfaces Structures," in *ASME 2023 Verification, Validation, and Uncertainty Quantification Symposium*, Baltimore, Maryland, USA: American Society of Mechanical Engineers, May 2023, p. V001T07A001. doi: 10.1115/VVUQ2023-108794.

[15] D. Padrao, "Thermofluid Optimisation of Additive Manufacturing High Heat Flux Components for Fusion," 2024, doi: 10.13140/RG.2.2.33749.84963.

[16] I. Gibson, D. Rosen, and B. Stucker, *Additive Manufacturing Technologies: 3D Printing, Rapid Prototyping, and Direct Digital Manufacturing*. New York, NY: Springer New York, 2015. doi: 10.1007/978-1-4939-2113-3.

[17] D. Hancock, D. Homfray, M. Porton, I. Todd, and B. Wynne, "Refractory metals as structural materials for fusion high heat flux components," *J. Nucl. Mater.*, vol. 512, pp. 169–183, Dec. 2018, doi: 10.1016/j.jnucmat.2018.09.052.

[18] T. Ron, A. Shirizly, and E. Aghion, "Additive Manufacturing Technologies of High Entropy Alloys (HEA): Review and Prospects," *Materials*, vol. 16, no. 6, p. 2454, Mar. 2023, doi: 10.3390/ma16062454.

[19] L. E. T. Mathias *et al.*, "Metal powder as feedstock for laser-based additive manufacturing: From production to powder modification," *J. Mater. Res.*, vol. 39, no. 1, pp. 19–47, Jan. 2024, doi: 10.1557/s43578-023-01271-8.

[20] W. Abd-Elaziem *et al.*, "On the current research progress of metallic materials fabricated by laser powder bed fusion process: a review," *J. Mater. Res. Technol.*, vol. 20, pp. 681–707, Sep. 2022, doi: 10.1016/j.jmrt.2022.07.085.

[21] J. O. Milewski, *Additive Manufacturing of Metals*, vol. 258. in Springer Series in Materials Science, vol. 258. Cham: Springer International Publishing, 2017. doi: 10.1007/978-3-319-58205-4.

[22] D. Svetlizky *et al.*, "Directed energy deposition (DED) additive manufacturing: Physical characteristics, defects, challenges and applications," *Mater. Today*, vol. 49, pp. 271–295, Oct. 2021, doi: 10.1016/j.mattod.2021.03.020.

[23] T. F. Babuska, B. A. Krick, D. F. Susan, and A. B. Kustas, "Comparison of powder bed fusion and directed energy deposition for tailoring mechanical properties of traditionally brittle alloys," *Manuf. Lett.*, vol. 28, pp. 30–34, Apr. 2021, doi: 10.1016/j.mfglet.2021.02.003.

[24] A. Aggarwal, V. Pandiyan, C. Leinenbach, and M. Leparoux, "Investigating laser beam shadowing and powder particle dynamics in directed energy deposition through high-fidelity modelling and high-speed imaging," *Addit. Manuf.*, vol. 91, p. 104344, Jul. 2024, doi: 10.1016/j.addma.2024.104344.

[25] M. Mattern, L. M. Kukreja, and A. Ostendorf, "Temperature-Dependent Reflectance of Copper with Different Surface Conditions Measured at 1064 nm," *J. Mater. Eng. Perform.*, vol. 33, no. 6, pp. 2897–2909, Mar. 2024, doi: 10.1007/s11665-023-08961-8.

[26] S. D. Jadhav *et al.*, "Laser powder bed fusion additive manufacturing of highly conductive parts made of optically absorptive carburized CuCr1 powder,"

Mater. Des., vol. 198, p. 109369, Jan. 2021, doi: 10.1016/j.matdes.2020.109369.

[27] C. T. V. Lindström, "Defect formation and mitigation during laser powder bed fusion of copper," Lausanne, EPFL, 2021. doi: 10.5075/EPFL-THESIS-9050.

[28] S. Felicioni, J. Vincic, A. Zacco, A. Aversa, P. Fino, and F. Bondioli, "Direct Energy Deposition of Inconel 718 onto Cu Substrate for Bimetallic Structures with Excellent Comprehensive Properties," *Metals*, vol. 15, no. 12, p. 1292, Nov. 2025, doi: 10.3390/met15121292.

[29] M. S. Khandpur, A. Giubilini, L. Iuliano, and P. Minetola, "On the Use of Green and Blue Laser Sources for Powder Bed Fusion: State of the Art Review for Additive Manufacturing of Copper and Its Alloys," *Metals*, vol. 14, no. 12, p. 1464, Dec. 2024, doi: 10.3390/met14121464.

[30] R. Paddock-Lamb, P. Khanbolouki, M. A. Cullinan, and M. Tehrani, "Near-infrared laser powder bed fusion of pure copper: Post-processing and structure–property relationships," *J. Mater. Res. Technol.*, vol. 40, pp. 1665–1673, Jan. 2026, doi: 10.1016/j.jmrt.2025.12.227.

[31] A. Zardoshtian, R. Esmaeilizadeh, M. Ansari, M. K. Keshavarz, H. Jahed, and E. Toyserkani, "On the Processability and Microstructural Evolution of CuCrZr in Multilayer Laser-Directed Energy Deposition Additive Manufacturing via Statistical and Experimental Methods," *J. Manuf. Mater. Process.*, vol. 7, no. 4, p. 151, Aug. 2023, doi: 10.3390/jmmp7040151.

[32] R. S. Thanumoorthy, S. Sharma, S. Bontha, and A. S. S. Balan, "Laser powder-directed energy deposition of CuCrZr using increasing LEPF approach: process development and characterization for mechanical and thermal properties," *Prog. Addit. Manuf.*, vol. 10, no. 8, pp. 5601–5621, Aug. 2025, doi: 10.1007/s40964-024-00927-z.

[33] L. Gargalis *et al.*, "Determining processing behaviour of pure Cu in laser powder bed fusion using direct micro-calorimetry," *J. Mater. Process. Technol.*, vol. 294, p. 117130, Aug. 2021, doi: 10.1016/j.jmatprotec.2021.117130.

[34] S. Yadav, C. P. Paul, A. N. Jinoop, A. K. Rai, and K. S. Bindra, "Laser Directed Energy Deposition based Additive Manufacturing of Copper: Process Development and Material Characterizations," *J. Manuf. Process.*, vol. 58, pp. 984–997, Oct. 2020, doi: 10.1016/j.jmapro.2020.09.008.

[35] K.-E. Peiponen and T. Tsuboi, "Metal surface roughness and optical reflectance," *Opt. Laser Technol.*, vol. 22, no. 2, pp. 127–130, Apr. 1990, doi: 10.1016/0030-3992(90)90022-V.

[36] D. Bergström, J. Powell, and A. F. H. Kaplan, "The absorption of light by rough metal surfaces—A three-dimensional ray-tracing analysis," *J. Appl. Phys.*, vol. 103, no. 10, p. 103515, May 2008, doi: 10.1063/1.2930808.

[37] B. Zhang, H. Xiao, W. Wang, F. Li, Y. Wang, and H. Zhu, "Influence of laser absorptivity of CuCr0.8 substrate surface state on the characteristics of laser directed energy deposition inconel 718 single track," *J. Mater. Res. Technol.*, vol. 33, pp. 1898–1909, Nov. 2024, doi: 10.1016/j.jmrt.2024.09.178.

[38] S. D. Jadhav, J. Vleugels, J. Kruth, J. Van Humbeeck, and K. Vanmeensel, "Mechanical and electrical properties of selective laser-melted parts produced from surface-oxidized copper powder," *Mater. Des. Process. Commun.*, vol. 2, no. 2, Apr. 2020, doi: 10.1002/mdp2.94.

[39] S. D. Jadhav, P. P. Dhekne, S. Dadbakhsh, J.-P. Kruth, J. Van Humbeeck, and K. Vanmeensel, "Surface Modified Copper Alloy Powder for Reliable Laser-based Additive Manufacturing," *Addit. Manuf.*, vol. 35, p. 101418, Oct. 2020, doi: 10.1016/j.addma.2020.101418.

[40] S. D. Jadhav *et al.*, "Highly conductive and strong CuSn0.3 alloy processed via laser powder bed fusion starting from a tin-coated copper powder," *Addit. Manuf.*, vol. 36, p. 101607, Dec. 2020, doi: 10.1016/j.addma.2020.101607.

[41] R. Zheng *et al.*, "Enhanced densification of copper during laser powder bed fusion through powder surface alloying," *J. Mater. Process. Technol.*, vol. 305, p. 117575, Jul. 2022, doi: 10.1016/j.jmatprotec.2022.117575.

[42] Z. Hu *et al.*, "The enhancement of laser absorptivity and properties in laser powder bed fusion manufactured Cu-Cr-Zr alloy by employing Y2O3 coated powder as precursor," *J. Alloys Compd.*, vol. 927, p. 167111, Dec. 2022, doi: 10.1016/j.jallcom.2022.167111.

[43] O. A. Tertuliano *et al.*, "High absorptivity nanotextured powders for additive manufacturing," *Sci. Adv.*, vol. 10, no. 36, p. eadp0003, Sep. 2024, doi: 10.1126/sciadv.adp0003.

[44] S. Sharma, R. S. Thanumoorthy, S. Bontha, and A. S. S. Balan, "Copper-graphene nanocomposite fabrication through LP-DED process: Powder preparation, characterization and printability studies," *J. Manuf. Process.*, vol. 131, pp. 707–723, Dec. 2024, doi: 10.1016/j.jmapro.2024.09.069.

[45] S. Zaimovic, L. Maggio Tanasi, V. Serafini, J. Blanco Triana, and G. Perrone, "High brightness 500W blue laser source for DED processes," in *High-Power Diode Laser Technology XXIII*, E. P. Zucker, J. Campbell, and M. S. Zediker, Eds., San Francisco, United States: SPIE, Mar. 2025, p. 11. doi: 10.1117/12.3044153.

[46] H. Siva Prasad, F. Brueckner, J. Volpp, and A. F. H. Kaplan, "Laser metal deposition of copper on diverse metals using green laser sources," *Int. J. Adv. Manuf. Technol.*, vol. 107, no. 3–4, pp. 1559–1568, Mar. 2020, doi: 10.1007/s00170-020-05117-z.

[47] X. Liu, H. Wang, K. Kaufmann, and K. Vecchio, "Directed energy deposition of pure copper using blue laser," *J. Manuf. Process.*, vol. 85, pp. 314–322, Jan. 2023, doi: 10.1016/j.jmapro.2022.11.064.

[48] A. Domine, C. Verdy, C. Penaud, L. Vitu, N. Fenineche, and L. Dembinski, "Selective laser melting (SLM) of pure copper using 515-nm green laser: from single track analysis to mechanical and electrical characterization," *Int. J. Adv. Manuf. Technol.*, Sep. 2023, doi: 10.1007/s00170-023-12338-5.

[49] A. Ben Hammouda, H. Mrad, H. Marouani, A. Frikha, and T. Belem, "Process Optimization and Distortion Prediction in Directed Energy Deposition," *J. Manuf. Mater. Process.*, vol. 8, no. 3, p. 116, May 2024, doi: 10.3390/jmmp8030116.

[50] B. Aslan Çiğir and O. Yılmaz, "THERMO-MECHANICAL ANALYSIS IN DIRECTED ENERGY DEPOSITION (DED) METHOD: PREDICTION OF DISTORTION AND RESIDUAL STRESSES," *Sivas Cumhur. Üniversitesi Mühendis. Fakültesi Derg.*, vol. 3, no. 1, pp. 55–63, Jun. 2025, doi: 10.66248/cumfad.1684389.

[51] V. Nain, T. Engel, M. Carin, D. Boisselier, and L. Seguy, "Development of an Elongated Ellipsoid Heat Source Model to Reduce Computation Time for

Directed Energy Deposition Process," *Front. Mater.*, vol. 8, p. 747389, Dec. 2021, doi: 10.3389/fmats.2021.747389.

[52] L. L. Beghini, M. Stender, D. Moser, B. L. Trembacki, M. G. Veilleux, and K. R. Ford, "A coupled fluid-mechanical workflow to simulate the directed energy deposition additive manufacturing process," *Comput. Mech.*, vol. 67, no. 4, pp. 1041–1057, Apr. 2021, doi: 10.1007/s00466-020-01960-9.

[53] M. Çallı, E. İ. Albak, and F. Öztürk, "Prediction and Optimization of the Design and Process Parameters of a Hybrid DED Product Using Artificial Intelligence," *Appl. Sci.*, vol. 12, no. 10, p. 5027, May 2022, doi: 10.3390/app12105027.

[54] Oles Honchar Dnipro National University, Physical and technical faculty, Gagarina Avenue 72, Dnipro, 49010, Ukraine *et al.*, "Modeling of Thermal Processes in DED Using SolidWorks Simulation," *Adv. Therm. Process. Energy Transform.*, vol. 7, no. 2, pp. 31–34, 2024, doi: 10.54570/atpet2024/07/02/0031.

[55] Oak Ridge National Laboratory (ORNL), Oak Ridge, TN (United States) *et al.*, "Integrated Process and Materials Modeling for Development of Additive Manufacturing of Refractory Materials for Critical Applications," ORNL/TM-2023/3226, 2397457, Feb. 2024. doi: 10.2172/2397457.

[56] S. Takemura, R. Koike, Y. Kakinuma, Y. Sato, and Y. Oda, "Design of powder nozzle for high resource efficiency in directed energy deposition based on computational fluid dynamics simulation," *Int. J. Adv. Manuf. Technol.*, vol. 105, no. 10, pp. 4107–4121, Dec. 2019, doi: 10.1007/s00170-019-03552-1.

[57] A. Kiran, J. Hodek, J. Vavřík, M. Urbánek, and J. Džugan, "Numerical Simulation Development and Computational Optimization for Directed Energy Deposition Additive Manufacturing Process," *Materials*, vol. 13, no. 11, p. 2666, Jun. 2020, doi: 10.3390/ma13112666.

[58] A. Love, O. A. Valdez Pastrana, S. Behseresht, and Y. H. Park, "Advancing Metal Additive Manufacturing: A Review of Numerical Methods in DED, WAAM, and PBF," *Metrology*, vol. 5, no. 2, p. 30, May 2025, doi: 10.3390/metrology5020030.

[59] A. El Ouali, Y. Khattari, B. Lamrani, T. El Rhafiki, Y. Zeraouli, and T. Kousksou, "Apparent heat capacity method to describe the thermal performances of a latent thermal storage system during discharge period," *J. Energy Storage*, vol. 52, p. 104960, Aug. 2022, doi: 10.1016/j.est.2022.104960.

[60] G. B. Arfken, D. F. Griffing, D. C. Kelly, and J. Priest, "THERMAL PROPERTIES OF MATTER," in *University Physics*, Elsevier, 1984, pp. 412–428. doi: 10.1016/B978-0-12-059860-1.50027-8.

[61] "Tin - Specific Heat, Latent Heat of Fusion, Latent Heat of Vaporization | nuclear-power.com," Nuclear Power. Accessed: Jul. 30, 2026. [Online]. Available: https://www.nuclear-power.com/tin-specific-heat-latent-heat-vaporization-fusion/

[62] J. C. Heigel, P. Michaleris, and T. A. Palmer, "Measurement of forced surface convection in directed energy deposition additive manufacturing," *Proc. Inst. Mech. Eng. Part B J. Eng. Manuf.*, vol. 230, no. 7, pp. 1295–1308, Jul. 2016, doi: 10.1177/0954405415599928.

[63] Fluke Corporation, "Emissivity values of common materials," Emissivity values of common materials. Accessed: Jul. 31, 2026. [Online]. Available:

https://www.bergeng.com/mm5/downloads/fluke/Emissivity-Values-of-Common-Materials-Chart.pdf?srsltid=AfmBOop2JzoLGjH4C1ag-1CLdtjW6pRbYq8KQxsviHHXWCd5KxNyXKZl

[64] M. Gouge, P. Michaleris, E. Denlinger, and J. Irwin, "The Finite Element Method for the Thermo-Mechanical Modeling of Additive Manufacturing Processes," in *Thermo-Mechanical Modeling of Additive Manufacturing*, Elsevier, 2018, pp. 19–38. doi: 10.1016/B978-0-12-811820-7.00003-3.

[65] "Thermal Contact Resistance - SolidWorks Help." Accessed: Jul. 31, 2026. [Online]. Available: https://help.solidworks.com/2025/english/solidworks/cworks/c_Thermal_Contact_Resistance.htm

[66] E. Linden and P. Vitruk, "Implant-safe settings for SuperPulse 10,600 nm CO2 laser-assisted, closed flap peri-implantitis treatment," *Practice*, vol. 8, pp. 1–4, Dec. 2015.

[67] B10 Committee, *Specification for Titanium and Titanium Alloy Strip, Sheet, and Plate*. doi: 10.1520/B0265-20A.

[68] A. F. H. Kaplan, "Laser absorptivity on wavy molten metal surfaces: Categorization of different metals and wavelengths," *J. Laser Appl.*, vol. 26, no. 1, p. 012007, Feb. 2014, doi: 10.2351/1.4833936.

[69] C. J. Doona and D. M. Stanbury, "Equilibrium and Redox Kinetics of Copper(II)−Thiourea Complexes," *Inorg. Chem.*, vol. 35, no. 11, pp. 3210–3216, Jan. 1996, doi: 10.1021/ic9502077.

[70] Z. Kovac and K.-N. Tu, "Immersion tin: Its chemistry, metallurgy, and application in electronic packaging technology," *IBM J. Res. Dev.*, vol. 28, no. 6, pp. 726–734, Nov. 1984, doi: 10.1147/rd.286.0726.

[71] S. Krzewska, H. Podsiadły, and L. Pajdowski, "Studies on the reaction of copper(II) with thiourea—III," *J. Inorg. Nucl. Chem.*, vol. 42, no. 1, pp. 89–94, Jan. 1980, doi: 10.1016/0022-1902(80)80050-9.

[72] G. Lumay *et al.*, "Measuring the flowing properties of powders and grains," *Powder Technol.*, vol. 224, pp. 19–27, Jul. 2012, doi: 10.1016/j.powtec.2012.02.015.

[73] A. Singh, S. Kapil, and M. Das, "A comprehensive review of the methods and mechanisms for powder feedstock handling in directed energy deposition," *Addit. Manuf.*, vol. 35, p. 101388, Oct. 2020, doi: 10.1016/j.addma.2020.101388.

[74] D. Ershov *et al.*, "TrackMate 7: integrating state-of-the-art segmentation algorithms into tracking pipelines," *Nat. Methods*, vol. 19, no. 7, pp. 829–832, Jul. 2022, doi: 10.1038/s41592-022-01507-1.

[75] J.-Y. Tinevez *et al.*, "TrackMate: An open and extensible platform for single-particle tracking," *Methods*, vol. 115, pp. 80–90, Feb. 2017, doi: 10.1016/j.ymeth.2016.09.016.

[76] J. Dill, M. Soshi, and K. Yamazaki, "A study on the effect of directed energy deposition substrate energy on clad geometry," *Int. J. Adv. Manuf. Technol.*, vol. 109, no. 1–2, pp. 315–333, Jul. 2020, doi: 10.1007/s00170-020-05485-6.

[77] T. Reindl, N. Hempel, and P. Mayr, "Effect of substrate preheating and in situ cooling on dimensional accuracy, microstructure, and hardness of wire-arc directed energy deposition components," *Weld. World*, vol. 69, no. 12, pp. 3745–3760, Dec. 2025, doi: 10.1007/s40194-025-02104-4.

[78] "UNS C91100 (Alloy B) Gear Bronze :: MakeItFrom.com." Accessed: Aug. 18, 2026. [Online]. Available: https://www.makeitfrom.com/material-properties/UNS-C91100-Alloy-B-Gear-Bronze

[79] M. OnlineMetals, "Electrolytic Tough Pitch (ETP) Copper, UNS C11000, OSO50 Temper flat products, rod, tube, shapes." Accessed: May 21, 2026. [Online]. Available: https://www.matweb.com/search/DataSheet.aspx?MatGUID=41a3ab3af15a4ca7b8d558b974d8eb51&ckck=1

[80] M. Greenstein, "Optical absorption aspects of laser soldering for high density interconnects," *Appl. Opt.*, vol. 28, no. 21, p. 4595, Nov. 1989, doi: 10.1364/AO.28.004595.

[81] S. V. Stankus and R. A. Khairulin, "The density of alloys of tin—lead system in the solid and liquid states," *High Temp.*, vol. 44, no. 3, pp. 389–395, May 2006, doi: 10.1007/s10740-006-0048-5.

[82] C. Ho, R. W. Powell, P. E. Liley, and C. Ho, *Thermal conductivity of the elements: a comprehensive review*. in Journal of physical and chemical reference data Supplement, no. 3,1. New York, NY: American Chemical Society [u.a.], 1974.

[83] E. Edge and E. E. LLC, "Specific Heat Capacity of Metals Table Chart." Accessed: Aug. 07, 2026. [Online]. Available: https://www.engineersedge.com/materials/specific_heat_capacity_of_metals_13259.htm